2-1-2018

Fabrication and characterization of semiconductor based photo-catalysis for light-Driven water splitting

Shady Abd El-Nasser

Follow this and additional works at: https://fount.aucegypt.edu/etds

THE AMERICAN UNIVERSITY IN CAIRO

SCHOOL OF SCIENCES AND ENGINEERING

Fabrication and Characterization of Semiconductor based Photo-catalysis for Light-driven Water Splitting

BY

Shady Abd El-Nasser

A thesis submitted in partial fulfillment of the requirements for the degree of

Masters of Science in Mechanical Engineering

Under the supervision of:

Dr. Amal Esawi

Professor, Department of Mechanical Engineering

The American University in Cairo

Dr. Rita Toth

Scientist, EMPA, Swiss Federal Laboratories for Materials Science and Technology, Dubendorf, Switzerland.

June 2017

Abstract

The straightforward, low-priced and hence extensive conversion of sun light utilizing photocatalysis in a water splitting process is the main source to provide a clean and renwable hydrogen supply. Principally, photocatalysts are semiconductor materials with a suitable band gap that can absorb incident photons to produce photogeneated charges which consequently initiate the water splitting reaction to generate oxygen and hydrogen. The process itself is typically influenced by the material properties of the semiconductor (band gap, redox potentials and crystallinity) thus, altering the band structure of the semiconductor would help build up a photocatalyst that is appropriate for susbtaintial hydrogen generation. This thesis exemplifies a detailed study of high performance yet affordable photo-electrodes for solar-driven hydrogen production using Titanium (II) oxide (TiO_2).

TiO_2 is considered to be a favorable photocatalyst that can be used as a photoanode in the photoelectrochemical cell due to its unique properties. In particular it's high physical and chemical stability, high oxidizing power of the photogenerated holes, low-cost and non-toxicity. However, TiO_2 is ideal for water splitting only under ultraviolet (UV) light due to its band gap that reaches 3.2 eV which makes its photocatalytic activity only restricted to the UV range that comprises only about 3% of the whole solar spectrum.

In this study, two titania based photoanode systems were investigated in an effort to optimize the trade-off between the low external bias needed (electrical energy input) and the high photocurrent spectral response (H_2 output).

In the first part, Na-modified TiO_2 nanostructured electrodes were studied. Varying the Na content showed a noticeable impact on the optical as well as the photoelectrochemical characteristics. The morphological characterization affirmed the presence of a discontinuous layer adsorbed over the surface of the TiO_2 nanotubes where the tublar structure is kept preserved after treatment. Chemical analysis revealed no significant change in the structural properties of TiO_2 upon modification which proves that the alkali ions were just dispersed within the TiO_2 network. Optical properties illustrate the inclusion of conduction band tail states attributed to the disordered structure where the absorption edge is slightly shifted towards higher wavelength regions. The modified electrodes maintained nearly 81 % enhancement in the photoconductivity (0.9928 mA cm^{-2}) in comparison with that of bare TiO_2 (0.1821 mA cm^{-2}) under AM 1.5G illumination (100 mW cm^{-2}, 0.05 M Ba $(OH)_2$). Also, improved carriers' separation and mobility has been accomplished which was asserted by the electrochemical impedance spectroscopy that revealed less charge transfer resistance as well as space charge capacitance for the surface modified electrodes. Further, the Mott-Schottky analysis affirmed the observed V_{oc} enhancement by demonstrating a negative shift in the flat band potential for all the Na^+-modified electrodes with respect to that of the pristine TiO_2 implying less band bending requirements. Finally, DFT calculations were implemented to add further details on the electronic structure of the disordered titania confirming the empirical findings obtained upon surface modification.

In the second part of this work, hybrid PEDOT/TiO$_2$ photoelectrodes were analyzed. The development of such nanocomposites was accomplished by controlled electrochemical anodization of Ti foil, followed by a simple and fast spin coating of PEDOT. The heterojunctions maintained superior optical sensitivity where the absorption band edge reaches nearly $\lambda \cong 694$ nm with respect to that of the unsensitized (TiO$_2$ $\lambda \cong 382$ nm). This clearly indicates the ability to promote water splitting under visible irradiation. Likewise, superior photoelectrochemical performance concerning the photoconductivity, and the charge transfer kinetics were recognized mainly due to the fact that the highest occupied molecular orbit (HOMO) and lowest unoccupied molecular orbit (LUMO) of PEDOT are more negative than the conduction band (CB) and the valence band (VB) of TiO$_2$. This in return, not only narrows down the band gap but also facilitates the separation of photo-induced charges and accordingly improves the photocatalytic activity.

Thesis approval

Dr. Amal Esawi
Professor, Departement of Mechanical Engineering, The American University in Cairo
Associate Dean for Graduate Studies and Research
Director of PhD program
Thesis Advisor
Chair of Committee

Dr. Rita Toth
Scientist, Laboratory for High Performance Ceramics, EMPA, Swiss Federal Laboratories for
Materials Science and Technology, Dubendorf, Switzerland.
Thesis Co-Advisor

Dr. Joumana El-Rifai
Assistant Professor, Departement of Physics, The American University in Cairo
Internal Examiner

Dr. Mohamed H Alkordi
Associate Professor, J. Director, Centre for Materials Science University of Science and
Technology, Zewail City of Science and Technology
External Examiner

Dr. Mustafa Arafa
Professor, Department of Mechanical Engineering, the American University in Cairo
Defense Moderator

*Signatures are on file in the Graduate school

Tables of Contents

List of Figures

List of Tables

List of Charts

List of Acronyms

AM	Air Mass number
CBM	Conduction band minimum
DFT	Density functional theory
DRS	Diffuse reflectance spectra
DSSC	Dye- sensitized solar cells
EIS	Elecrtrochemical impedance spectroscopy
ESR	Electron spin resonance
FF	Fill factor
E_{fb}	Flat band potential
FTIR	Fourier Transform Infrared
$E_{p,d}$	Free enthalpy of oxidation
$E_{n,d}$	Free enthalpy of reduction
HOMO	Highest occupied molecular orbit
HER	Hydrogen-evolution reaction
IPCE	Incident-Photon-to-Current Conversion Efficiency
LSV	Linear sweep voltamettry
LUMO	Lowest unoccupied molecular orbit
MO	Methyl Orange
MS	Mott-Schottky
NEXAFS	Near edge X-ray absorption spectroscopy
NHE	Normal Hydrogen electrode

V_{oc}	Open-circuit voltage
OER	Oxyge-evolution reaction
$\eta_{c,max}$	Photoconversion efficiency
I_{ph}	Photocurrent
PEC	Photo-electrochemical
PL	Photoluminescence
PANI	Polyaniline
PPy	Polypyrrol
PEDOT	Poly-3,4-ethylene-dioxythiophene
P3HT	Poly-3-hexylthiophen
PDOS	Projective Density Of State
SEM	Scanning electron microscopy
STH	Solar-to-Hydrogen conversion efficiency
UV	Ultra Violet
VBM	Valence band maximum
V_{WE}	Working electrode potential
XRD	X-ray diffraction

Acknowledgments

Be with those who bring out the best in you not the stress in you

Chapter 1

Introduction and Scope of the Thesis

1.1 Energy Crisis

Energy is as important as raw materials, capital and labor in influencing our productivity. The consumption of energy has seen an interrelated increase with the promotion of technology and the high growth rate in worldwide human population [1]. In addition to the amount of energy in our food needed to support our body as it operates (100 W), 30 times more energy is used to make our lives more convenient [2]. Figure 1.1 shows a map of the whole world highlighting the gross per capita usage of energy for different areas as reported by Frank Hsia-San Shu [3]. The map introduces an explicit relationship between resources and energy use. Related to their prosperity, North American and the Middle East are leading in their utilization of energy. There are large areas of the world where the per capita use of energy is considerably low. Nonetheless, the trend is evolving expeditiously in some developing countries like China and India. This evolution deepens the main threat of the 21st century that is, global warming and energy crises. World population will presumably rise to 9 billion in 2050. If the average per capita use of energy is one-half of the United States then the needed global power will be almost 50 TW [3].
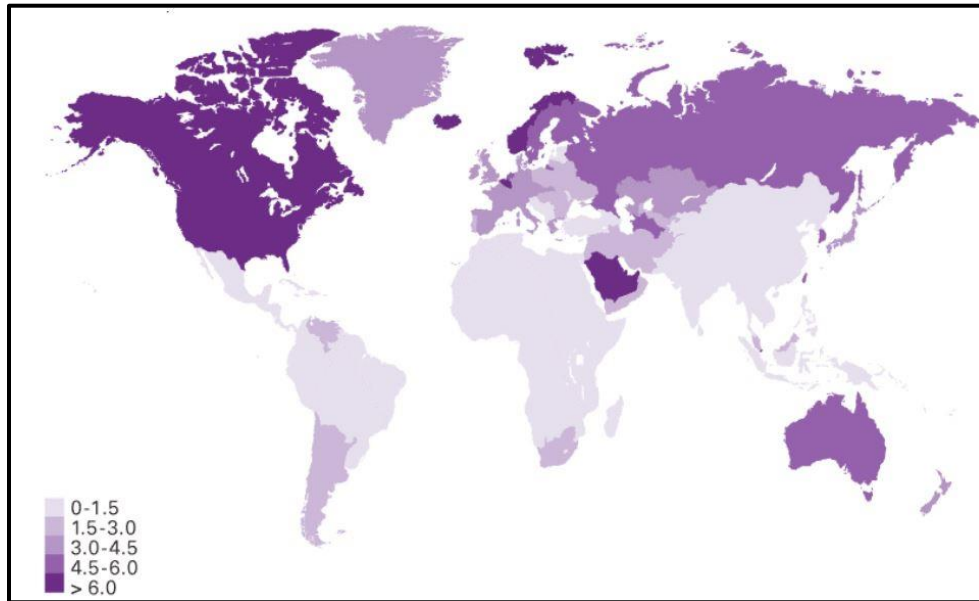
Figure 1.1: Per Capita energy consumption in 2007 (Tonnes of oil equivalents) [3]

Since the industrial revolution the energy economy of most industrialized countries was based on using fossil fuels as the elementary source of energy. Depending on such resources to satisfy our energy needs creates various problems [2]. First, an energy source can endure only until it is drained. It is predicted that the world has nearly 40 to 80 years of remaining oil supply and 60 to 160 years of natural gas supply. This is very alarming and accordingly we should begin to find alternatives. Furthermore, the increase in the world population and the higher demand on

energy for better living standards lessen the time upon which we can depend on fossil fuels [4]. If we consider oil and gas consumption as the representation for the consumption of fossil energy over a long period of time, Figure 1.2 shows that up to the start of the 20th century the decay of the resources was nearly inappreciable. At that instant the consumption rises excessively to an ultimate value that will be reached in one or two decades and will then drop again due to the continuous decay of the resources. The resources that have been piled up over millions of years will be worn out over a time of approximately one hundred years. Moreover, another crucial problem associated with the consumption of fossil fuels is the change of the atmosphere arising from the products of combustion. Up until now, these disadvantages are not vigorously perceivable but they will bring on severe obstacles for the future generations [2].
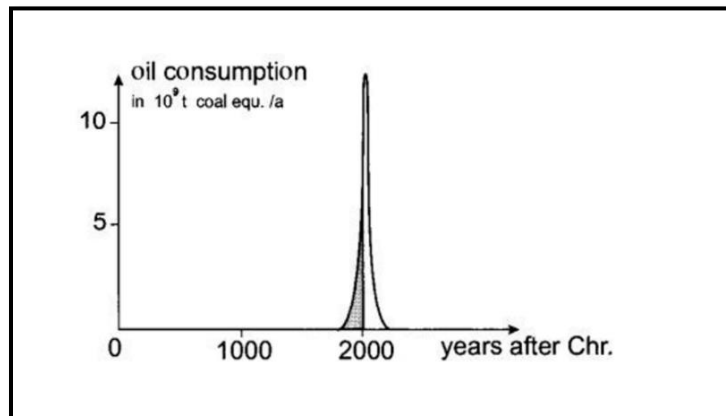
Figure 1.2: Annual consumption of Oil. The area under the curve illustrates the predicted total oil reserves [2]

Carbon dioxide (CO_2) is mainly produced from the process of burning fossil fuels due to the reaction between carbon (present in fossil fuels) and oxygen (present in the atmosphere). The increase in the percentage of CO_2 in the atmosphere will have a disastrous impact on our climate. In the time being, the atmosphere includes a portion of 0.03 % of CO_2, which amounts to 2.3 x 10^{12} t of CO_2 [2].

Continuously adding more CO_2 to the atmosphere is expected to result in considerable changes to the climate, involving a rise in the average global temperature by 1.4 – to 5.8°C (according to the intergovernmental panel on climate change) (IPCC) over the period of this century [5].

Figure 1.3 illustrates a 1000 year record monitoring the increase in CO_2 emission due to burning of fossil fuels and the consequent rise in atmospheric CO_2 concentrations as well as air temperatures.
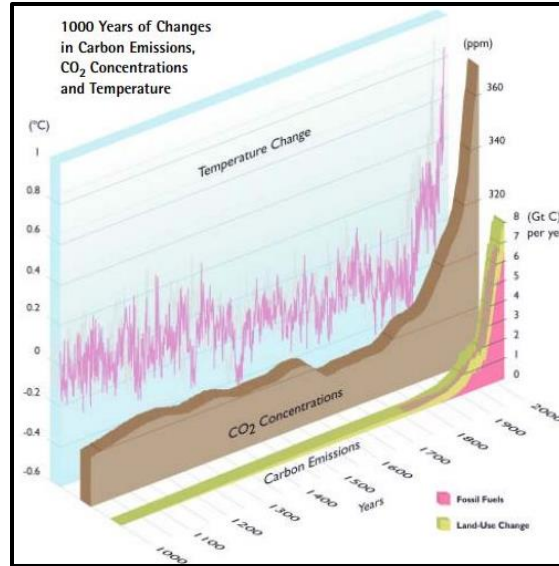
Figure 1.3: 100 years of change in carbon emissions, CO₂ concentrations and temperature [5].

Climate changes involve global consequences including melting of the glaciers and hence rising sea levels. Glaciers are considered as the primary source of fresh water for many parts of the world. They cover an area approximately equal to that of South America. Since the era of the Little Ice Age (nearly 150 years ago) they have been globally depleted, however, lately they have started melting at unprecedented rates [6].

The anticipated climate change within this century will further promote the rate by which glaciers melt since the average global temperatures are estimated to increase at the end of this century as mentioned above. Reports showed that $4°C$ increase in temperature will probably drop all the glaciers globally. The existence of these glaciers are of crucial importance since they affect both daily and seasonal norms of rivers' flow and can either raise or reduce the entire annual flow via the continuous alteration in the reservoirs (i.e. the regions encompassed by the glaciers)**.** Accordingly, their loss will yield floods, rising sea levels, water scarcity for plenty of people, as well as attacking and ruining coastal communities and habitats which in turn will negatively influence human populations as well as the ecosystem [6].

1.2 Solar Energy Conversion and Storage

For all these reasons above, the present time appears to be the reasonable time for the scientific community and energy producers to focus on developing cleaner energy systems that are not contributing to global warming. In this regard, solar energy provides a promising solution in terms of abundance and sustainability that could provide earth with 60 TW of energy which was estimated to be double the amount we would need by the year 2050 [7]. Solar energy is the only renewable source that has enough earthbound energy potential to provide a carbon-free supply of energy. From the 1.2×10^5 TW of solar energy that hits the earth's surface, a feasible global solar power potential value is approximately 600 TW that ranges from provident assessment of 50 TW to idealized assessment of 1500 TW, depending on the amount of land utilized to power generation. An acceptable fraction of inland power generation is apparently 600

TW, in this way, for a 10% qualified solar farm, at worst 60 TW of power could be delivered from inland solar energy resources. For distinction, photosynthesis delivers about 90 TW worldwide to make the ecosystem run, accordingly the amount of power generated from the sun is tremendous by any measure [8]. However, there are many challenges that may affect the utilization of solar energy for practical purposes. The temporary behavior of sunlight requires means of conversion and storage of solar energy in order to provide constant supply of energy and hence enable effective implementation in several applications. To this end, Hydrogen is regarded as a very promising energy carrier to store solar energy because:

1. It is a renewable fuel.
2. Its raw material for production is water.
3. Its energy amount per unit mass is three times that of gasoline.
4. It does not yield any greenhouse gases upon combustion in air, i.e. environmentally friendly.
5. It can be conveyed to long distances via pipelines or tankers [9]

The approach of the hydrogen economy commenced in the early 1970s. The first World Hydrogen Conference in 1976 recognized hydrogen as a renewable energy carrier for the future. The Australian chemist John Bockris first formulated the term "hydrogen economy" in 1970 [10].

There are various means to generate hydrogen. Presently, about 80-85% of the global hydrogen production is obtained via steam methane reforming of natural gas [11]. This process has emissions of CO_2 of about 7 kg CO_2/kg H_2, which is responsible for nearly 3% of the worldwide industrial zone CO_2 emissions [12].

A renewable, carbon free approach of hydrogen production is desirable to protect the environment and conserve the energy resources. In this regard, photoelectrochemical water splitting is considered to be an adequate technique to obtain hydrogen fuel because it does not lead to the emission of any hazardous gases within the entire production process and will also be useful for large-scale application in solar hydrogen generation due to its simplicity [13]

1.3 Hydrogen Generation by Water Electrolysis

Electrolysis of water to produce hydrogen and oxygen has a history of almost 200 years yet, it does not provide more than 4% of the global hydrogen production. With respect to other conventional methods (such as steam methane reforming), water electrolysis can provide very pure hydrogen (>99.9%) which is useful for some manufacturing processes such as the fabrication of electronic components [14]. The major concern in hydrogen generation by water electrolysis is that the electricity utilized to promote the reaction is mainly produced by the combustion of fossil fuels. The process could be more sustainable provided that the electricity utilized is derived from a renewable source (such as wind or solar) as described in the following reaction where oxygen, an extremely valuable gas, is the only by product.

$$H_2O + electrical\ energy \rightarrow H_2(g) + \frac{1}{2}O_2(g) \quad (1.1)$$
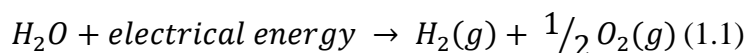
Photoelectrolysis demonstrates the electrolysis of water by direct utilization of light; particularly, the conversion of photon energy into electrical current and then the change of a chemical matter (H_2O, H_2S) into advantageous chemical energy (such as H_2) by means of that current. Accordingly, solar energy together with electrolysis, seem to be the most favorable approach for hydrogen production. [1]
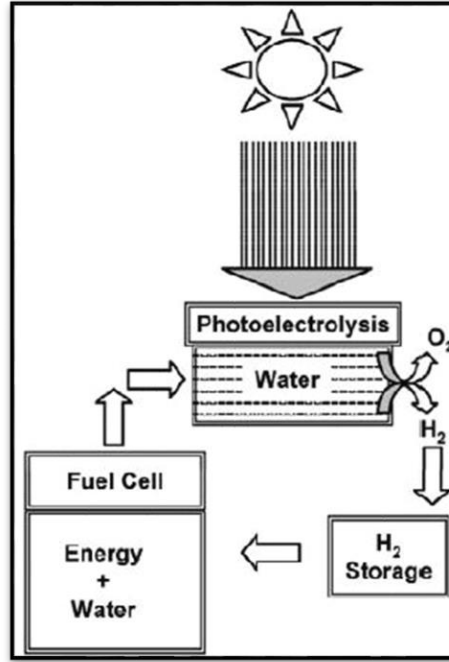
Figure 1.4: Hydrogen generation via water photoelectrolysis [1]

Similarly, plants carry out solar-chemical conversion by means of the photosynthesis reaction to maintain their food. Photosynthesis, see reaction 1.2, is a crucial way of converting solar energy into chemical energy in the form of starch or sugar. Thus, solar water-splitting for hydrogen generation can be called artificial photosynthesis [1].

$$6CO_2 + 12\ H_2O + solar\ light\ \rightarrow C_6H_{12}O_6 + 6O_2 + 6H_2O \qquad (1.2)$$
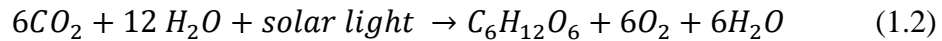
The concept of establishing an artificial device to convert sun light into a valuable form of energy by imitating the natural photosynthesis process is the principal motivation for the artificial photosynthesis research. We typically intend to break down the water molecule into hydrogen and oxygen utilizing robust and durable materials that are able to achieve adequate electron transfer. For this reason, artificial photosynthesis approaches involving photoelectrochemical (PEC) solar energy conversion have been extensively researched within the last 40 years [15].

The basis of photoelectrochemistry using semiconductors was first recognized by Gerischer in the 1960s [16]. Only semiconductor materials are appropriate for storing the energy obtained from the electromagnetic radiations and promote the stored energy to be converted to other forms. Metals are not applicable to convert photon energy due to their excited electronic states that have very short lifetimes and most of the energy will be rapidly dissipated as heat

[17]. Several reports on photoelectrochemical (PEC) water splitting describe the ordinary two-electrode configuration depicted in Figure 1.5. In this recognized setup, a light sensitive semiconductor is submerged in an electrolytic solution, with an external circuit coupled to a metallic counter electrode. Upon excitation, photoinduced electron-hole pairs in the semiconductor react electrochemically with ionic species in the electrolyte at the semiconductor/electrolyte interface. Photogenerated holes proceed the oxygen-evolution reaction (OER) at the anode, whereas photogenerated electrons proceed the hydrogen-evolution reaction (HER) at the cathode [18]. Honda and Fujishima in 1972 first described the idea of photoelectrochemical cells utilizing titanium dioxide (TiO_2) as the photoanode and platinum as the counter electrode submerged in aqueous electrolyte [19]. The low efficiency expressed by Honda and Fujishima, revealed new path ways for further research to enhance the performance of nanostructured semiconductors for hydrogen generation via light-driven water splitting. This thesis is one of these attempts.
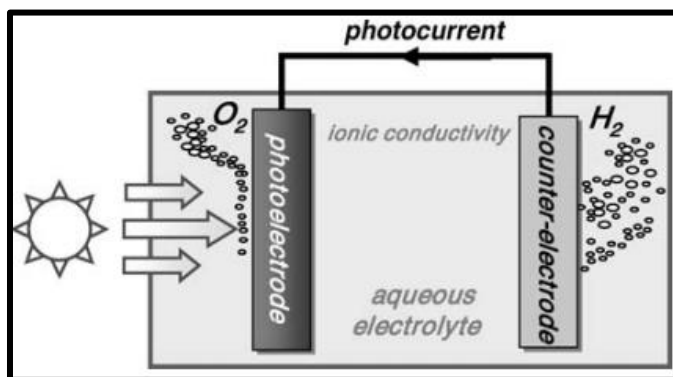
Figure 1.5: Two electrode configuration for PEC water splitting [17].

1.4 Scope of the Thesis

As it was elucidated in Chapter 1, the possibility to design and fabricate high performance yet affordable materials that can be can used to convert sun light into H_2 is one of the favorable solutions to solve the energy crisis. In this thesis, the preparation as well as the optical and photoelectrochemical properties of two systems have been investigated with the aim to reach a new-concept photoelectrochemical system for hydrogen generation. Namely: Na-modified TiO_2 photoelectrodes and PEDOT-TiO_2 heterojunctions.

Chapter 2 explains the theoretical background used throughout the thesis and the science behind the water splitting reaction as well as fundamental aspects of semiconductors to help the reader get into the discussion of the results.

Chapter 3 reviews the relevant literature on alkali metals modified and polymer sensitized TiO_2 hybrid photoelectrodes.

Chapter 4 demonstrates the details of the experimental procedures employed for fabrication and characterization of the developed samples.

Chapter 5 illustrates the results and discussion section of the Na-modified TiO_2 system based on the study of morphological, structural, optical and photoelectrochemical properties.

Chapter 6 reveals the realization and characterization of the hybrid PEDOT-TiO_2 structures as a novel system for PEC hydrogen production.

Chapter 7 summarizes and discusses the outcomes of the research and proposes some extension ideas for future work.

References

1. C. Grimes, S. Ranjan and O. Varghese, *Light, Water, Hydrogen*, 1st ed. Boston, MA: Springer Science+Business Media, LLC, 2008.

2. P. Würfel, *Physics of solar cells: from principal to new concepts*. Wienheim: Wiley-VCH Verlag, 2008.

3. F. H. Shu, "Global Change and the Energy Crisis," University of California, San Diego," vol. 2007, pp. 1–41.", 2007.

4. G. Zini and P. Tartarini, *Solar hydrogen energy systems*, 1st ed. Milan: Springer-Verlag Italia, 2012.

5. S. Hassol, *Impacts of a warming Arctic: Arctic climate impact assessment*, 1st ed Cambridge University Press, 2004.

6. S. Combes *et al.*, "Going, Going, Gone! Climate Change and Global Glacier Decline," Berlin, Germany, Brochure, 2003.

7. H. Prakasam, "Towards Highly Efficient Water Photoelectrolysis", Ph.D. dissertation, Dept. Elect. Eng., The Pennsylvania State University., Pennsylvania, USA, 2008.

8. N. Lewis, "Chemical Challenges in Renewable Energy", Pasadena, CA 91125, Tech. Rep, 2006.

9. I. Jain, "Hydrogen the fuel for 21st century," *International Journal of Hydrogen Energy*, vol. 34, no. 17, pp. 7368–7378, 2009.

10. W. Lattin and V. Utgikar, "Transition to hydrogen economy in the United States: A 2006 status report," *International Journal of Hydrogen Energy*, vol. 32, no. 15, pp. 3230–3237, 2007.

11. A. Simpson and A. Lutz, "Exergy analysis of hydrogen production via steam methane reforming," *International Journal of Hydrogen Energy*, vol. 32, no. 18, pp. 4811–4820, 2007.

12. R. Soltani, M. Rosen, and I. Dincer, "Assessment of CO_2 capture options from various points in steam methane reforming for hydrogen production," *International Journal of Hydrogen Energy*, vol. 39, no. 35, pp. 20266–20275, 2014.

13. A. Kudo, "Photocatalysis and solar hydrogen production," *Pure and Applied Chemistry*, vol. 79, no. 11, pp. 1917–1927, 2007.

14. D. M. F. Santos, C. A. C. Sequeira, and J. L. Figueiredo, "Hydrogen production by alkaline water electrolysis," *Química Nova*, vol. 36, no. 8, pp. 1176–1193, 2013.

15. K. Sivula, F. Le Formal, and M. Grätzel, "Solar Water Splitting: Progress Using Hematite (α-Fe$_2$O$_3$) Photoelectrodes," *ChemSusChem*, vol. 4, no. 4, pp. 432–449, 2011.

16. J. Schneider, D. Bahnemann, J. Ye, G. L. Puma, and D. D. Dionysiou, *Photocatalysis: fundamentals and perspectives*. Cambridge, UK: Royal Society of Chemistry, 2016.

17. L. Li, *Functional photo-electrochemical devices for solar cells and solar fuels based on molecular components*, 1st ed. Stockholm: Chemical Science and Engineering, KTH Royal Institute of Technology, 2012.

18. L. Vayssieres, *On Solar Hydrogen & Nanotechnology*, 1st ed. Singapore 129809: John Wiley & Sons (Asia) Pte Ltd, 2 Clementi Loop, # 02 01, 2009.

19. A. Fujishima and K. Honda, "Electrochemical Photolysis of Water at a Semiconductor Electrode", *Nature*, vol. 238, no. 5358, pp. 37-38, 1972.

Chapter 2

Background

There are several concepts that uphold the improvement of photocatalytic materials for solar hydrogen production. This chapter presents some essential fundamental background information used in the interpretation of the data obtained in this thesis, involving the fundamentals of solar radiation, the interrelationship between semiconductors materials and the electrolyte when utilized as photoelectrodes in a photoelectrochemical cell, the impact of nanostructures on the transport of charges and finally distinctive concentration on the selection of titanium dioxide as an exemplary of a photoelectrode will be depicted.

2.1 Solar Radiation

Sun is the optimum source of energy for almost all forms of life on earth. Each second the sun transfers 637 million tonnes of hydrogen to generate 632 million tonnes of helium by nuclear fusion reaction [1]. The difference of almost 5 million tonnes is converted to energy according to Einstein's well-known relation, $E=mc^2$. This energy increases the surface temperature by about 6000 K, consequently, it results in an increase in the spectral distribution of the solar radiation. Figure 2.1 illustrates that the solar spectrum is bell-shaped and around 96.3% of the full irradiance is restricted to the range of $0.25\mu m < \lambda < 3\mu m$. The fine holes or gaps in the spectrum are related to the absorption of particular wavelength bands by gases like H_2O, O_3, O_2 and CO_2 in the atmosphere. Planck's rule for a totally absorbing body (black body) illustrates the relation between wavelength, λ, of the electromagnetic radiations and their energy, E [2].

$$E = h\upsilon = {hc}/{\lambda} \qquad (2.1)$$

Where h is Planck's constant, υ is the frequency and c is the speed of light.
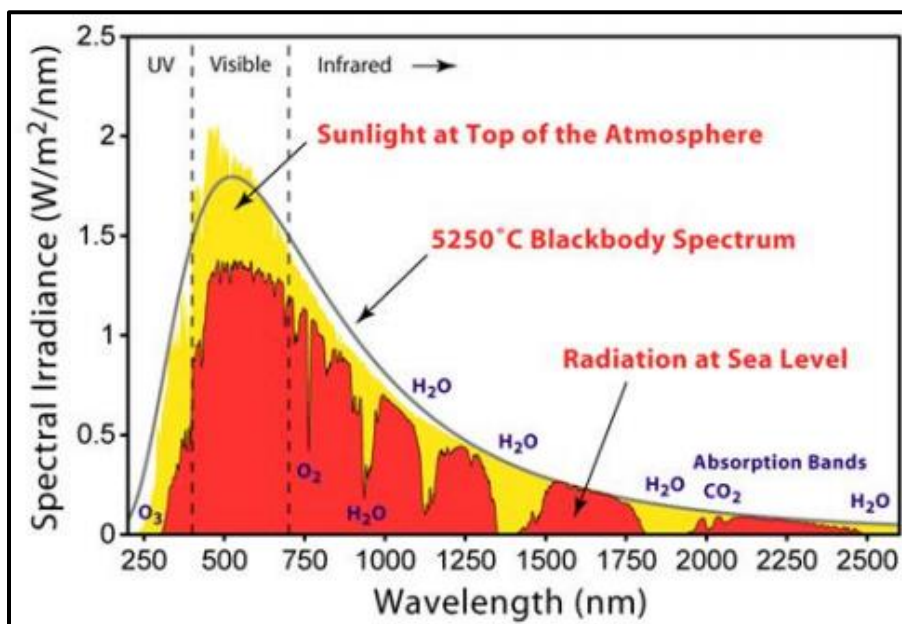
Figure 2.1: Solar spectrum at the upper atmosphere and at the surface [3]

The amount of the light energy picked up by the earth's surface changes based on the climate conditions, the time of the year, the position of the sun as well as the mass of the air by which it travels. Any light losses depend on the distance of the atmosphere it covers as it is being absorbed or dispersed by air particles. Accordingly, to accurately account for the effect of thickness of the atmosphere through which light travels, the Air Mass (AM) index expresses the general climate conditions in the United States that conform to the case when the sun is at zenith angle of 48.19^o, AM = [1/cos 48.19=1.5]. In this regard, the electromagnetic radiation passes through the atmosphere 1.5 times the extent it passes when the sun is at 0° zenith angle (AM 1.0). The typical AM 1.5 range is standardized to provide 1000 W/m^2. This is conventionally considered as 1 sun [4-6].

2.2 Photoelectrochemical Water Splitting

A cell that is able to transform photon energy into a favorable energy output by means of solar-driven electrochemical process is ordinarily called a photoelectrochemical (PEC) cell. Upon the absorption of photon energy by the photoelectrode, current and voltage are concurrently produced in a PEC. The result is either electrical or chemical energy [5].

Figure 2.2 displays a simplified schematic illustration of the photoelectrochemical (PEC) water splitting cell. The basic constituents of the PEC cell is the n-type semiconductor in the role of photoandoe as well as a counter electrode in the role of cathode. In a customary PEC cell, semiconductors employ the solar energy to advance chemical reactions on their surfaces'. Upon photoexcitation of the n-type semiconductor, electrons are agitated from the valence band to the conduction band creating an electron-hole pair. The photogenerated holes flow towards the surface of the semiconductor to react with the oxygen ions in water, producing oxygen gas at the photoanode. The hydrogen ions induced from the water oxidation will flow in the direction of the cathode, concurrently the photogenrated electrons are driven to the cathode through the back contact [7, 8]. In like manner, p-type semiconductor can be utilized in a PEC cell acting as a photocathode with a counter anode. The latter example is not commonly used because p-type semiconductors have generally shown less stability in aqueous electrolytes and are more prone to surface recombination [9].

2H⁺ +2e⁻ ➔H₂ → $2H^+ + 2e^- \rightarrow H_2$
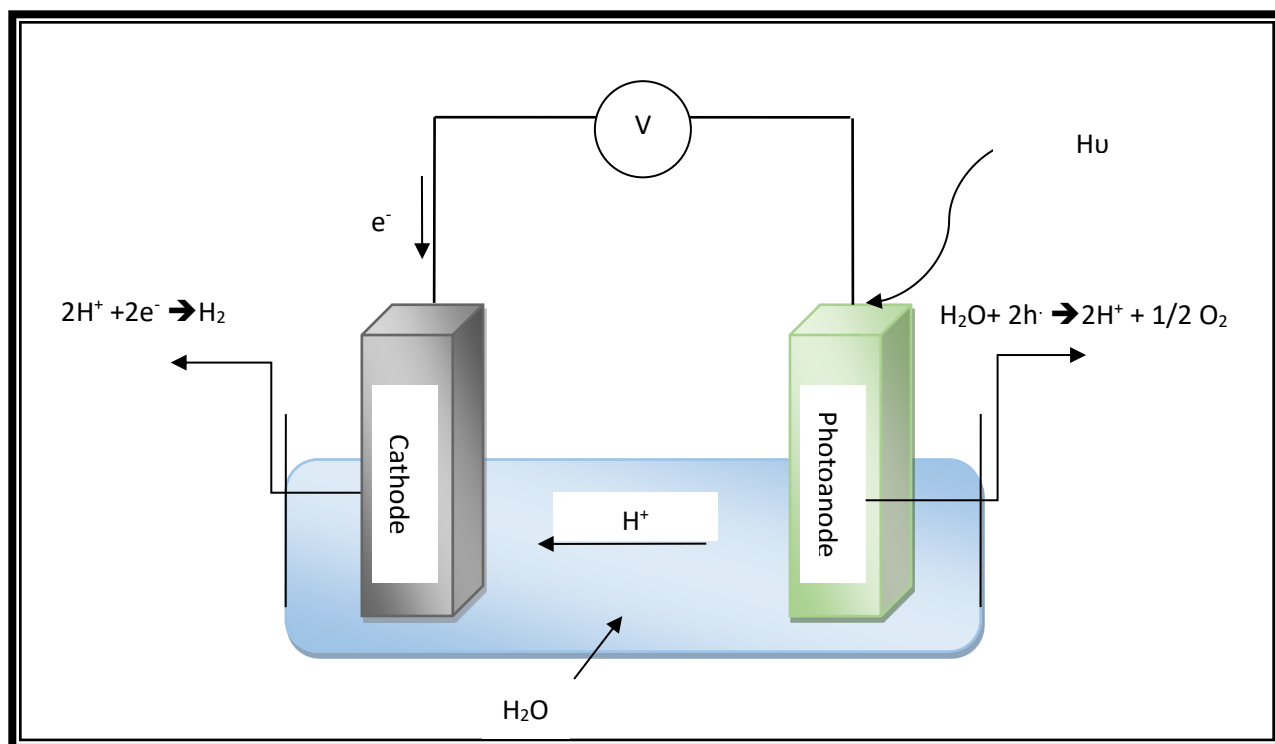
Fig 2.2: Schematic illustration of the photoelectrochemical cell.

Ultimately, the complete water splitting process can be described as:

$$H_2O \rightarrow \frac{1}{2}O_2 + H_2 \qquad (2.1)$$
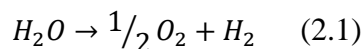
With the half reactions:

$$2H^+ + 2e^- \rightarrow H_2 \qquad (2.2)$$

$$H_2O \rightarrow O_2 + 4H^+ \qquad (2.3)$$
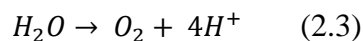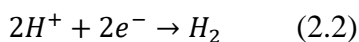
The adequacy of water splitting process relies mainly upon the energy gap and electrochemical potentials of the absorbing material in addition to the charge transfer mechanism. Principally for adequate H_2 generation some substantial factors (controlling parameters) should be fulfilled for ideal performance. Such as:

1. A small semiconductor bandgap (approximately less than 3 eV) in order to respond to visible light
2. The conduction band (CB) and valence band (VB) positions must bracket the redox levels of H_2O
3. The semiconductor should be durable in aqueous environments
4. The semiconductor should be economically available, inexpensive and environmentally inert [7].

2.2.1 Reaction Mechanism

The water splitting reaction using a semiconductor photoanode and a metal-counter cathode includes various stages within the semiconductor and the semiconductor/liquid junction that involves the following: [10, 11]

1. Photoinduced electron-hole pair generation $2h\upsilon \rightarrow 2e^- + 2h^+$ (2.4)
2. OER: anodic water-oxidation half reaction at the photoanode by electron holes
$$H_2O + 2h^+ \rightarrow 2H^+ + \frac{1}{2}O_2(gas)$$ (2.5)
3. Transfer of H^+ ions from the working electrode to the counter electrode via the solution and transfer of electrons from the working electrode to the counter electrode via the back-contact
4. HER: cathodic H^+ reduction half-reaction at the counter electrode by electrons
5. Overall PEC water-splitting reaction $H_2O + 2\upsilon \rightarrow H_2(gas) + \frac{1}{2}O_2(gas)$ (2.6)
6. The overall reaction can only occur when the photon energy harvested by the photoanode is as same as or greater than the outset energy (E):
$$E = \frac{\Delta G^0}{2N_A}$$ (2.7)
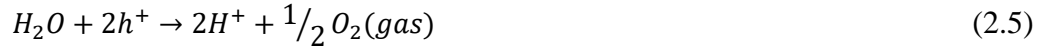
Where ΔG^0 is the Gibbs free energy per mole of reaction = 237.18 kJ mole^{-1} and N_A is Avogadro's number=6.023 x 10^{23} mol^{-1}. Substituting these values in Eq. 2.7 leads to

$$E = h\upsilon = 1.23 \text{ eV}$$ (2.8)

Consequently, the splitting of water is achievable as the electromotive force of the cell (EMF) is equivalent to or larger than 1.23 V. A photon energy of 1.23 eV (a wavelength about 1000 nm) must be attainable for solar-water splitting. Yet, in effect, about 2.0 eV (wavelength of around 620 nm) is needed [6]. The additional energy is to recompense the unavoidable losses due to electrode over potentials, recombination of photoinduced charge carriers and resistances of electrical connections. The predicted value of this aggregate was observed to be approximately 0.8 eV [11].

2.2.2 Physics of Semiconductor/Liquid Contacts

To establish an adequate photoelectrochemical system it is essential to recognize the basic nature of the semiconductor-liquid junction that is grown when the light sensitive material is submerged in an electrolyte. Figure 2.3 represents the energy diagram of the water splitting system. In Figure 2.3a, no contact was developed among the two electrodes, at the time of contact (absence of light) (Figure 2.3b) the Fermi level of the photoanode should be in balance with that of the solution by transport of electrons from the photoanode (higher work function) to the solution (lower work function). This creates a space vacant of electrons in the photoanode identified as the space charge region. The positively charged layer grabs negatively charged species from the solution developing an extremely thin (<1nm) layer called Helmholtz layer. The

equilibrium between the electrochemical potentials causes band bending. Upon illumination of the photoanode (Figure 2.3c), the absorbed photons generate electron-hole pair that are separated via the electric field in the depletion region. The photogenerated electrons react with the positive species in the space charge layer and decrease the band bending while the photogenerated holes flow to the junction among the semiconductor and the electrolyte to generate oxygen. Nonetheless, the Fermi level of the counter electrode is at lower potential with respect to the hydrogen evolution potential and thus hydrogen production is not possible. When an external voltage is applied (Figure 2.3d) the Fermi level of the counter electrode can be lifted over the hydrogen evolution potential, allowing the water splitting reaction to advance [5].
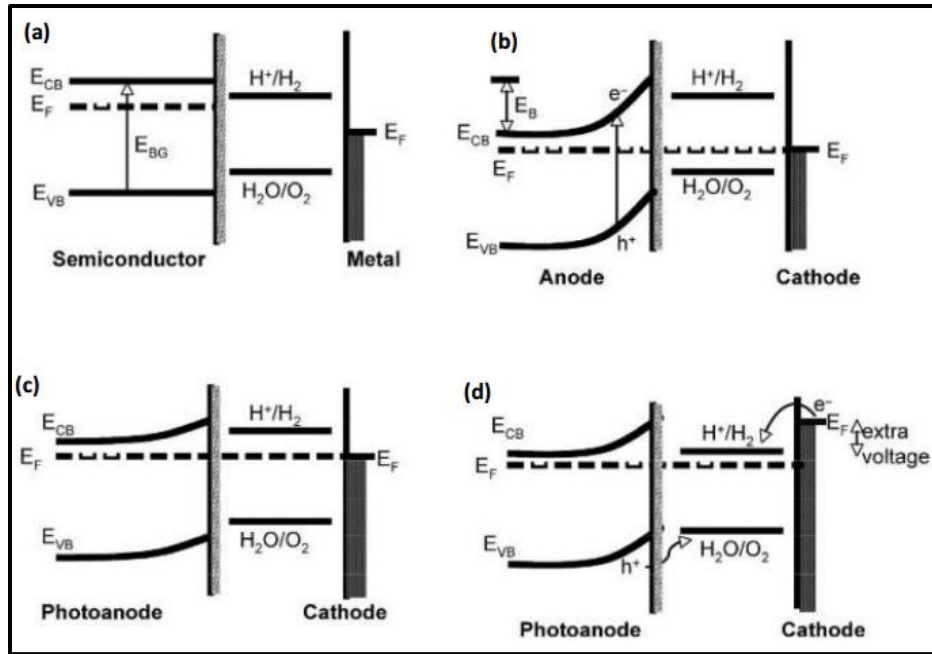
Figure 2.3: Energy diagram of a two-electrode PEC cell with n-type semiconductor photoanode and metal counter cathode: (a) No contact, (b) Equilibrium in dark, (c) Equilibrium under the effect of light, (d) Illumination under external bias [5].

2.3 Material Concerns

Considering that the semiconductor-liquid interrelation follows various stages involving many physical and chemical aspects, there are various material concerns that are required such as: appropriate band gap, significant corrosion resistance and fast charge transfer properties.

2.3.1 Band Gap

The band gap is the energy gap between the valence band maximum (VBM) and the conduction band minimum (CBM). As mentioned before in section 2.2.1, the minimum required band gap for adequate light absorption properties is approximately equal to 2 eV. Figure 2.4 shows band gaps of several semiconductors varying from 2.3 to 3.7 eV versus the vacuum level and normal hydrogen electrode (NHE). It is worth mentioning that materials having suitable band gaps such as GaP (E_g=2.23 eV) [12] and GaAs (E_g=1.4 eV) [12] were found to be very prone to photocorrosion problems. Whereas other materials such as In_2O_3 (E_g= 2.6 eV) [12] with indirect band gap will need greater energies than their analogous band gaps [13]. Seemingly, the

materials that maintain band gap requirements and photocorrosion stability are representing a complex criteria that are necessary in photoelectrochemical cells.
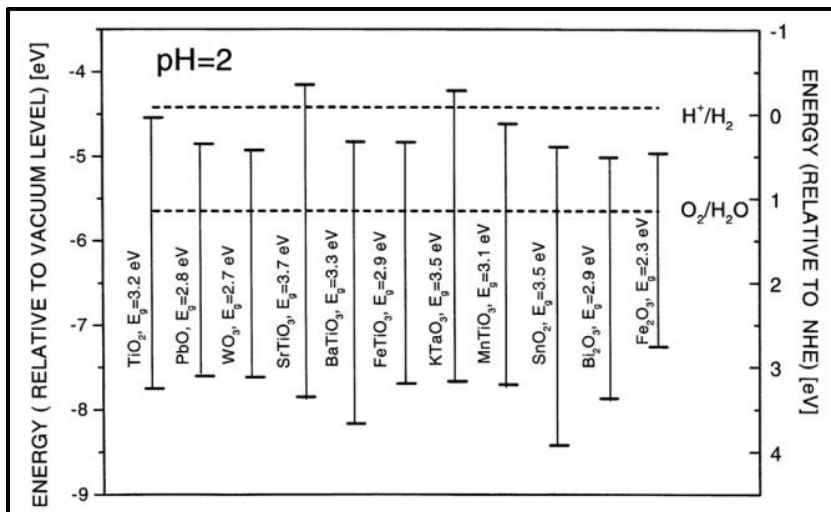
Figure 2.4: Band gap energies of various semiconductors and relative energies with reference to vacuum level and NHE [11].
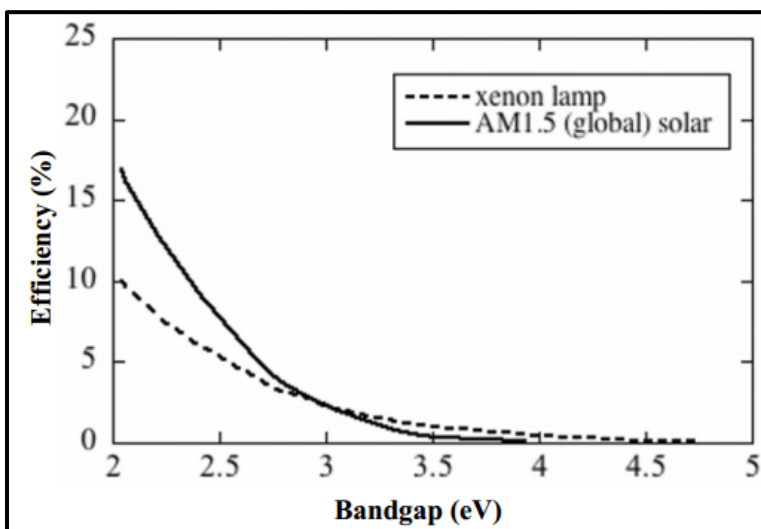
Figure 2.5: The maximum efficiency attainable by a photoanode with respect to its band gap [5]

2.3.2 Photocorrosion Stability

Since water (pH=7.0) is considered to be an inadequate ionic conductor, and thus provides a large Ohmic overpotential, it is rarely used as an electrolyte for produce hydrogen via water electrolysis. In order for the photoelectrochemical process to advance at an adequate cell potential, the conductivity of water should be enhanced by the accretion of acids or alkalis. Aqueous acidic and alkaline solutions provide high ionic (hydrogen and hydroxyl) concentration and mobility and will result in less electrical resistance. In general, basic electrolytes are usually favored because corrosion issues are significant with acidic electrolytes [14].

It is crucial for the semiconductor electrode to be stable and extremely resistant to photocorrosion reactions that could lead to the degradation of its properties. That is, the photoinduced electron-hole pairs can reduce or oxidize the semiconductor itself. Some metal oxides such as TiO_2 are exceptionally resistant to these photocorrosion reactions. And hence, they are highly desirable for electrochemical water splitting.

The electrochemical corrosion of an AB semiconductor that may bring on anodic or cathodic decomposition, could be illustrated by the subsequent relations.

$$AB + nh^+ \rightarrow A^{n+} + B + \Delta G_a \qquad\qquad E_{p,d} = \frac{\Delta G_a}{nN_A} \qquad\qquad (2.9)$$

$$AB + ne^- \rightarrow B^{n-} + A + \Delta G_c \qquad\qquad E_{n,d} = \frac{\Delta G_c}{nN_A} \qquad\qquad (2.10)$$

Where n represents the number of electrons or holes, ΔG_a and ΔG_c are the free energy change at both the anode and cathode respectively, $E_{p,d}$ is the free enthalpy of oxidation and $E_{n,d}$ is the free enthalpy of reduction [11].

Gerischer [15] established the next rules to examine the stability of the semiconductor electrodes with respect to electrochemical corrosion for the photoanode and the photocathode respectively:

$$E (O_2/H_2O) < E_{p,d} \qquad\qquad (2.11)$$
$$E (H^+/H_2) > E_{n,d} \qquad\qquad (2.12)$$

Where $E (O_2/H_2O)$ is the energy of the redox couple O_2/H_2O and $E (H^+/H_2)$ is the energy of the redox couple H^+/H_2. Consequently, the narrow energy gap is not solely essential, but also the band positions relative to the oxygen and hydrogen evolution potentials.

Figure 2.6 demonstrates the valence and conduction bands of several semiconductor electrodes regarding the electrochemical potentials O_2/H_2O and H^+/H_2. The pH of the solution can also impact the band potentials as displayed in Figure 2.7 for TiO_2.
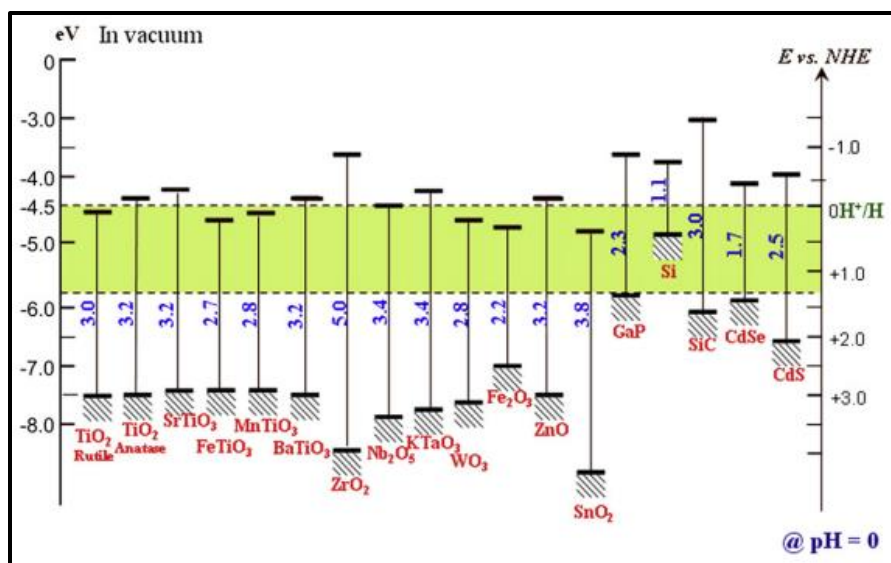
Figure 2.6: Band gap position for various semiconductors with respect to vacuum level and NHE [16].
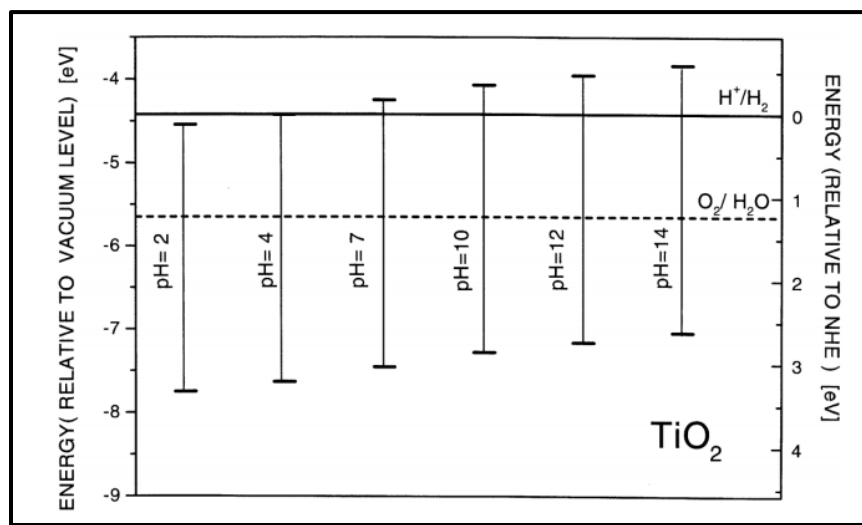
Figure 2.7: pH dependence of the band energies of TiO₂ relative to the vacuum level and NHE [11].

2.3.3 Structure

With the advent of nanomaterials, several semiconductors including those that have been studied before have gained great attention to be utilized in water splitting applications. As nanomaterials acquire characteristics that are totally distinctive from those of their bulk analogues, any modification in chemical bonding, structure geometry, mechanical strength, electrical properties or even melting point may lead to the fabrication of a very promising material for water splitting applications [17].

Principally, the utilization of nanoparticulate photoanodes with a diameter ranging from some micrometers to numerous nanometers was originally utilized for water splitting applications in 1980s [18-20]. However there were several reports declaring the use of nanoparticle photoanodes before this time and onwards [21, 22]. Nanoparticulate systems can provide high efficiencies, due to the high specific surface area. This will enhance the entire active area for the water splitting reaction. Another advantage would be the large effective

17

optical path of photons that results in better absorption properties [22]. Nonetheless, in nanoparticulate photoanodes, the electron transport is described by random walk mechanism and photogenerated electrons are vulnerable to recombination at the grain boundaries within the particulates. This leads to doubling the electron pathway length and as a result a delayed electron diffusion through the nanoparticle system [22, 23]. Favorably, nanotubular structures with vertical orientation can overcome recombination losses at grain boundaries by providing vectorial charge transfer across the wall thickness of the tubes while energy harvesting takes place across their lengths [24]. This makes the e-h recombination losses lower for 1D structures when compared to 3D structures [25] as described in Figure 2.8.
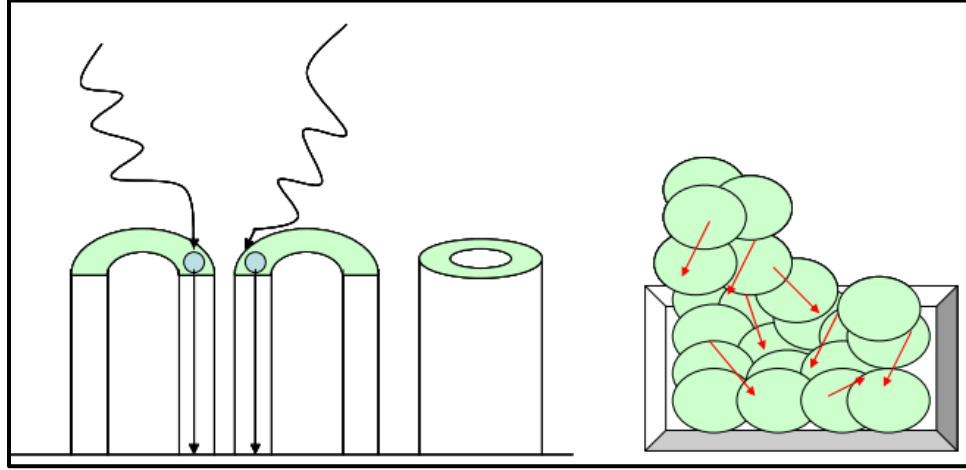
Figure 2.8: Schematic illustration of electron transport mechanism through (a) Nanotubes and (b) Nanoparticles [9].

2.4 Efficiency

The solar-to-hydrogen conversion efficiency (STH) characterizes the total adequacy of a PEC setup subjected to wide range of solar emissions (AM 1.5 G) under zero voltage where all the energy needed for the water splitting reaction is afforded by electromagnetic radiation. For an explicit solar-to-hydrogen behavior, STH is denoted as chemical energy of the hydrogen generated divided by direct photon energy input. The chemical energy of the hydrogen generated is expressed as the rate of hydrogen generation (mmole H_2/s) multiplied by the Gibbs free energy per mole of H_2 (ΔG^0 =237 kJ/mol at 25 °C), whereas the direct photon energy from sunlight is the direct irradiance power density (P_{total}, mW cm^{-2}) multiplied by the exposed area of the electrode (cm^2).

STH= [(mmole H_2 /s) x (237,000 J/mol)] / [P_{total} (mW cm^{-2}) x Area (cm^2)] AM 1.5 G   (2.13)

Preferably, using the equation that power is the multiplication of potential, current and the faradic efficiency of hydrogen production (η_F)

STH= [| (J_{SC} mA /cm^2) | X (1.237 V) X η_F / P_{total} (mW cm^{-2})] AM 1.5 G
        (2.14)

Where, J_{SC} is the short-circuit photocurrent density normalized to the exposed area of the electrode and the voltage 1.23 V is the thermodynamic water-splitting potential (based on ΔG^0) [26].

2.5 Structural Properties of TiO$_2$

Besides being cheap, non-toxic and chemically stable, the electronic properties of TiO$_2$ have made it a promising candidate for several practical applications such as environmental [27], biomedical [28], photovoltaic [29] and photocatalytic [30]. TiO$_2$ can be found in either crystalline or amorphous forms. The amorphous form is photocatalytically unstable [31]. There are three crystalline phases of TiO$_2$; anantase, rutile and brookite [31]. Brookite is rarely available and is limited for photocatalytic applications. Both anatase and rutile have been considerably investigated for photoelectrochemical purposes with the former being more competent for photocatalytic reactions [31]. Both anatase and rutile are tetragonal in the unit cell structure and can be expressed as groups of TiO$_6$ octahedra, where every Ti^{4+} ion is enclosed by six O^{2-} ions octahedron [32]. The two crystal structures differ in the arrangement of each octahedron and by the distribution of the octahedral groups. In rutile, the octahedron behaves in an orthorhombic arrangement, while, in anatase the octahedron is greatly altered with lower symmetry than orthorhombic. The Ti-Ti distance in anatase is longer than that of the rutile, while the Ti-O distance is much smaller. These discrepancies in the crystal orientation lead to different mass densities as well as different electronic characteristics among the two structures of TiO$_2$ [32].
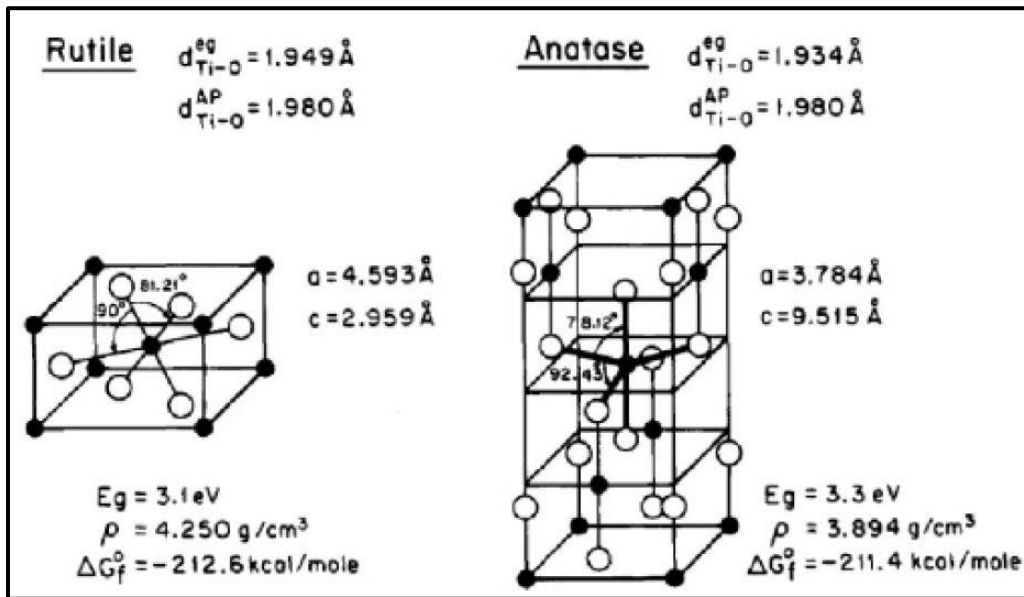
Figure 2.9: Structural orientation of Rutile and Anatase TiO$_2$ [32].

2.5.1: Ordered Array of TiO$_2$ Nanotubes

In an attempt to enhance the light collection and charge separation properties in TiO$_2$ photoanodes, extensive effort has been carried out to develop intricate structures such as nanotubes, nanorods or nanowires. Previous work related to the preparation and characterization of TiO$_2$ nanotubes was performed by Grimes [33] and lately by Schmuki et.al [34] and Misra and co-workers [35]. Up till now, several trials have been successfully carried out to fabricate TiO$_2$ nanotubes, involving hydrothermal method [36], sol-gel process [37] and templating approaches [38]. Nonetheless most of these techniques are sophisticated and expensive, which will apparently restrain the utilization of complex nanostructure in practical applications [39]. On the

other hand, the electrochemical anodization approach is considered a very favorable technique to prepare TiO_2 nanotube arrays because of being cheap, simple and reliable thus can be regarded as an effective method for large-scale production [40].

2.5.2: Mechanism of Anodically Fabricated TiO₂ Nanotube Arrays

Tubular TiO_2 structures are developed by the passage of an electrical potential through a fluoride containing electrolyte between the titanium anode and a platinum cathode, forming TiO_2 nanotube arrays that are perpendicular to the surface of the substrate and maintaining two separate pathways for decisive electron and hole transport [41,42]. The first step in the fabrication of TiO_2 nanotubes is the growth of an oxide layer over the titanium foil governed by the reactions hereinafter: [43]

$$2H_2O \rightarrow O_2 + 4e^- + 4H^+ \qquad (2.15)$$

$$\underline{Ti + O_2 \rightarrow TiO_2 \qquad\qquad\qquad (2.16)}$$

$$Ti + 2H_2O \rightarrow TiO_2 + 4H^+ + 4e^- \qquad (2.17)$$
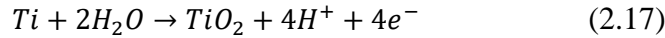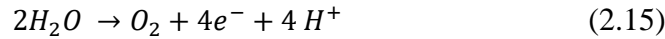
Figure 2.10 displays scanning electron image (SEM) of the oxide layer produced during the development of TiO_2.
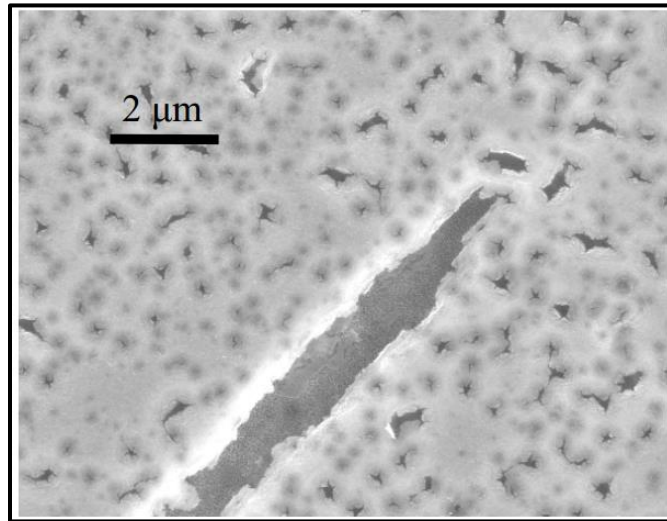
Figure 2.10: SEM image of the oxide layer created during fabrication of TiO₂ nanotubes [43].

The next step after the formation of the oxide layer is pit formation. The existence of a complexing ligand (fluoride ion, F⁻) and the applied voltage cause considerable dissolution of TiO_2 according to Equation 2.18.

$$TiO_2 + 6F^- + 4H^+ \rightarrow TiF_6^{2-} + 2H_2O \qquad (2.18)$$
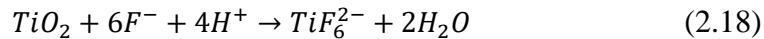
This complex formation causes the wreckage of the oxide layer with disarranged pit formation followed by a nanoporous structure covering uniformly the entire surface. The last step is the nanotubes formation. The Fluoride ion promotes further dissolution leading to the development of vertically-oriented nanotubes straight up to the surface [43].
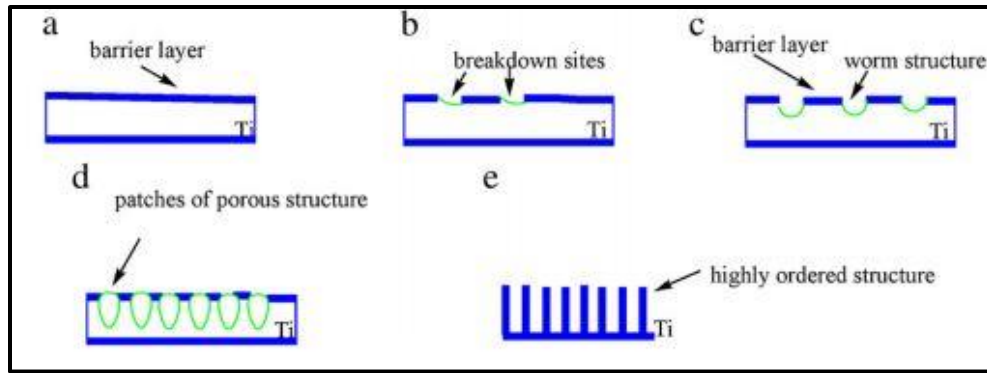
Figure 2.11: Schematic of the development of TiO$_2$ nanotubes synthesized by electrochemical anodization [44].

The development of TiO$_2$ nanotubes via electrochemical anodization can be analyzed by observing the current transient through the electrode. Considering the lower electrical conductivity of the oxide layer with respect to the Ti substrate, its formation is accompanied by an exponential decrease in the current [45]. Subsequently its dissolution, which is accompanied by the formation of a nanoporous structure, can be marked by a minor increase in the current because of the thinner oxide layer present which in turn will make the electrode more conductive. Lastly, the nanotube formation can be expressed by a tapered decrease in the current followed by a slow uniform decrease as oxide formation and dissolution take place at corresponding rates [45]. Figure 2.11 demonstrates the current behavior during the development of TiO$_2$ nanotubes via electrochemical oxidation.
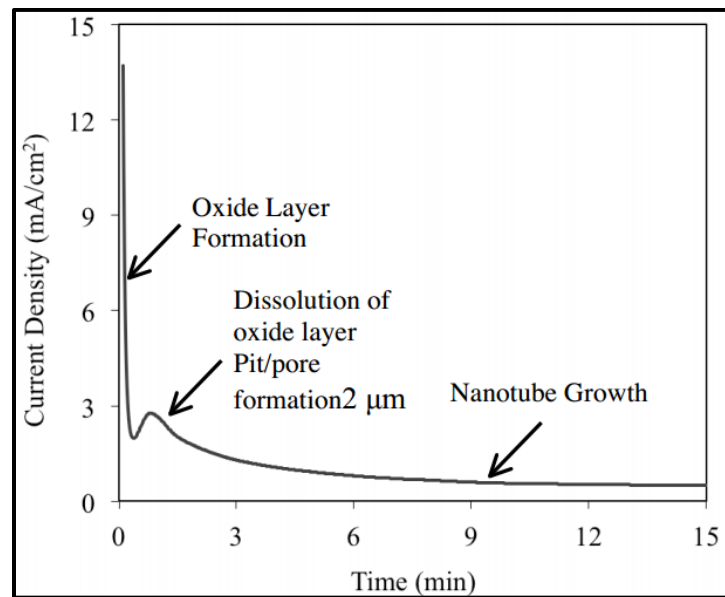
Figure 2.12: Current density behavior due to the applied potential as a function of time during the fabrication of TiO$_2$ nanotubes via electrochemical anodization [45].

21

References

1. N. Lewis and D. Nocera, "Powering the planet: Chemical challenges in solar energy utilization", *Proceedings of the National Academy of Sciences*, vol. 103, no. 43, pp. 15729-15735, 2006.

2. H. Prakasam, "Towards Highly Efficient Water Photoelectrolysis", Ph.D. dissertation, Dept. Elect. Eng., The Pennsylvania State University., Pennsylvania, USA, 2008.

3. Rhode, R. A. Image from Global Warming Art.
   http://en.wikipedia.org/wiki/Image:Solar_Spectrum.png.

4. R. C. C. Memming, *Semiconductor Electrochemistry*. Weinheim: Wiley-VCH, 2015.

5. C. Grimes, O. Varghese and S. Ranjan, "Photoelectrolysis", in *Light, Water, Hydrogen*, 1st ed., Springer US, 2008, pp. 115-190.

6. P. Pérez-Higueras and Fernández Eduardo F., *High concentrator photovoltaics: fundamentals, engineering and power plants*. Cham: Springer, 2015.

7. R. van de Krol, "Principles of Photoelectrochemical Cells", in *Photoelectrochemical Hydrogen Production*, 1st ed., R. van de Krol and M. Grätzel, Ed. Springer US, pp. 13-67, 2012.

8. Y. Smith, "Self-ordering Titania Nanotube Arrays: Electrochemical Anodization, Functionalization, and Application", Ph.D. dissertation, Dept. Metallurgical Engineering., The University of Utah., Utah, USA, 2014.

9. R. Rangaraju, "Synthesis and Characterization of Transition Metal Oxide Nanotubes for Photoelectrochemical Hydrogen Generation", M.S. thesis, Materials Engineering., University of Nevada, Reno., USA, 2009.

10. C. Grimes, O. Varghese and S. Ranjan, "Oxide Semiconducting Materials as Photoanodes", in *Light, Water, Hydrogen*, 1st ed., Springer US, 2008, pp. 191-255.

11. T. Bak, J. Nowotny, M. Rekas, and C. C. Sorrell, "Photo-electrochemical hydrogen generation from water using solar energy. Materials-related aspects," *International Journal of Hydrogen Energy*, vol. 27, no. 10. pp. 991–1022, 2002.

12. M. Pasut, "TiO_2- CdS Nanostructures For Hydrogen Production", Tesi di Laurea Magistrale, Dipartimento Di Ingegneria Industriale., Universita` Degli Studi Di Padova., Padova, Italia, 2013.

13. K. Bohnert, H. Kalt, A. Smirl, D. Norwood, T. Boggess and I. D'Haenens, "Renormalization of Direct and Indirect Band Gaps in Highly Excited AlxGa1−xAs", *Physical Review Letters*, vol. 60, no. 1, pp. 37-40, 1988.

14. C. Grimes, O. Varghese and S. Ranjan, "Hydrogen Generation By Water Splitting", in *Light, Water, Hydrogen*, 1st ed, Springer US, 2008, pp. 35-113.

15. H. Gerischer, "Solar photoelectrolysis with semiconductor electrodes", in *Topics in Applied Physics Solar Energy Conversion*, Berlin, Heidelberg: Springer-Verlag, 1979, pp. 115–172.

16. D. Jing, L. Guo, L. Zhao, X. Zhang, H. Liu, M. Li, S. Shen, G. Liu, X. Hu and X. Zhang, "Efficient solar hydrogen production by photocatalytic water splitting: From fundamental study to pilot demonstration", *International Journal of Hydrogen Energy*, vol. 35, no. 13, pp. 7087-7097, 2010.

17. V. Satsangi, S. Kumari, A. Singh, R. Shrivastav and S. Dass, "Nanostructured hematite for photoelectrochemical generation of hydrogen", *International Journal of Hydrogen Energy*, vol. 33, no. 1, pp. 312-318, 2008.

18. S. Sato and J. White, "Photodecomposition of water over Pt/TiO$_2$ catalysts", *Chemical Physics Letters*, vol. 72, no. 1, pp. 83-86, 1980.

19. K. Domen, S. Naito, M. Soma, T. Onishi and K. Tamaru, "Photocatalytic decomposition of water vapour on an NiO–SrTiO3catalyst", *J. Chem. Soc., Chem. Commun.*, no. 12, pp. 543-544, 1980.

20. K. Domen, A. Kudo and T. Onishi, "Mechanism of photocatalytic decomposition of water into H$_2$ and O$_2$ over NiO-SrTiO$_3$", *Journal of Catalysis*, vol. 102, no. 1, pp. 92-98, 1986.

21. G. Schrauzer and T. Guth, "Photolysis of water and photoreduction of nitrogen on titanium dioxide", *Journal of the American Chemical Society*, vol. 99, no. 22, pp. 7189-7193, 1977.

22. K. Maedaa, "Photocatalytic water splitting using semiconductor particles: History and recent developments", *Journal of Photochemistry and Photobiology C: Photochemistry Reviews*, vol. 12, no. 4. pp. 237–268, 2011.

23. M. Law, L. Greene, J. Johnson, R. Saykally and P. Yang, "Nanowire dye-sensitized solar cells", *Nature Materials*, vol. 4, no. 6, pp. 455-459, 2005.

24. N. Beermann, L. Vayssieres, S.-E. Lindquist, and A. Hagfeldt, "Photoelectrochemical Studies of Oriented Nanorod Thin Films of Hematite", *Journal of The Electrochemical Society*, vol. 147, no. 7, pp. 2456–2461, 2000.

25. S. Mohapatra, S. John, S. Banerjee and M. Misra, "Water Photooxidation by Smooth and Ultrathin α-Fe_2O_3 Nanotube Arrays", *Chemistry of Materials*, vol. 21, no. 14, pp. 3048-3055, 2009.

26. Z. Chen, H. N. Dinh, E. Miller, "Efficiency Definitions in the Field of PEC", in *Photoelectrochemical water splitting: standards, experimental methods, and protocols*, New York: Springer, 2013, pp. 7–16.

27. Q. Zhang, H. Xu, and W. Yan, "Highly Ordered TiO_2 Nanotube Arrays: Recent Advances in Fabrication and Environmental Applications—A Review", *Nanoscience and Nanotechnology Letters*, vol. 4, no. 15. pp. 505–519, 2012.

28. K. M. Kummer, E. Taylor, and T. J. Webster, "Biological Applications of Anodized TiO_2 Nanostructures: A Review from Orthopedic to Stent Applications", *Nanoscience and Nanotechnology Letters*, vol. 4, no. 5. pp. 483–493, 2012.

29. G. Mor, K. Shankar, M. Paulose, O. Varghese and C. Grimes, "High efficiency double heterojunction polymer photovoltaic cells using highly ordered TiO_2 nanotube arrays", *Applied Physics Letters*, vol. 91, no. 15, p. 152111, 2007.

30. A. Kubacka, M. Fernandez-García, and G. Colon, "Advanced Nanoarchitectures for Solar Photocatalytic Applications", *Chem. Rev.*, vol. 112, no. 3. pp. 1555–1614, 2012.

31. T. Zhu and S. Gao, "The Stability, Electronic Structure, and Optical Property of TiO_2 Polymorphs", *The Journal of Physical Chemistry C*, vol. 118, no. 21, pp. 11385-11396, 2014.

32. X. Chen and S. S. Mao, "Titanium Dioxide Nanomaterials: Synthesis, Properties, Modifications, and Applications," *Chem. Rev.*, vol. 107, no. 7. pp. 2891–2959, 2007.

33. C. Grimes, "Synthesis and application of highly ordered arrays of TiO_2 nanotubes", *Journal of Materials Chemistry*, vol. 17, no. 15, pp. 1451-1457, 2007.

34. Y. Nah, I. Paramasivam and P. Schmuki, "Doped TiO_2 and TiO_2 Nanotubes: Synthesis and Applications", *ChemPhysChem*, vol. 11, no. 13, pp. 2698-2713, 2010.

35. Y. R. Smith, R. S. Ray, K. Carlson, B. Sarma, and M. Misra, "Self-Ordered Titanium Dioxide Nanotube Arrays: Anodic Synthesis and Their Photo/Electro-Catalytic Applications," *Materials*, vol. 6, no. 7. pp. 2892–2957, 2013.

36. A. Nakahira, T. Kubo and C. Numako, "Formation Mechanism of TiO_2-Derived Titanate Nanotubes Prepared by the Hydrothermal Process", *Inorganic Chemistry*, vol. 49, no. 13, pp. 5845-5852, 2010.

37. T. Kasuga, M. Hiramatsu, A. Hoson, T. Sekino and K. Niihara, "Formation of Titanium Oxide Nanotube", *Langmuir*, vol. 14, no. 12, pp. 3160-3163, 1998.

38. R. Wang, X. Cai and F. Shen, "Preparation of TiO_2 hollow microspheres by a novel vesicle template method and their enhanced photocatalytic properties", *Ceramics International*, vol. 39, no. 8, pp. 9465-9470, 2013.

39. P. Simon and Y. Gogotsi, "Materials for electrochemical capacitors", *Nature Materials*, vol. 7, no. 11, pp. 845-854, 2008.

40. K. Xie, J. Li, Y. Lai, W. Lu, Z. Zhang, Y. Liu, L. Zhou and H. Huang, "Highly ordered iron oxide nanotube arrays as electrodes for electrochemical energy storage", *Electrochemistry Communications*, vol. 13, no. 6, pp. 657-660, 2011.

41. J. Macak, H. Tsuchiya, A. Ghicov, K. Yasuda, R. Hahn, S. Bauer and P. Schmuki, "TiO_2 nanotubes: self-organized electrochemical formation, properties and applications", *Current Opinion in Solid State and Materials Science*, vol. 11, no. 1-2, pp. 3-18, 2007.

42. J. Wang and Z. Lin, "Freestanding TiO_2 Nanotube Arrays with Ultrahigh Aspect Ratio via Electrochemical Anodization", *Chemistry of Materials*, vol. 20, no. 4, pp. 1257-1261, 2008.

43. G. Mor, O. Varghese, M. Paulose, K. Shankar and C. Grimes, "A review on highly ordered, vertically oriented TiO_2 nanotube arrays: Fabrication, material properties, and solar energy applications", *Solar Energy Materials and Solar Cells*, vol. 90, no. 14, pp. 2011-2075, 2006.

44. J. Wan, X. Yan, J. Ding, M. Wang and K. Hu, "Self-organized highly ordered TiO_2 nanotubes in organic aqueous system", *Materials Characterization*, vol. 60, no. 12, pp. 1534-1540, 2009.

45. V. Prida, E. Manova, V. Vega, M. Hernandez-Velez, P. Aranda, K. Pirota, M. Vázquez and E. Ruiz-Hitzky, "Temperature influence on the anodic growth of self-aligned

Titanium dioxide nanotube arrays", *Journal of Magnetism and Magnetic Materials*, vol. 316, no. 2, pp. 110-113, 2007.

Chapter 3

Review of Relevant Literature

3.1 Alkali Metal Modified TiO$_2$ Photoanodes

Anodically-fabricated TiO$_2$ nanotubes are regarded as adequate materials for use as photoanodes in the photoelectrochemical cell, owing to their favorable properties such as abundance, stability, quantum confinement effects and their very large specific area [1]. Yet, considering their intrinsic band gap (3.2 eV), only photocatalysis using UV spectrum (which comprises about 5% of the entering sun light on the earth's surface) is achievable. On the contrary, the visible range amounts to nearly 45% of the sun's spectrum. Thus, any modification in the optical sensitivity of TiO$_2$ nanotubes from the UV to the visible range, and at the same time retaining its robust properties will yield a more enhanced photoelectrochemical performance. In this regard, compositional doping of TiO$_2$ utilizing several elements constitutes one of the promising pathways for band engineering [2]. Among these dopants, alkali metals have shown very appealing results in improving the performance of TiO$_2$ in water splitting. Using alkali metals is expected to lower the overall work function due to their low first ionization potential [3].

With regards to the applications of photocatalytic decomposition of organic pollutants, Brezova et al. showed that Li$^+$/ TiO$_2$ layers fixed on glass fibers prepared by sol-gel technique exhibit higher photoactive performance in the rate of phenol decomposition with respect to TiO$_2$ layers formed without Li addition. It was suggested that the surface charge of Li$^+$/ TiO$_2$ can considerably enhance the adsorption of phenol (K$_{ph}$). The isoelectric point was measured as a proof of concept and showed an enhancement for the doped sample over the pure TiO$_2$ as depicted in Figure 3.1. The authors illustrated that the lagre adsorption constant attained by the photocatalyst doped with Li ions makes it more powerful in the photodegradation of phenol [4].
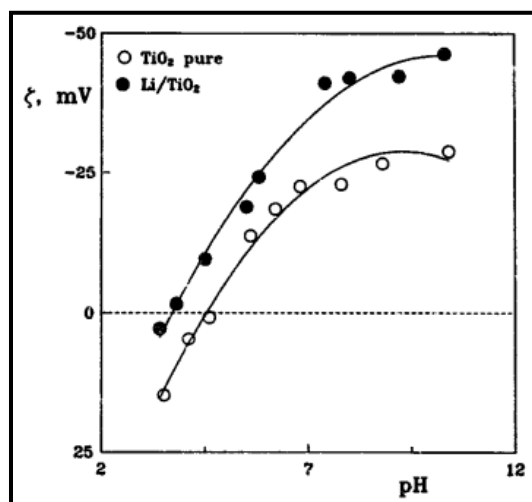
Figure 3.1: Dependence of Zeta potential on the pH at 25°C for TiO₂ photocatalysts prepared by sol-gel approach [4].

On the other side, Lopez et al. examined the Li ion influence on the photoactive performance of sol-gel titania for the degcomposition of 2,4-dinitroaniline. The outcomes indicate that the photoactive performance of Li/TiO$_2$ is slightly lower with respect to that of pristine TiO$_2$. The unimportant influence of lithium was mainly attributed to its role in prohibiting the reaction rate by trapping either electrons or holes that originate during UV illumination. Additionally, the authors claimed that lithium may be found as Li-O replacing Ti^{4+} in the titania network due to its comparable ionic radius (0.60 Å) to that of Ti^{4+} (0.68 Å) acting as an electron trap or it may be found as an interstitial Li^0 (due to the high reducing role reported for the dehydroxylation) acting as a hole trap [5].

With the same explanation of electron/hole trapping in coupling TiO$_2$ with metal dopants, Choi et al. examined the effect of lithium on TiO$_2$ colloids (transparent particle suspensions) formed by the hydrolysis of titanium tetraisopropoxide in the existence of added metal salt LiOH. The photoactive performance of the doped material was assessed regarding both the conduction band electron reduction of an electron acceptor (CCl$_4$dechlorination) and the valence band hole oxidation of an electron donor (CHCl$_3$ decomposition). Particularly, the authors elucidated that the dopant should play the role of both an electron trap and a hole trap in order to enhance the photoactivity. It was observed that trapping either an electron or a hole solely is incompetent since the movable charge carrier will readily recombine with its trapped counterpart. The authors further explained, that all the dopants having closed-shell electronic configuration, such as Li, will exhibit a minor impact on the photoactivity because the stability of the tight electronic configuration keeps an electron or a hole trapping unlikely to happen [6].

In this context, an important conclusion can be drawn from these studies that the influence of a metal ion dopant relies mainly upon either it can act as an intermediary of charge transfer or a recombination site. This is originally ascribed to the positions of the band edges of the dopant within the TiO$_2$ lattice. Consequently, improving the interfacial charge transfer seems to be a crucial parameter in enhancing the photoactivity of doped TiO$_2$.

In consideration of studying the influence of the preparation techniques and the thermal treatments, Bouattour et al. reported on the fabrication of a Li doped TiO$_2$ photocatalyst prepared by sol-gel technique and solid-state sintering. They examined the photocatalytic activity for decomposition of several organic models. The XRD patterns of the fabricated samples showed that TiO$_2$ doped with 1% Li$^+$ and 7% Li$^+$ (relative to the molar fraction of TiO$_2$) possess a mixture of anatase and rutile phases. Whereas the TiO$_2$ structure doped with 3% Li$^+$ appears to rely upon the preparation technique. That is, for the sol-gel route, a mixture of anatase and rutile phases existed, while for the solid-state sintering only anatase phase was formed associated with some species of spinel phase (Li$_4$Ti$_5$O$_{12}$) as seen in Figure 3.2a. It seems that doping TiO$_2$ with Li$^+$ expedites the anatase-rutile transformation [7].

These results were verified by the diffuse reflectance spectra (DRS) which revealed that 1% and 3% Li$^+$ doped TiO$_2$ samples prepared by sol-gel exhibit rutile-type absorption where they can absorb at lower energies. While, the 3% Li$^+$ doped TiO$_2$ samples prepared by solid-state sintering are in a middle position between pure rutile and pure anatase. This illustrates the improvement of the photoactive performance of the samples developed by sol-gel as shown in

Figure 3.2b and c. Table 3.1 summarizes the corresponding band gap values for each catalyst. Furthermore, the influence of the calcination temperature on the photoactive performance was also considered adopting 2-naphthol as a solute model. The outcomes displayed in Figure 3.2d illustrate a great reliance of the photoactive efficiency on the calcination temperature. That is, after 7 hours the remaining concentrations achieved by 1% Li doped TiO_2 sample calcined at 400°C, 600°C and 800°C were 34, 39 and 90% respectively [7].
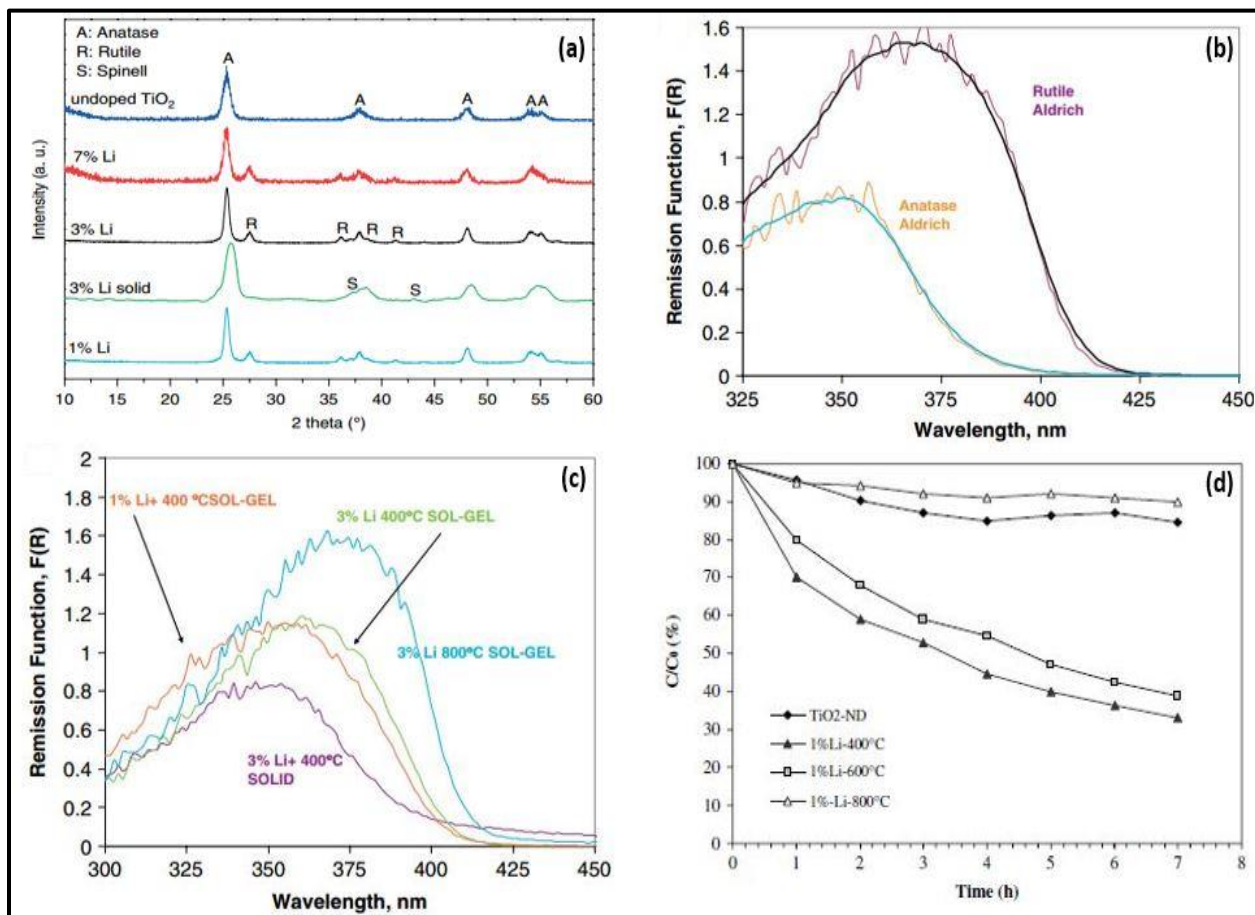
Figure 3.2: (a) XRD patterns of undoped, 3% Li^+ solid sintering and X% (X=1, 3 and 7) Li^+ sol-gel samples calcined at 400 °C, (b) Diffuse reflectance spectra of rutile and anatase, (c) Diffuse reflectance spectra of 1% Li^+ 400 °C sol-gel, 3% Li^+ 400 °C sol-gel, 3% Li^+ 800 °C sol-gel and 3% Li^+ 400 °C solid sintering, (d) Impact of calcination temperature on the photodegradation of 2-naphthol by TiO_2 doped with 1% Li and treated at various temperatures [7].

Table 3.1: The estimated band gap values and absorption edges for rutile, anatase and Li$^+$ doped samples [7].

	E_g (eV)^a	λ_{abs}^{max} (nm)	λ_{emi}^{max} (nm)
Undoped rutile	3.02	367	–
Undoped anatase	3.23	350	–
3% Li solid 400 °C	3.11	350	–
3% Li sol–gel 400 °C	3.05	363	–
1% Li sol–gel 400 °C	3.08	355	–
3% Li sol–gel 800 °C	3.03	368	724

The authors inferred that the coexistence of both anatase and rutile phases in the sol-gel prepared samples could account for their higher photoactivity, which is consistent with the behavior observed by Chen et al [8] who claimed that TiO$_2$ including either anatase or rutile solely is less efficient than TiO$_2$ including both phases for photodecomposition under UV irradiation.

It is also worth mentioning that the results reported by Bouattour et al. are contradicting to those expressed by Lopez et al., who reported an unfavorable consequences on the photocatalytic activity due to the existence of Li in the TiO$_2$ framework. We have to consider the different experimental procedures adopted by both groups. Lopez et al. achieved the gelification by adding a certain quantity of water containing LiCl to a solution of titanium n-butoxide Ti(OBu)$_4$, while Bouattour et al performed the gelification in acetic acid in the presence of HCl. The discrepancy in the gelification method could lead to different structures on the gel network as well as different dispersions of the dopant within the gel [5, 7].

With the same explanation of varying the preparation procedures, Bessekhouad et al. verified the concept using x% Li-doped TiO$_2$ synthesized by two different methods: sol-gel technique (x= 0, 1, 3, 5) and impregnation technology (x= 1, 3, 5) for the decomposition of Malachite green oxalate (MG), 4-hydroxybenzoic acid (4-HBZ) and benzamide (BZ). The results obtained in Figure 3.3a and b show that the preparation technique has a great influence on the efficiency of the catalyst to decompose 4-HBZ. For the sol-gel route, all Li doped samples exhibited an inferior photocatalytic efficiency. The authors reported that whatever the doping level was, the half-life of the 4-HBZ was at worst twice that of the undoped material. In contrast, the samples prepared by the impregnation technique showed a slight enhancement particularly for the 1% Li-doped TiO$_2$, whereas, at higher doping levels unfavorable behavior was observed and the half-life of 4-HBZ increased with increasing the doping level. In addition, the photoactive performance for benzamide degradation displayed in Figure 3.3 c and d reveals a crucial enhancement on the efficiency of all doped samples developed by sol-gel especially for the 5% Li-doped TiO$_2$, where the half-life of the pollutant is about 4 times less than that of the pure TiO$_2$. While, the samples prepared by impregnation showed deactivation of the catalyst regardless of the Li concentration. Additionally, two definite and contradicting aspects were

observed for the behavior of Li-doped TiO$_2$ on the half-life of MG (see Figure 3.3 e and f). The sol-gel samples showed a dramatic deactivation for all samples except for the 5% Li-doped TiO$_2$ which exhibited a slight shorter half-life. Whereas, the samples prepared by impregnation method showed a considerable enhancement for the catalyst above 1%Li. The authors justified the phenomenon to be related to the allocation of lithium over the TiO$_2$ surface i.e., a homogenous dispersion was obtained by using the sol-gel route while a concentrated dispersion was obtained by using impregnation [9].

Accordingly, the valuable conclusion that can be drawn from the aforementioned studies is that the photoactive performance of doped TiO$_2$ is a very specific issue that strongly related to the inclusion procedures of the dopant into TiO$_2$ lattice as well as the type of the pollutant to degrade.
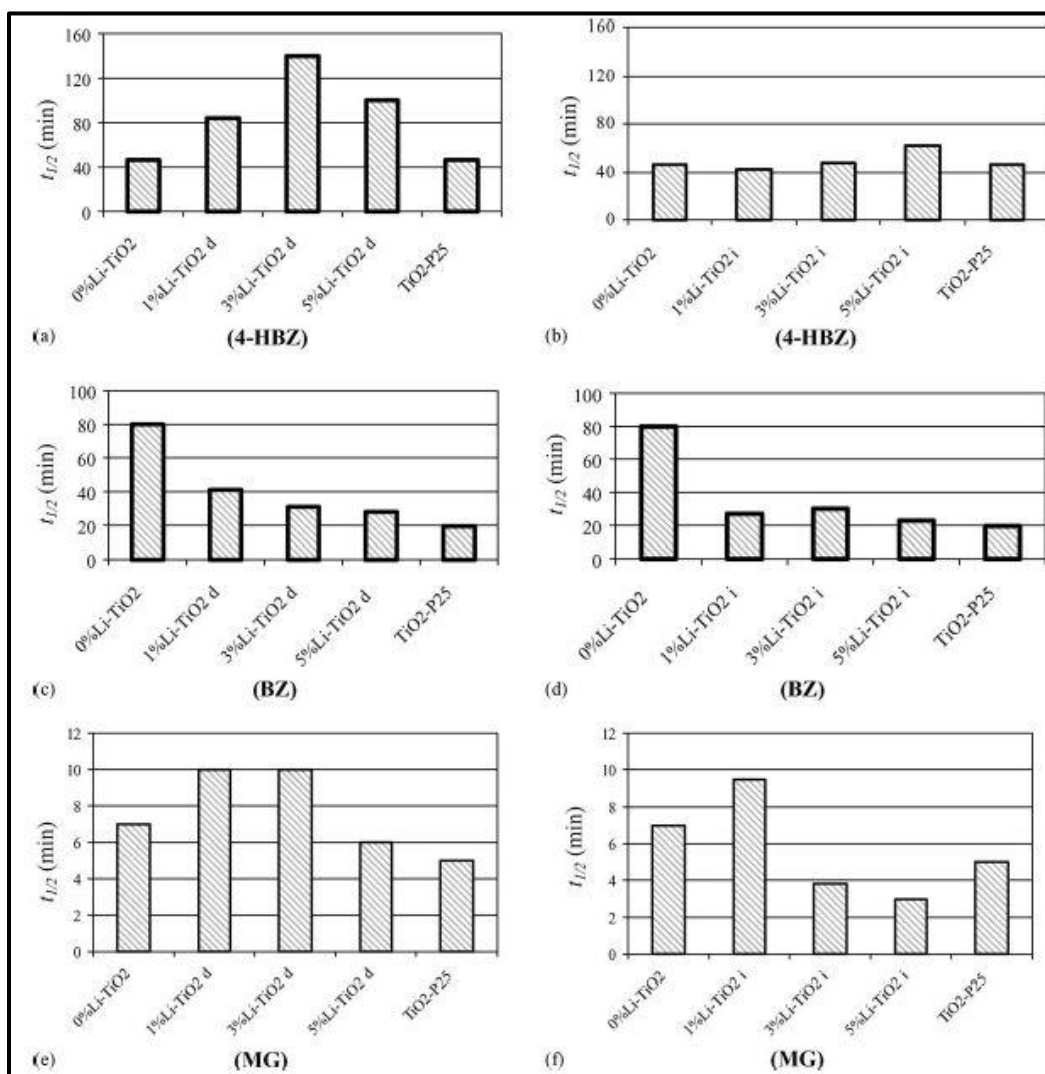
Figure 3.3: Half-life of pollutant degradations as a function of Li doped TiO$_2$ [9].

Along with the previous study, Bessekhouad et al. also examinde the impact of potassium on the photodegradation of MG, 4-HBZ and BZ adopting the same preparation techniques and concentrations reported for Li. The authors assured the same behavior for the photocatalytic activity of TiO_2 verifying the previously revealed conclusion [9].

The effect of potassium was further investigated by Morawski et al. who described the development of K-doped TiO_2 by impregnation technique using KNO_3, K_2CO_3, KOH as well as metallic potassium for the degradation of phenol. It was reported that TiO_2/KNO_3, TiO_2/K_2CO_3 and TiO_2/KOH are inactive on the degradation of phenol. However, using elemental potassium showed a remarkable improvement in the photocatalytic activity over that of pure TiO_2. Table 3.2 shows complete phenol mineralization after 4.5 h under U.V illumination. The authors proposed that the existence of potassium presumably promotes the electron-hole creation [10].

Table 3.2: Relation between phenol concentration and UV illumination time [10].

U.V.-illumination time (h)	Phenol concentration (g/dm^3)
1.5	0.0150
2.0	0.0120
3.0	0.0078
3.5	0.0039
3.75	0.0019
4.0	0.0010
4.5	0.0000

These results contradict those obtained by Grzechulska et al. who revealed that TiO_2/KOH has the optimal photocatalytic activity to decompose oil dispersed in water indicating that the photoelectrode forms mixture of several titanium oxides that are believed to be accountable for the enhancement of the performance [11].

With the same explanation focusing on the effect of different phases and structures present in the TiO_2 network. Cheng et al. examined the photocatalytic performance of tetratitnate $K_2Ti_4O_9$ on the decomposition of phenol. The photoluminescence (PL) spectra shown in Figure 3.4A reveals that the luminescence maximum of $K_2Ti_4O_9$ is blue shifted to 354 nm with respect to that of anatase TiO_2 at 386.8 nm. This implies that the TiO_2 crystallites accountable for the luminescence spectra of $K_2Ti_4O_9$ are much smaller than those of anatase because of the particle size quantization effect which illustrates that the gap between the valence and conduction bands is widened as the particle size of TiO_2 decreases. This behavior was also interpreted by the diffuse reflectance spectra illustrated in Figure 3.4B admitting the blue shift of $K_2Ti_4O_9$ by 0.38 eV with respect to that of anatase TiO_2 and a red shift for rutile that is mainly ascribed to its better atomic orbital overlap because of its more closed packed structure with respect to anatase. On the other hand, the authors further explained that the lower phenol degradation rate achieved by $K_2Ti_4O_9$ with respect to that of anatase TiO_2 is mainly attributed to coke formation on its surface due to the presence of K^+ ions that increases the ion-π electron interaction between the surface and the phenolic intermediates. Thus an important conclusion can be drawn from this

32

study that the crystalline structure and the existence of other chemical constituents may alter the electrostatic field on the surface of the catalyst and hence greatly affect the photoactivity [12].
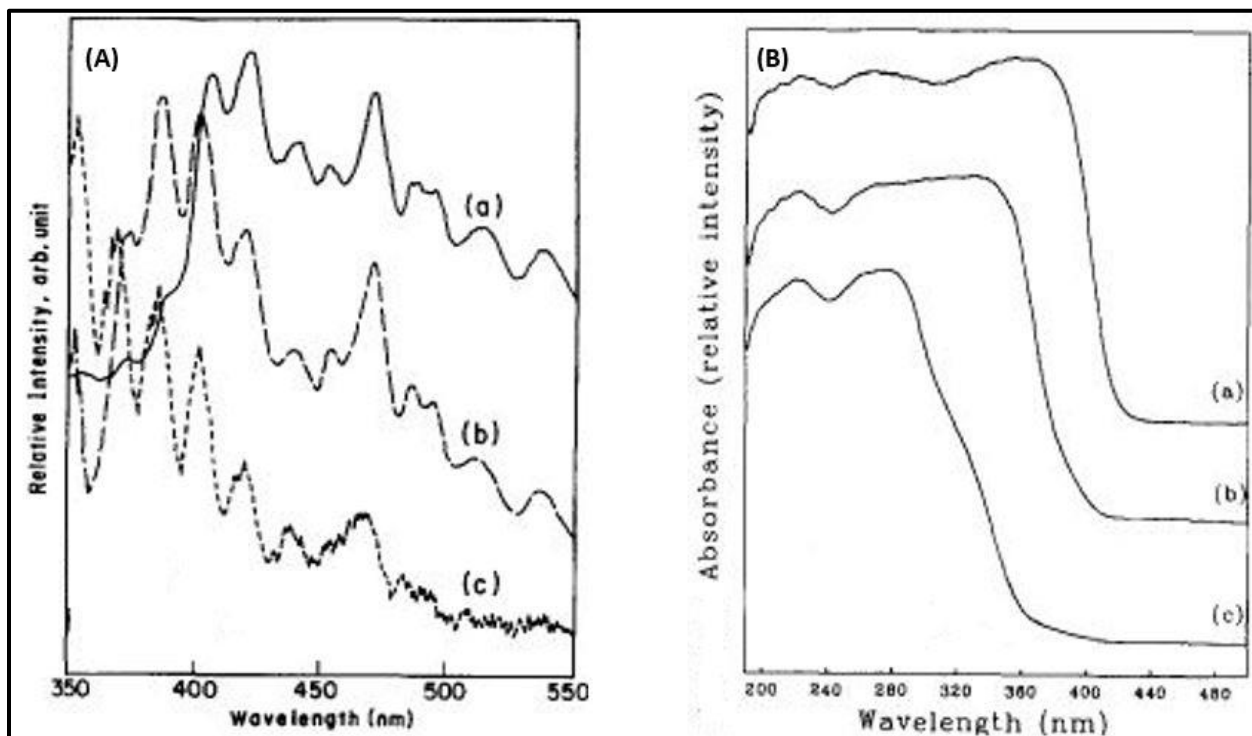
Figure 3.4: (A) Photoluminescence spectra of (a) rutile, (b) anatase and (c) $K_2Ti_4O_9$. (B) Diffuse reflectance spectra of (a) rutile, (b) anatase and (c) $K_2Ti_4O_9$ [12].

For hydrogen production purposes, Richter et al. described the fabrication of vertically-oriented TiO_2 nanotubes containing a definite quantity of surface-adsorbed potassium ions via electrochemical oxidation using potassium containing electrolytes. The authors investigated the surface adsorbed species on the catalyst by near edge X-ray absorption spectroscopy measurements (NEXAFS) as revealed in Figure 3.5. Two definite peaks at 297.6 eV and 300.2 eV are observed for the photoelectrodes synthesized in the potassium containing electrolyte (K2) that are definitely non-existent in the photoelectrodes synthesized without potassium (NH1). These two peaks are attributed to L-edge $2p_{3/2}$ and $2p_{1/2}$ levels, respectively. Also, the NEXAFS results for both samples possesses some characteristics assigned to surface carbon K-edge peaks (258 eV) that are related to any organic acids that might be present in the electrolyte. The solar-water splitting performance was appraised as shown in Figure 3.6 where all the photoelectrodes studied exhibited a reduction in the photocurrent (I_{ph}) and an increase in the bias voltage (V_{bias}) with increasing the potential of the working electrode (V_{WE}). However, It was also shown that the K^+ free sample exhibited maximum photoconversion efficiency $\eta_{c,max}$ at higher values of V_{WE} and correspondingly at higher I_{ph} induced by higher bias voltage, whereas the K^+ containing photoelectrodes showed maximum photoconversion efficiency at lower V_{WE} with lower I_{ph} and lower bias voltage (see the dashed lines of Figure 3.6). These results indicate that the K^+ containing photoelectrodes generate hydrogen at a lower rate than the K^+ free one (as illustrated by the low I_{ph} values) but also need a considerably less energy input per liter of hydrogen

generated (as illustrated by the low V_{bias} values). The authors assigned the obtained results to the existence of surface-adsorbed K^+ ions that modify the energy states of the K^+ containing photoelectrodes by pinning the electrochemical potentials of TiO_2 at higher values in comparison with that of the K^+ free one, (originated from the change in work function when K^+ ions are adsorbed on the TiO_2 surface). This pinning leads to reducing the external bias needed for water splitting [13].
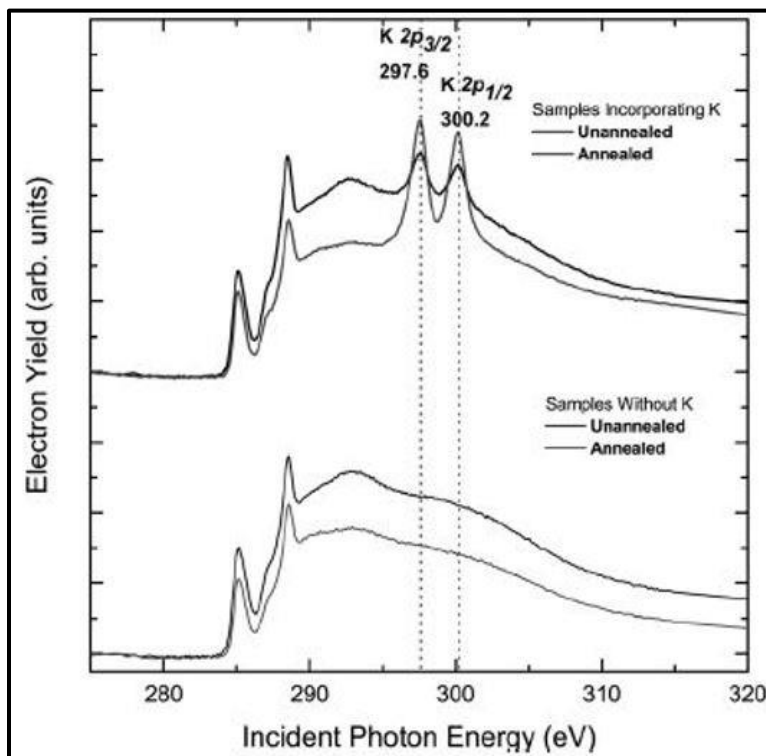
Figure 3.5: NEXAFS spectra of potassium L-edge and carbon K-edge [13]

34
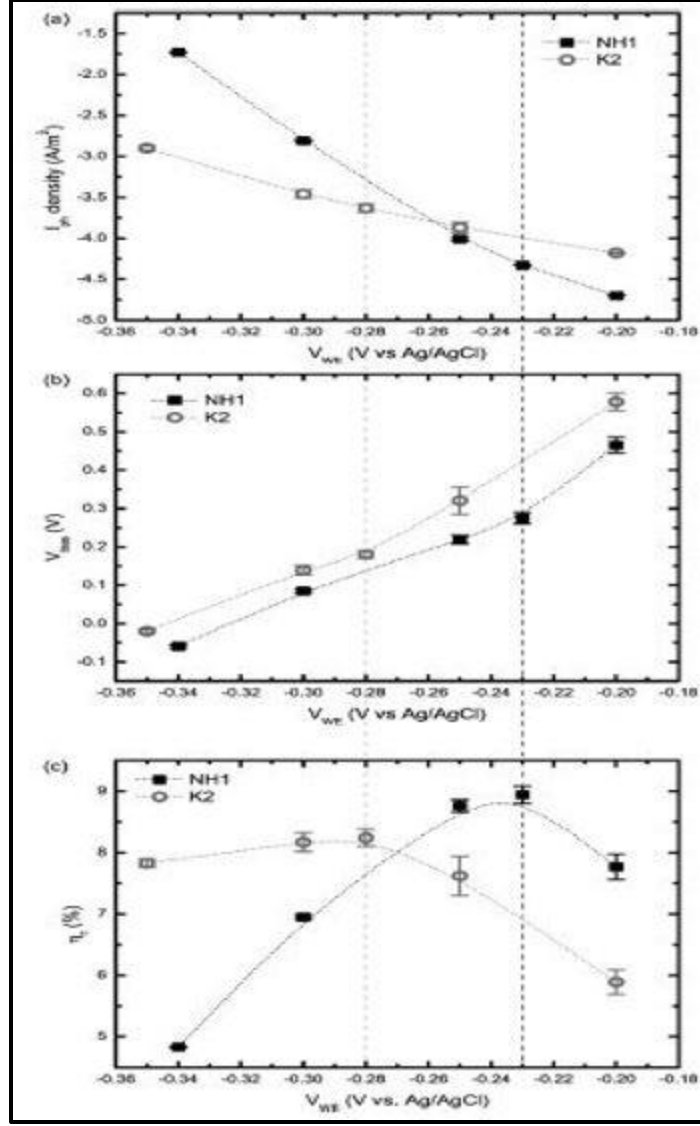
Figure 3.6: (a) Photocurrent density of NH1 and K2 samples I_{ph}, (b) Corresponding bias voltage V_{bias} and (c) Corresponding photoconversion efficiency ηc [13]

Following the same explanation used for reducing the work function of TiO_2 Richter et al. elucidated the impact of Na^+ on the photoelectrochemical performance of TiO_2 nanotubes. The authors suggested that the charge transfer between the adsorbed Na ions and TiO_2 nanotubes may have a considerable effect not only on the TiO_2 surface charge but also on the energy band properties (band bending). It was further illustrated that Na forms strong ionic bond with TiO_2 leading to effective charge transfer and modify the surface electronic and band structure inducing pinning of TiO_2 energy bands at more positive energy levels. An understanding of TiO_2 band structure that confirm these claims is displayed in Figure 3.7. Figure 3.7a represents the regular band energy diagram of TiO_2 involved in aqueous electrolyte whereas Figures 3.7b and c display the alteration of the band structure upon Na^+ adsorption. These can be summarized as (i) pinning of the energy bands of Na^+ adsorbed TiO_2 nanotubes at slightly more positive energy levels with respect to the Na^+ free TiO_2 nanotubes and (ii) less steepness of the band bending as Na is adsorbed on TiO_2 surface. The photoelctrochemical performance was also quantified showing

35

that the open circuit voltage of all Na^+ adsorbed samples are typically more negative than the Na^+ free samples as described in Figure 3.8 [14].
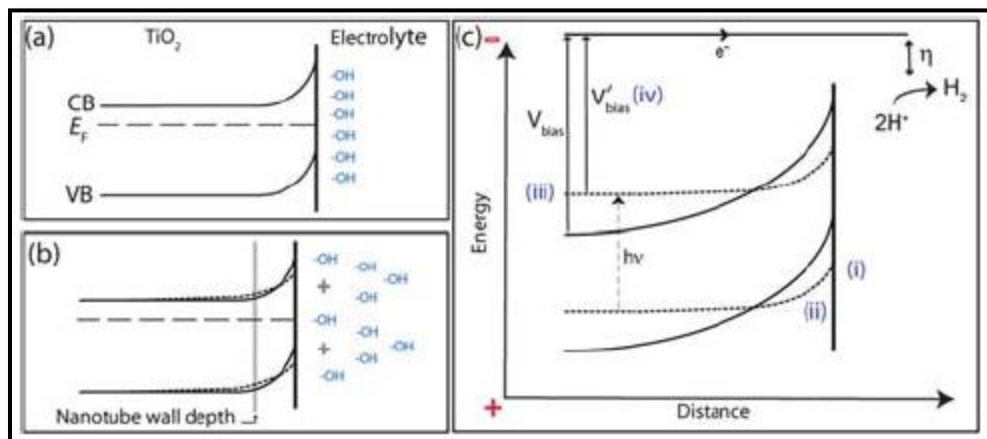
Figure 3.7: Schematic diagram for the band model demonstrating the following features (i) Positive band pinning upon Na adsorption, (ii) Less steepness of the band bending towards the surface (iii) Illuminated electrode potential is more negative and (iv) Less external bias required [14].
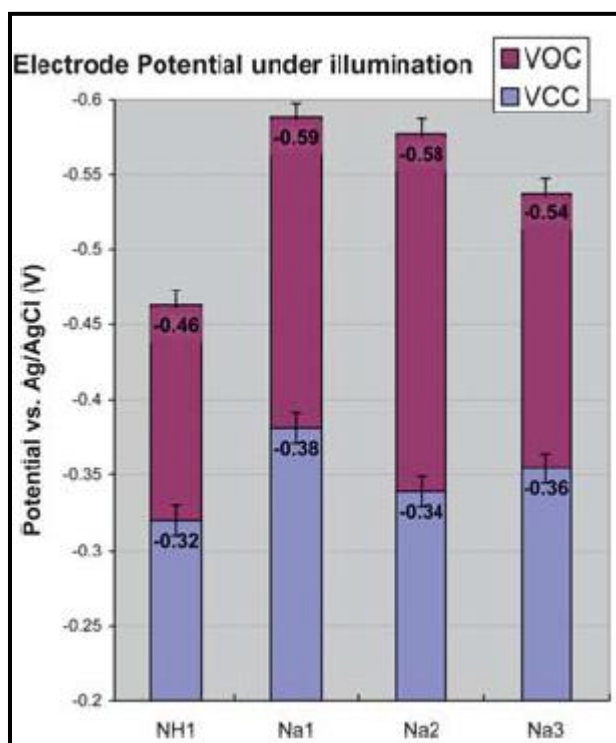
Figure 3.8: The average open circuit (VOC) and short circuit (VCC) of TiO_2 nanotube arrays measured versus Ag/AgCl [14].

In this context, an important conclusion can be drawn from these studies that considerable alteration in the surface charge will typically affect the surface electrochemistry which in return would influence the charge separation kinetics.

The role of Na in PEC water splitting applications was further investigated by Inoue et al. who utilized sodium hexatitanate $Na_2Ti_6O_{13}$ with tunnel-type structures as a photoelectrode for the cleavage of water to obtain H_2 and O_2 at apparently stoichiometric proportionality. The authors revealed that the titanates in this arrangement are assembled in a sheet described by edge- and corner-shared TiO_6 octahedra as shown in Figure 3.9a. This structure is capable of sheltering any catalytic active species such as noble atoms which in return will enhance the separation of photogenerated charges and their transfer to the adsorbed reactants on the surface. Figure 3.9b. shows the SEM image of $Na_2Ti_6O_{13}$ oxide where it maintains a layer-like structure extending to the topmost surface. It was shown that upon the involvement of $Na_2Ti_6O_{13}$ with noble metal solution ($RuCl_3$), the amount of Na ions exchange with Ru is equivalent to at least nine layers of the oxide which illustrates that Ru species were intercalated deep inside the oxide and not only on its surface. Figure 3.9c. shows that $Na_2Ti_6O_{13}$ allows stoichiometric generation of both H_2 and O_2 which indicates the membrane effect of the titanate and its ability to not only separate charges but also separate the reaction outputs, H_2 and O_2 [15]. It is worth noting that the reported behavior showed an enhancement for Na-doped TiO_2 photocatalysts over the behavior of pure TiO_2 reported by Sakata et al. who revealed the creation of a large amount of recombination centers upon the deposition of Ru over pure TiO_2 and hence a reduction in the photocatalytic activity [16].
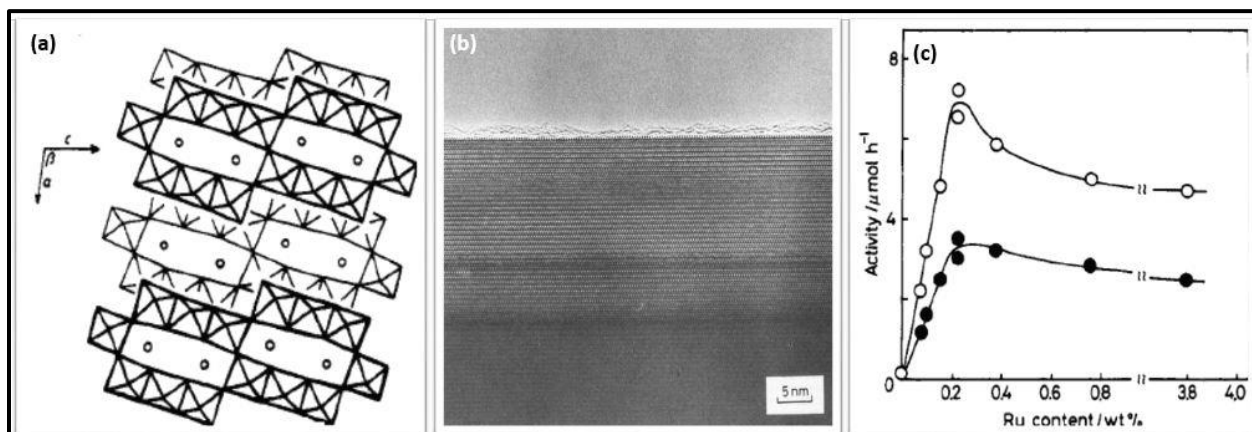
Figure 3.9: (a) Tunnel structure of $Na_2Ti_6O_{13}$ oxide, (b) High resolution SEM Image of $Na_2Ti_6O_{13}$ and (c) Photocatalytic activity of $Na_2Ti_6O_{13}$ loaded with Ru for the decomposition of water as a function with the Ru content [15].

The photocatalytic activity for the splitting of water using the hexatitanate structure of $Na_2Ti_6O_{13}$ was further reviewed by Ogura et al. who defined a valuable relationship between the ability to generate electron-hole pairs and the photoelectrochemical performance. The authors utilized electron spin resonance (ESR) spectroscopy to measure the surface radicals (active species) created upon irradiation and relate the results with the photocatalytic performance. Figure 3.10a displays the ESR spectra of $Na_2Ti_6O_{13}$ measured at 77 K under UV illumination in the existence of O_2 at 4.0 kPa. No signal were indicated under dark conditions, however, upon illumination $Na_2Ti_6O_{13}$ produced strong peaks with g=2.020, g=2.018 and g=2.004. These are attributed to the surface O^- radicals produced from lattice oxygens (O^{2-}) which clearly illustrate the high capability of $Na_2Ti_6O_{13}$ to produce photogenerated charges. Moreover, the efficiency of the photogenerated charge formation was related to the photocatalytic activity as illustrated in Figure 3.10b where $Na_2Ti_6O_{13}$ shows an exceptional ability to obtain stoichiometric generation of H_2 and O_2 from the decomposition of water. The authors further clarified that the location of the Ti ion within the tunnel structure of $Na_2Ti_6O_{13}$ is eccentric from the mass center of the other

oxygen atoms around it. This disorder induces a dipole moment which is crucially important for exciton's formation and hence influences the photocatalytic performance [17].
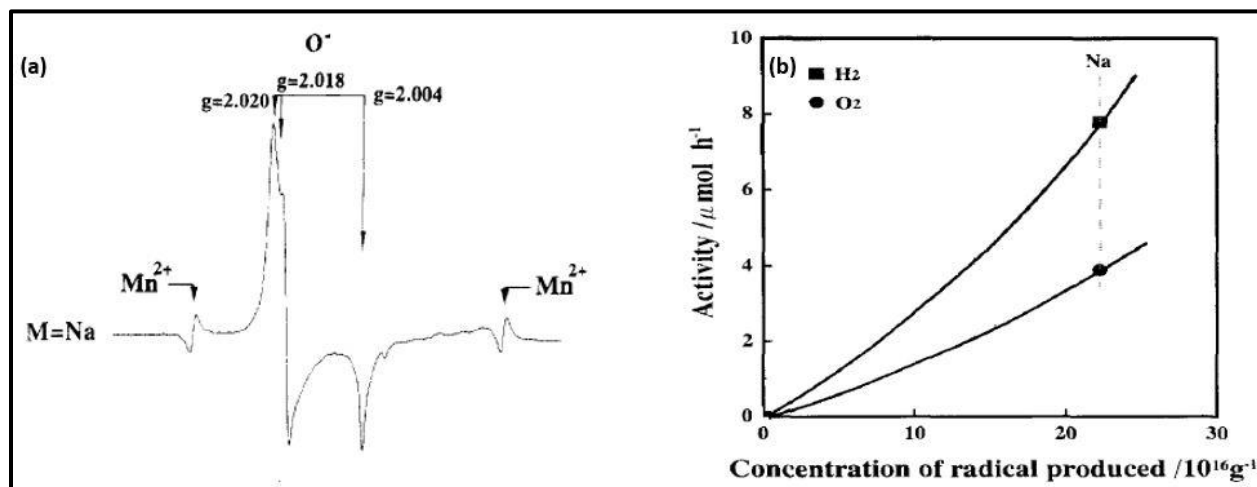
Figure 3.10: ESR spectra of $Na_2Ti_6O_{13}$ and (b) Dependence of photocatalytic activity on the concentration of the radicals produced [17].

In a latter study the same authors justified that the ability of the radical formation is related to the existence of internal fields in the disordered TiO_6 octahedra building the tunnel structure of $Na_2Ti_6O_{13}$. The authors proposed that the O^- radical can act as a hole site in the photoelectrochemical process which in turn will affect the efficiency of the photoexcieted charges separation [18]. The Raman spectrum displayed in Figure 3.11 reveals a strong single peak between 846 and 873 cm^{-1} for the $Na_2Ti_6O_{13}$ that is ascribed to the vibration of short Ti-O bond with double bond-like nature [19]. The existence of this short Ti-O bond is denotative for the distortion of TiO_6 octahedra. It was noted that the three types of the distorted TiO_6 octahedra in $Na_2Ti_6O_{13}$ creates dipole moments of 5.3, 5.8 and 6.7 Debye [20]. These significantly large dipole moments imply the presence of internal polarization fields in the TiO_6 octahedra promoting the separation of photogenerated charges and consequently enhance the O^- radical formation. This behavior is in contrast to the behavior of pure TiO_2 which does not possess dipole moments and hence is inefficient in the production O^- radical under UV illumination. Furthermore, it has been proposed that upon UV illumination, the weak Ti-O bonds are broken to produce lattice O^- radicals and Ti^{3+}. The O^- species serve as a hole center for OH^- while Ti^{3+} can trap electrons to advance the reduction of H^+ [18].
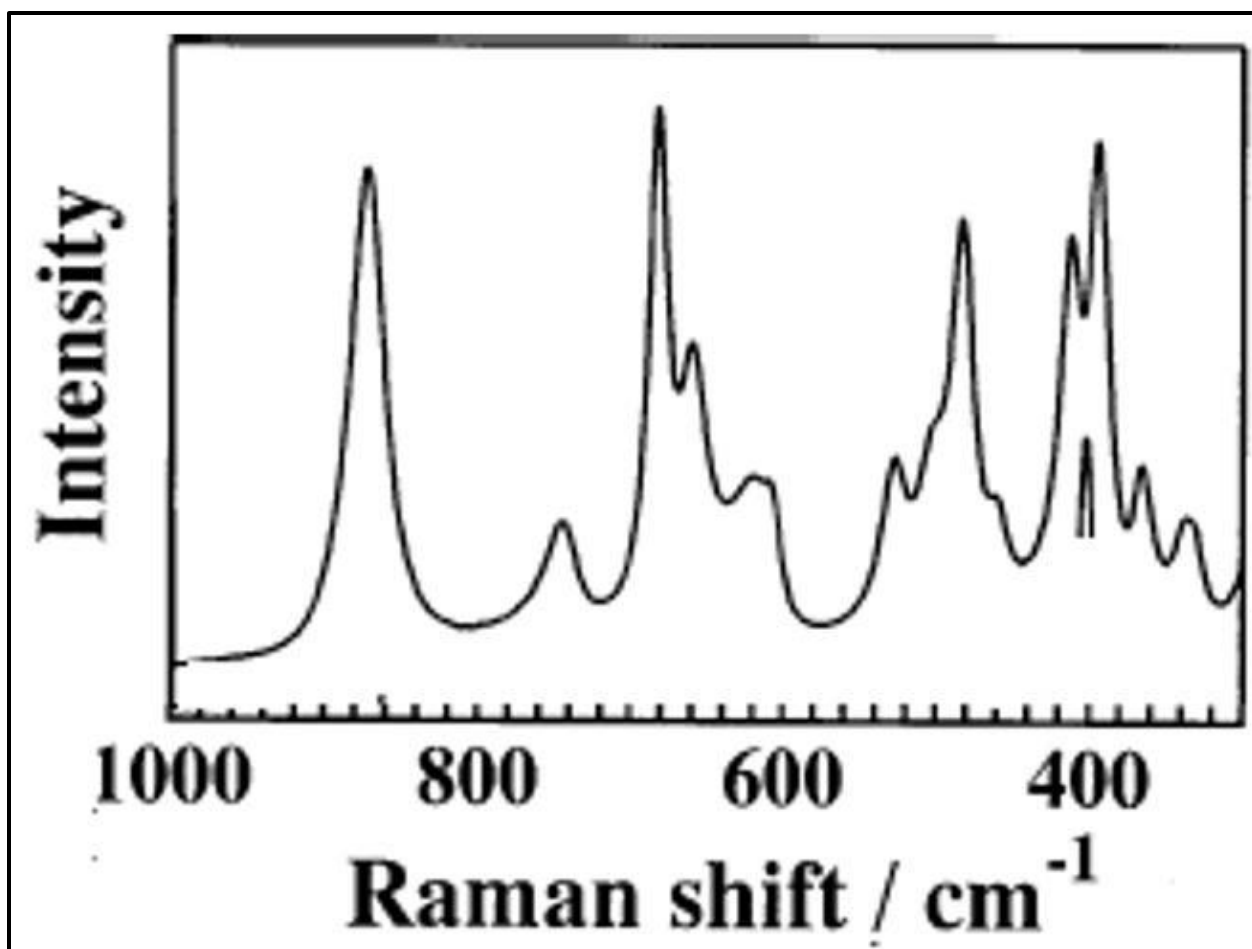
Figure 3.11: Raman spectra of $Na_2Ti_6O_{13}$ [18].

In this respect, an important conclusion can be observed from the previous studies that the high internal polarization field due to the dipole moment produced by the tunnel structure $Na_2Ti_6O_{13}$ is favorable to enhance the efficiency of the photoexcited charges separation.

Yu et al. studied the photoelectrochemical behavior of Na doped TiO_2 heterostructures prepared by H_2O_2 treatment of Ti sheets followed by immersion in Na_2NO_3 solution for 30 mins. The XRD pattern displayed in Figure 3.12a shows that Na doping process did not modify the crystal structure of TiO_2 where no new peaks for Na-Ti-oxide phases were observed. The authors attributed the phenomenon to the approximate small size of Na^+. The photoconversion efficiency of the fabricated samples was also evaluated as depicted in Figure 3.12b. It was shown that the PEC performance of the TiO_2 was directly suppressed after Na modification which was also ascribed to the smaller size of Na (1.54 Å). The behavior was further confirmed by the Mott-Schottky (MS) plots displayed in Figure 3.12c, where it was distinctly obvious from the gradient of the linear part of the curves that the Na^+ modified samples exhibited lower electron density with respect to that of pure TiO_2. The study pointed out that doping with Na steadily decreased the PEC response of TiO_2 [21].
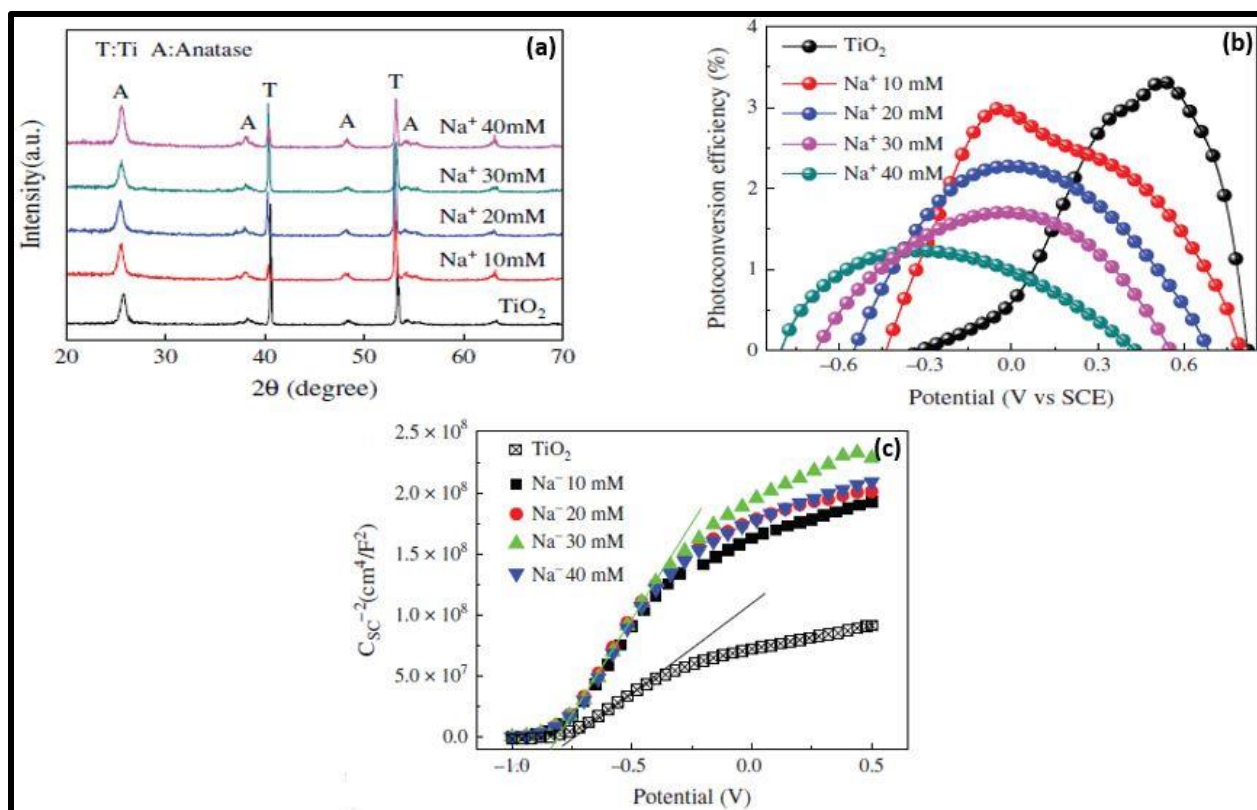
Figure 3.12: (a) XRD pattern of Na doped TiO₂ nanorods, (b) Corresponding photoconversion efficiency under Xenon lamp illumination and (c) Corresponding Mott-Schottky plots under Xenon lamp illumination [21]

The role of Na for photoelectrochemical purposes was further extended to the photolysis of gas-phase water. Yamaguti et al. studied the influence of NaOH overlaid on metallized TiO₂ (anatase) powders for gas-phase water photolysis. The authors showed that the water build-up of NaOH will maintain enough water over the catalyst to promote the photolysis of water which in turn can make NaOH act as an electrolyte that is essential for water cleavage. It was shown that the rate of hydrogen generation was very slow (0.5 µmol h⁻¹) when the catalyst is not loaded by NaOH, whereas it was greatly enhanced upon NaOH loading up to 15 wt% as illustrated in Figure 3.13. It is worth to mention that the rate of hydrogen generation starts to decrease above 15 wt% NaOH due to the fact that excess NaOH loading may prevent the release of the reaction products and consequently decrease the rate. The authors further elucidated the effect of thermal back reaction associated with the photolysis of water over metallized semiconductors according to the relation:

$$\frac{dp}{dt} = V - kP \qquad (3.1)$$

Where P is the pressure of H₂, t is the illumination period, V is the water photolysis rate when there is no back reaction and k is the rate constant of back reaction. It was reported that NaOH served to impair the thermal back reaction by increasing V and decreasing K [22].
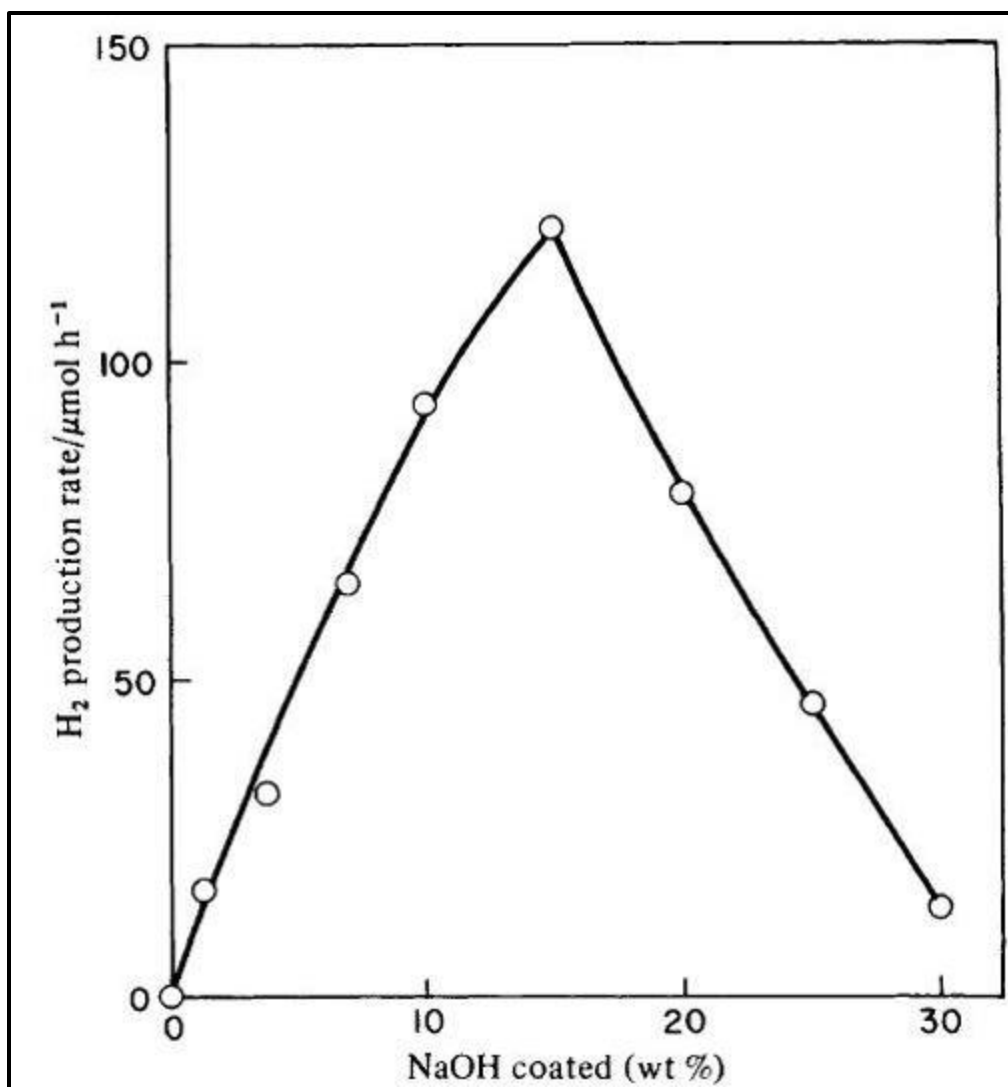
Figure 3.13: Relation between the photolysis rate and NaOH amount on metallized TiO$_2$ [22].

In addition, other reports concerning the enhanced water oxidation performance of various semiconductors modified with Na salts were recognized. Ma et al. showed that the inadequate crystallization due to thermal nitridation of Ta$_2$O$_5$ enhanced unfavorable charge carriers' recombination and thereupon reduced the quantum yield of the photoelectrochemical reaction. This can be improved by surface loading of a small amount of Na$_2$CO$_3$ onto Ta$_2$O$_5$. It was demonstrated that Na-modified Ta$_2$O$_5$ possesses superior crystallinity, smoother surface with smaller particles and more interestingly a 6-fold enhancement in the photoelectrochemical performance for O$_2$ production under visible illumination. The authors related the enhanced photoactive performance to the modified physical properties of Na-Ta$_3$N$_5$ like particle morphology, crystallinity as well as donor concentration. Figure 3.14a shows a schematic diagram for the growth of the photoactive Na$_2$CO$_3$/Ta$_3$N$_5$ catalyst and Figure 3.14b indicates the enhanced rate of O$_2$ evolution. Furthermore it was mentioned that the addition of Na$_2$CO$_3$ would not affect the semiconducting characteristics such as the energy gap and the flat band potential as long as the quantity of Na species added is kept low. This study pointed to the role of Na salts addition on the physiochemical characteristics and their relationship with the photoactive performance [23].
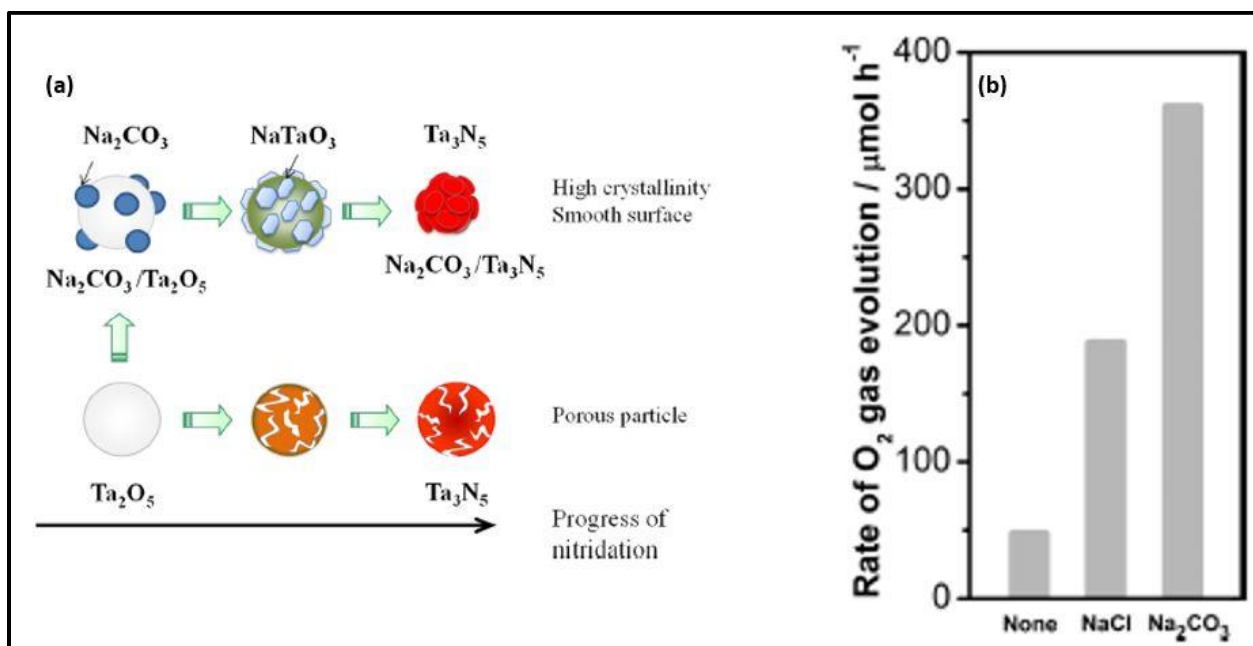
Figure 3.14: (a) Schematic diagram for the development of Na₂CO₃/Ta₃N₅ (top) and Ta₃N₅ (down) and (b) Oxygen evolution rate of Na/Ta₃N₅ [23].

Along with the previous study, Schmuki et al. highlighted the outcomes of a simple soaking treatment in Na_2SO_4 for highly organized Ta_2O_5 nanochannels annealed in NH_3 and N_2 atmospheres reporting a band gap of approximately 1.6 eV (with respect to 2.1 eV for bare Ta_3N_5) and approximately 9 fold higher IPCE spectral response. It was shown that the band gaps for the fabricated samples were estimated by plotting $(I_{ph}*h\nu)^{1/2}$ vs $h\nu$. Where I_{ph} is the photocurrent and $h\nu$ is the photon energy as displayed in Figure 3.15. The values obtained for the Na-free samples are in agreement with those reported for Ta_3N_5 (1.9-2.1eV) and TaO (2.4 eV) whereas, the Na-containing samples exhibited a considerable lower energy gap of approximately 1.6 eV. It is worth to mention that the authors clarified that these analyses do not signify an obvious confirmation either for band gap reduction or even the inclusion of extra bands into the wide band gap semiconductor. Hence, from an experimental perspective the obtained results should be treated as a "virtual" band gap [24].
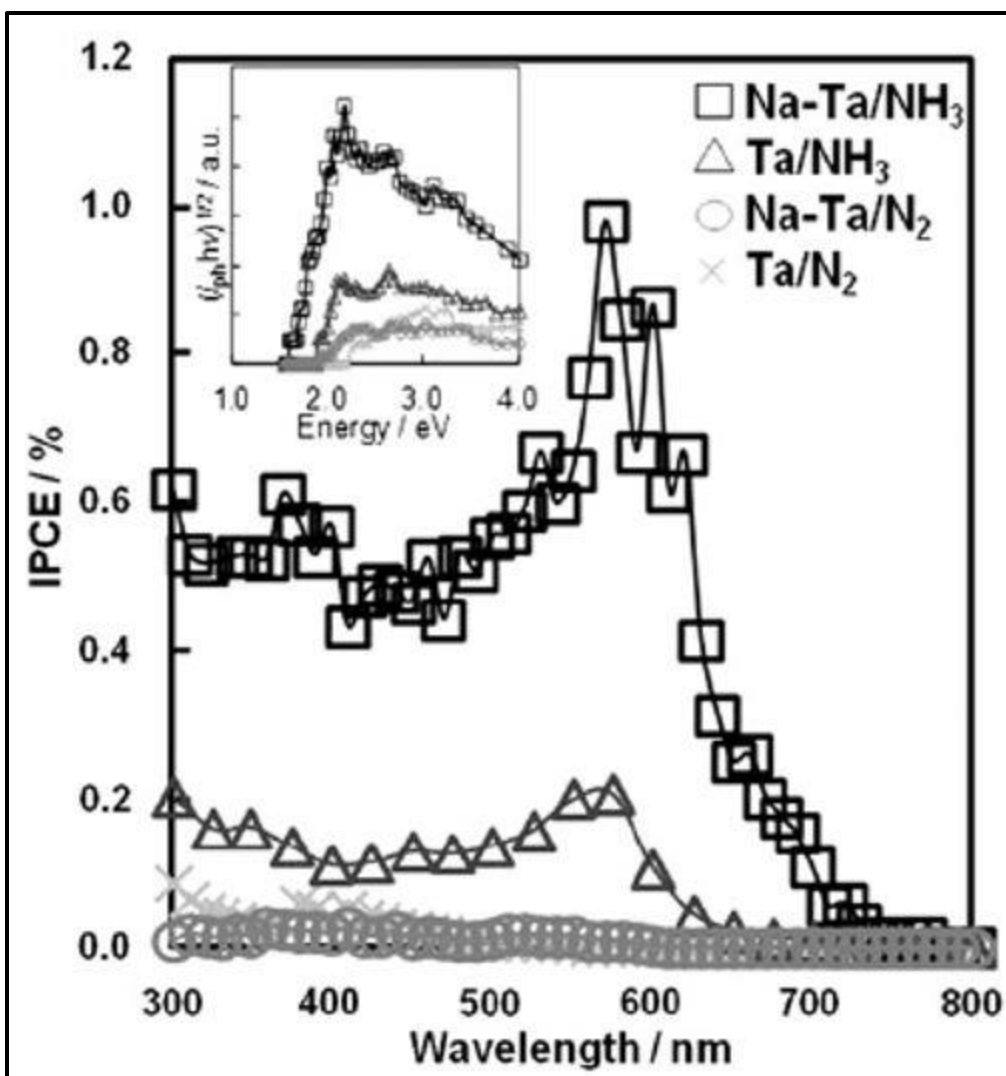
Figure 3.15: IPCE spectra taken in 0.1 M Na₂SO₄ at 0.5 V vs Ag/AgCl (3 M KCl) for samples of thickness approximately 5 μm annealed at 800 ℃ for 8 h under N₂ or NH₃ with/without pretreatment in 1 M Na₂SO₄ and the corresponding band gaps shown in the inset [24].

In the applications of large-scale energy storage systems, Xu et al. studied the performance of $Na_2Ti_3O_7$ as a Na-ion battery anode obtained by mechanical blending of anatase TiO_2 and anhydrous Na_2CO_3 with a post heat treatment at 800°C. The authors investigated the structural changes and the low-voltage characteristics by comparing $Na_XTi_3O_7$ to its $Li_XTi_3O_7$ counterpart where $(2 < X < 4)$. Also the phase transformation between $Na_2Ti_3O_7$ and the totally intercalated phase $Na_4Ti_3O_7$ was reported. Figure 3.16a shows that upon intercalation in the TiO_2 framework, the Na sites exhibited significant changes where the coordination of the Na ion is reduced from 9 and 7 in the pristine case to 6 after complete intercalation. Although, there is no Ti-O bond rupture, the lattice constants were reformed by shearing the Ti-O strip upon occupying more Na ions. On the basis of Nernst equation, the authors affiliated the battery voltage to the alteration in the Gibbs free energy within a chemical process and shows that the low voltage exhibited by $Na_2Ti_3O_7$ with respect to $Li_2Ti_3O_7$ is accompanied by minor change in Gibbs free energy. Figure 3.16b shows a high leap in the electrostatic energy of $Na_XTi_3O_7$ with respect to $Li_XTi_3O_7$. Such a leap establishes a powerful electrostatic repulsion in $Na_4Ti_3O_7$ which

43

in turn produces structural disorder and hence increases the Gibbs free energy for $Na_4Ti_3O_7$. Accordingly, the net change in the Gibbs free energy is lowered upon Na intercalation and consequently the battery voltage is reduced. Moreover, it was elucidated that due to the significant electrostatic repulsion in the totally discharged phase, $Na_4Ti_3O_7$, self-relaxation characteristics were recognized as shown by the XRD analysis. Figure 3.16c shows that the intensity of the peaks (-302) and (104) from $Na_4Ti_3O_7$ electrodes stored after full discharge decrease consistently, implying that the anode material ($Na_4Ti_3O_7$) exhibited self-relaxation which in turn will lead to self-discharge in the real fuel cell. The authors attributed the ultra-low voltage reported for $Na_4Ti_3O_7$ to be a result of a crystal structure effect rather than an electronic contribution [25].
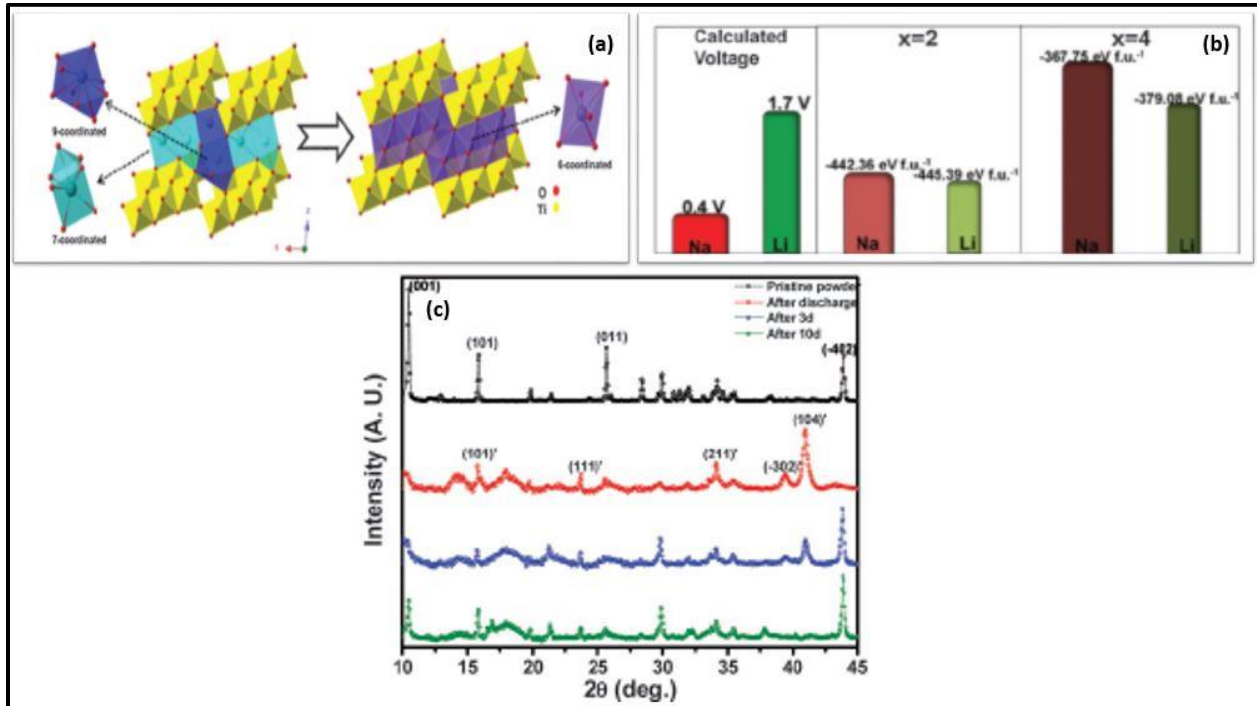
Figure 3.16: (a) The phase transformation upon Na intercalation, (b) The estimated voltage and electrostatic energy at X=2 and 4 for $Li_xTi_3O_7$ and $Na_xTi_3O_7$ respectively and (c) Change in XRD pattern with time for fully discharged electrodes [25].

With regards to applications in solar cells, Eid et al. examined the electronic influence of deposited Na on the charge carrier lifetime in Cu (In, Ga) Se_2 (CIGS) solar cells. The authors employed time resolved photoluminescence to estimate the minority carrier lifetime in polycrystalline CIGS with various thicknesses of NaF (0-30 nm) as a direct mean to detect its absorber quality. Figure 3.17a shows an increase in both positive and negative peaks of CIGS-0NaF with a time constant of 1 ps. This behavior was attributed to the eminently energetic charge carriers that have been seized by the CIGS energy states and repose expeditiously to a lower energy state. Figure 3.16b depicts the dependence of the charge carriers' recombination rate on the addition of Na where the ground state (negative band) recovery exhibited an enhancement in the recombination time from 310 ps for CIGS-0NaF to 477 ps for CIGS-15 nm NaF. Furthermore, the unrecovered negative bands that are attributed to the un-recombined charge carriers also exhibited an enhancement from 3% for CIGS-0NaF to 10% for CIGS-15 nm NaF. Moreover, it has been shown that the longer carrier lifetime (shown by the existence of a fast portion on the positive band) in CIGS-15 nm NaF maintains charge carriers in distant states

which renders favorable transfer and collection at the heterojunction and consequently improves the conversion efficiency of the device. The authors further illustrated that CIGS-15 nm NaF exhibited the longest recombination time as well as the highest concentration of charge carriers (as shown in Figure 3.17c) and reported that including more Na to CIGS may induce unfavorable defects such as acting as a quenching center and increasing the charge carriers' recombination [26].
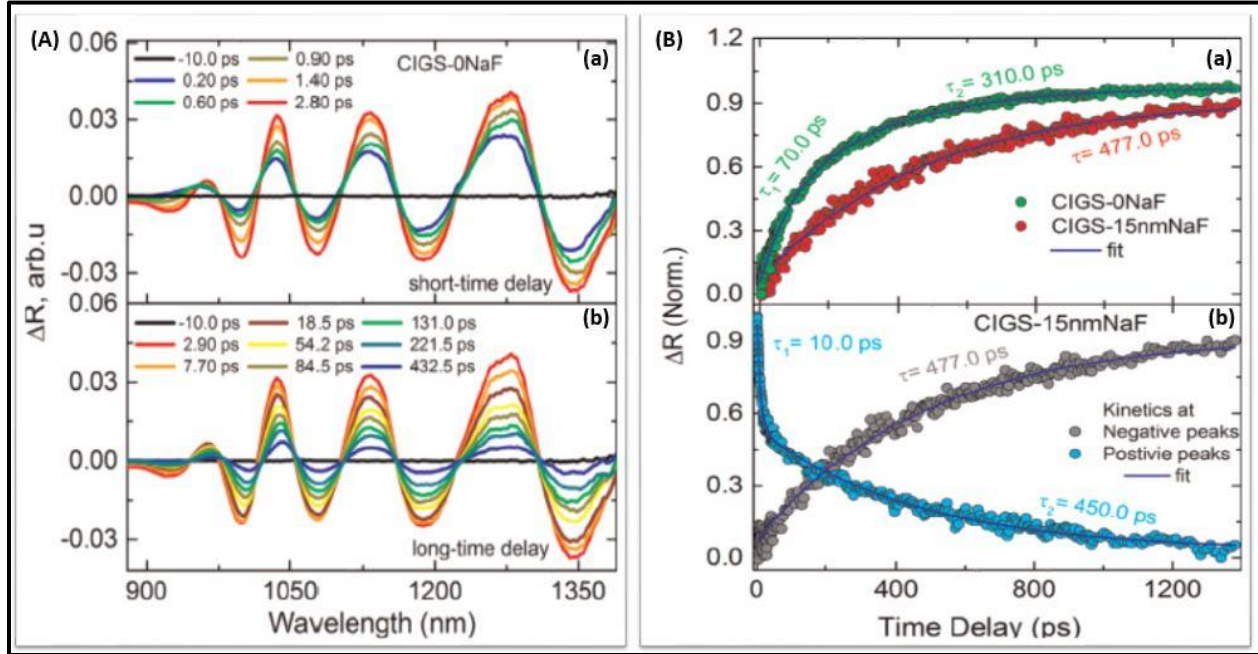
Figure 3.17: (A) Time-resolved transient reflectance spectra at (a) Early time delays and (b) Long time delays of CIGS- 0 NaF and (B) Dynamics of negative band recovery in CIGS-0NaF and CIGS-15 nm NaF (a) and Comparison of the dynamics of negative band decay and positive band recovery of CIGS-15 nm NaF (b) [26].

It is worth noting that solar cells developed with ideal Na concentrations are remarkably more efficient due to their enhanced open-circuit voltage (V_{OC}) and higher fill factor (FF) [27, 28].

From the above literature survey, it can be observed that the photoelectrochemical performance of Na-modified TiO_2 photoelectrodes is influenced by the Na doping procedures, geometries of nanostructured TiO_2, and different experimental conditions. Hence, we believe that more work should be dedicated to consider the Na content of TiO_2 photoelectrodes as a controlling parameter to improve the trade-off between the high H_2 output and the low electrical energy input needed per liter of H_2 generated.

3.2 Polymers Sensitized TiO₂ Photoanodes

As mentioned earlier, novel photocatalysts have become of significant importance due to the need for more efficient materials in solar energy applications. Inherently conductive polymers have lately regarded as novel class of electrocatalytic materials. In the year 2000 the Nobel Prize was given to Heeger, Mac-Diarmid and Shirakawa for being able to modify the typical view of polymers as dielectrics. The findings revealed that a polymer (particularly polyacetylene) can be made conductive nearly like a metal. Polyacetylene was mainly recognized as a black powder made as a silver film from acetylene. Although it has a metallic appearance, it was not a conductor until 1977. It was found that oxidation with chlorine or bromine vapor develops polyacetylene films 10^9 times more conductive than they were originally. This process was named doping similarly to the doping of semiconductors. Unfavorably, doping of polyacetyene is not applicable for experimental purposes since it is very susceptible to oxidation by air and easily affected by humidity [29]. This inspired further investigation of several conductive polymers such as poly-3-hexylthiophen (P3HT), polyaniline (PANI), polypyrrol (PPy) and poly-3,4-ethylene-dioxythiophene (PEDOT) that can be fabricated directly in more stable forms and utilized in various applications such as plastic solar cells [30,31], fuel cells [32], light emitting diodes [33], battery systems [34], and electrocatalytic materials [35, 36].

In the applications of dyes' photodegradation, Wang et al. examined the photoactive performance of TiO₂ nanoparticles altered by a small quantity of P3HT for the decomposition of methyl orange (MO) under visible illumination. The diffuse reflectance data displayed in Figure 3.18a shows a red shift in the absorption edge from 388 nm for pure TiO₂ to 414, 410, 407 and 396 nm for TiO₂/P3HT (30:1), TiO₂/P3HT (50:1), TiO₂/P3HT (75:1) and TiO₂/P3HT (100:1), respectively .These results illustrate lower band gap values for the hybrid materials in comparison to that of pure TiO₂ and consequently promote more charge carriers to be generated under visible illumination. Figure 3.18b shows that the photodegradation rate of MO increases from 13.5% for pure TiO₂ (P-25) to 88.5% for TiO₂/P3HT (75:1) revealing that TiO₂/P3HT exhibited superior photoelectrochemical performance under visible illumination. It is worth mentioning that the photodegradation rate decreased after the 75:1 molar ratio due to the fact that excess P3HT may enhance the recombination rate and thus decrease the photoactive performance. Additionally, it was shown that TiO₂/P3HT nanocomposites exhibited superior photocatalytic stability as shown in Figure 3.18c which indicates that the degradation rate of MO after 10 consecutive cycles under visible illumination is still 60% that of the first cycle. The authors further explained the mechanism of charge transfer in the hybrid TiO₂/P3HT based on the obtained results as depicted in Figure 3.18d. It was shown that upon illumination, P3HT promotes electron π- π^* transition where the photogenerated electrons are transferred from π-orbital to π^*-orbital. Thereupon, the photogenerated electrons are easily swept to the CB of TiO₂ due to the synergic effect produced from the matching of d-orbital (CB) of TiO₂ and π^*-orbital of P3HT and consequently promoted to the catalyst's surface to react with oxygen and produce superoxide radicals $\cdot O_2^-$. Meanwhile, positive holes (h^+) are produced by electron transfer from the VB of TiO₂ to the π-orbital of P3HT where they can react with OH⁻ or H₂O to produce a hydroxyl radical $\cdot OH$.
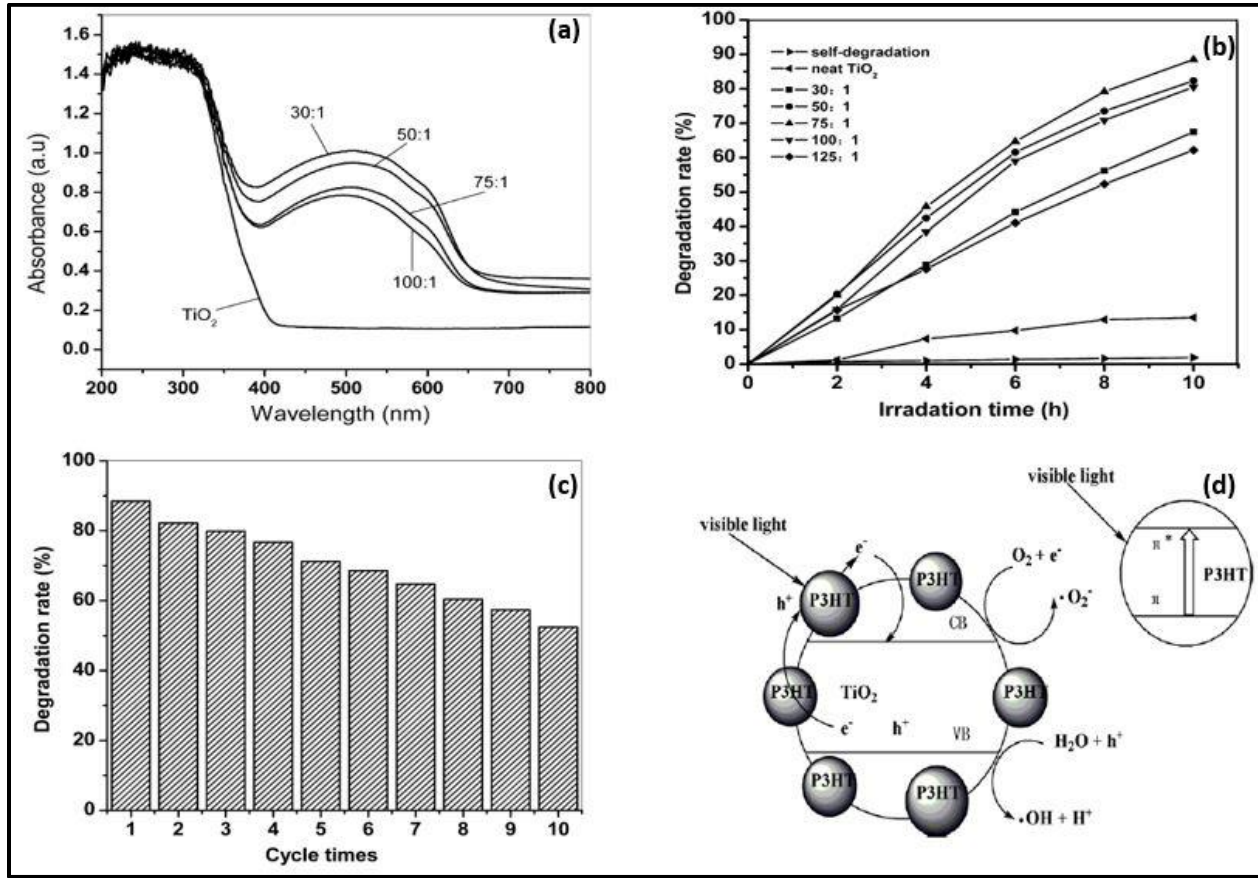
Figure 3.18: (a) Diffuse reflectance spectra for bare TiO₂ and hybrid TiO₂-P3HT, (b) Comparison of photocatalytic decomposition of MO using pure TiO₂, hybrid TiO₂ –P3HT (30:1), (50:1), (75:1), (100:1), (125:1) as well as self-decomposition of MO under visible light, (c) Photocatalytic degradation rate of MO with hybrid TiO₂-P3HT (75:1) at various recycling times and (d) Corresponding charge transfer mechanism of the TiO₂/P3HT system [37]

The produced radicals are in charge of the degradation of MO according to the following reactions [37].

$$\text{Ti}O_2/\text{P3HT} + \text{h}\nu \rightarrow \text{Ti}O_2/\text{P3HT}^+ + e^-_{CB} \qquad (3.2)$$

$$\text{e}^-_{CB} + O_2 \rightarrow O^-_2 \qquad (3.3)$$

$$H_2O + O^-_2 \rightarrow OOH \cdot + OH^- \qquad (3.4)$$

$$2 \cdot OOH \rightarrow O_2 + H_2O_2 \qquad (3.5)$$

$$OH^- + h^+ \rightarrow OH \cdot \qquad (3.6)$$

$$H_2O + h^+ \rightarrow OH \cdot + H^+ \qquad (3.7)$$

$$OH \cdot + Organic\ pollutant \rightarrow CO_2 + H_2O \qquad (3.8)$$

47
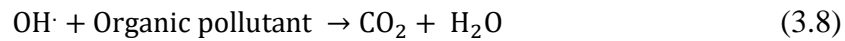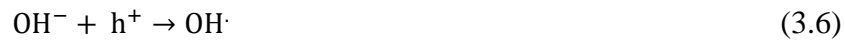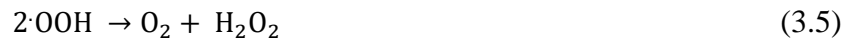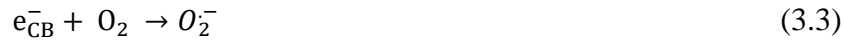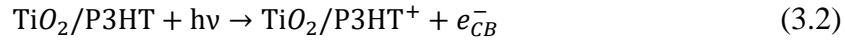
This mechanism explains that P3HT can act as a sensitizer for TiO$_2$ to narrow down the energy gap and promote the photoelectrochemical performance**.**

The role of P3HT on TiO$_2$ was further elucidated by Huang et al. who carried out photoelectrochemical measurements to analyze the photocatalytic efficiency of Dye- sensitized solar cells (DSSC) incorporating Ti$_2$O/ P3HT electrodes. With respect to the pure TiO$_2$ electrodes, the photocurrent measurements shown in Figure 3.19a indicate an enhancement of almost 2 times for the hybrid Ti$_2$O/ P3HT illustrating more favorable charge transfer due to the excitations of P3HT units. Besides, Figure 3.19b depicts the monochromatic incident-photon-to-current conversion efficiency (IPCE) of the DSSC, where the hybrid Ti$_2$O/ P3HT exhibits wider IPCE than the pure TiO$_2$ as a result of the absorption of P3HT. Furthermore, the mechanism of charge transfer at the Ti$_2$O/ P3HT interface was analyzed by electrochemical impedance spectroscopy (EIS) as displayed in Figure 3.19c, where the diameter of the semicircle of Ti$_2$O/ P3HT is less than that of pure TiO$_2$. This behavior reveals that the hybrid electrodes exhibit less charge transfer resistance (R$_{ct}$) than TiO$_2$ owing to the high conductivity of P3HT. It was confirmed that sensitizing TiO$_2$ with P3HT would extend the range of solar energy utilized from the UV to the visible. The authors also mentioned that the enhancement of the visible-driven photoelectrochemical activity reported for TiO$_2$/P3HT is relatively analogous to that reported for PANI/TiO$_2$ [38].
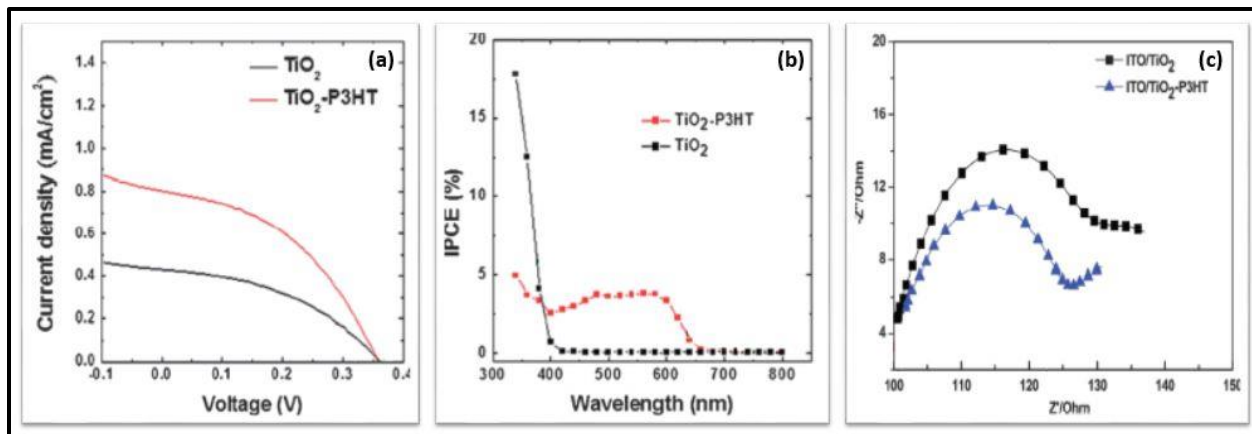
Figure 3.19: (a) J-V curve for DSSC involving pure TiO$_2$ and TiO$_2$-P3HT as photoelectrodes (b) Relevant IPCE curve and (c) Corresponding Nyquist plot for the pure TiO$_2$ and TiO$_2$-P3HT coated on ITO substrate in 5 mM Fe(CN)$_6^{3-}$/ Fe(CN)$_6^{4-}$ in phosphate buffer solution. Amplitude: 1 mV; Frequency: 0.1 Hz to 1 MHz [38]

With the same explanation of the synergetic effect, Li et al. showed that polyaniline-TiO$_2$-nanocomposite powders which were synthesized by a chemically oxidative polymerization technique in HCl solutions exhibited a substantially higher photocatalytic activity with repsect to the pure TiO$_2$ on the photodecomposition of phenol under visible irradiation. Figure 3.20a shows that PANI possesses elevated absorption in both the UV as well as the visible regions. It was also shown that the absorption of the hybrid photocatalyst increases within the visible range and decrease within the UV with respect to that of pure TiO$_2$. The band gap values estimated from the curve were 3.02 and 3.07 eV for PANI-TiO$_2$ nanocomposite and pure TiO$_2$ successively indicating that the hybrid photocatalyst can generate more charge carriers upon excitation under visible light and hence possess higher photoactivity. In the photodegradation test, several molar ratios of aniline to TiO$_2$ (from 1/60 to 1/120) were utilized as depicted in Figure 3.20b. It was shown that the self-decomposition of phenol is almost negligible revealing that phenol has no

absorption in the visible spectrum. Also, it is obvious that upon increasing the PANI content the photocatalytic degradation rate of phenol is also increasing which indicates that PANI can successfully act as a sensitizer for TiO₂. The charge transfer kinetics can be described based on the synergetic effect between TiO₂ and PANI as schematically shown In Figure 3.20c. Upon excitation, the photoexcited electrons in the LUMO level of PANI can easily migrate to the CBM of TiO₂ since they are well aligned for charge transfer. Concurrently, the positively charged holes can be created by electron migration from TiO₂ VBM to HOMO level of PANI.
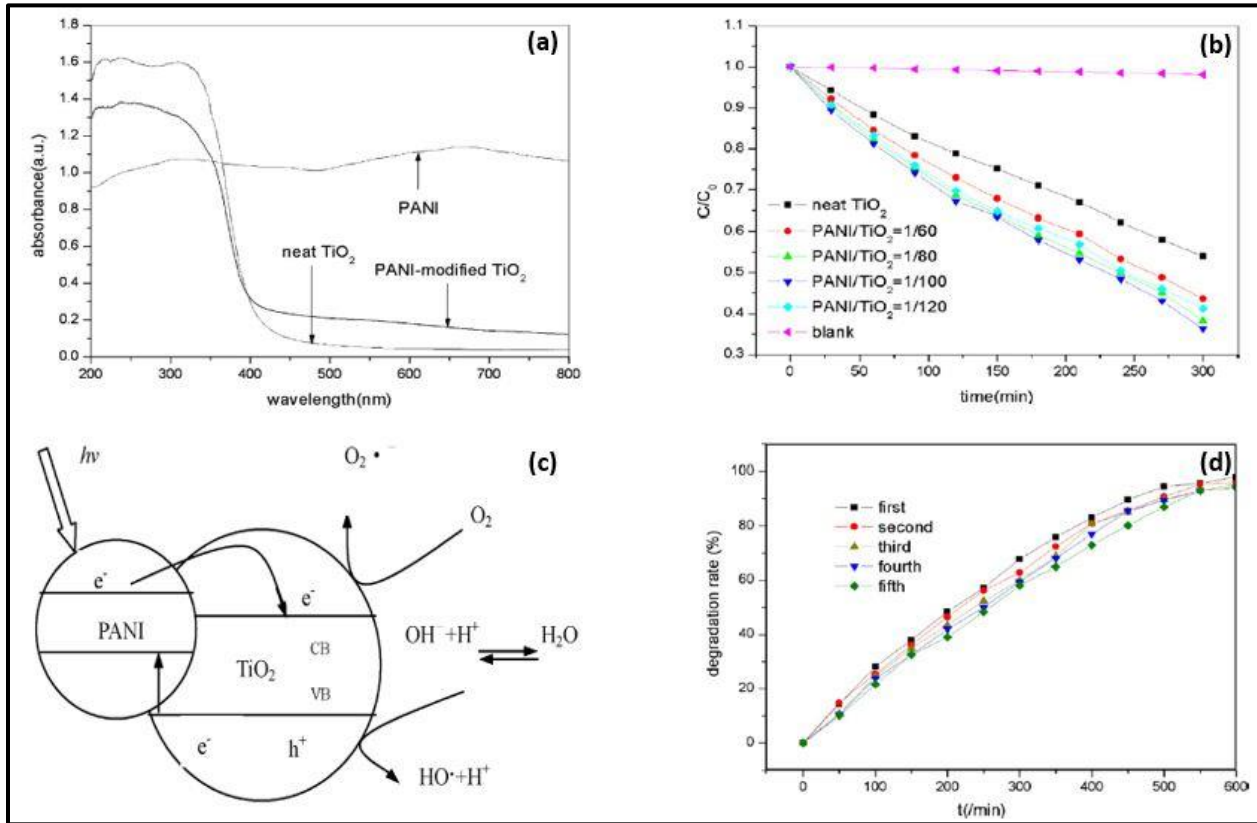
Figure 3.20: (a) Diffuse reflectance spectra for PANI, TiO₂ and PANI modified TiO₂, (b) Photocatalytic degradation of phenol in the existence of pure TiO₂, PANI/TiO₂ as well as self-degradation of phenol under visible light, (c) Proposed mechanism of the photodegradation reaction by hybrid PANI/TiO₂ and (d) photocatalytic degradation rate of phenol in the presence of PANI/TiO₂ for five cycles [39].

The carriers produced can react with water to produce hydroxyl and super-oxide radical which are accountable for the decomposition of the pollutant molecules according to the following reactions:

$$PANI/TiO_2 + \text{h}\nu \rightarrow PANI^+/TiO_2 + e^-_{CB} \qquad (3.9)$$

$$e^-_{CB} + O_2 \rightarrow O_2^{\cdot -} \qquad (3.10)$$

$$PANI^+/TiO_2 \rightarrow PANI/TiO_2 + h^+_{VB} \qquad (3.11)$$

$$h^+_{VB} + (H_2O \leftrightarrow H^+ + OH^-) \rightarrow H^+ + OH^{\cdot} \qquad (3.12)$$
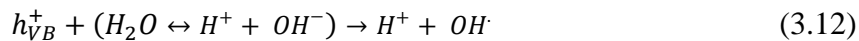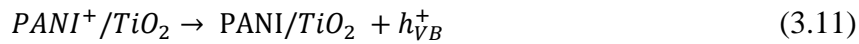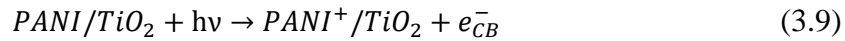
It should be also noted that TiO_2 nanoparticles deposited by polyaniline exhibited superior stability under visible illumination and retain a higher photocatalytic performance after various cycles (See Figure 3.20d) [39].

The photocatalytic activity of PANI on TiO_2 was further investigated by Lin et al. who studied the role of the radical species produced from a PANI/TiO_2 hybrid photocatalyst in the mineralization of Methyl orange (MO) and 4-chlorophenol (4-CP) under visible illumination. The active species were verified by adding several types of active species scavengers, photoluminescence spectra (PL), electron spin resonance spectra (ESR), and photoelectrochemical techniques. Due to the mechanism of charge transfer of PANI that allows the photoexcited electrons from HOMO to LUMO to be transferred to the conduction band of TiO_2 besides accepting holes from the valence band of TiO_2, the life time of the charge carriers is enhanced. Accordingly, the production of several types of radical species with immense oxidation ability like hydroxyl radicals and superoxide radicals is more favorable. The ESR spin-trapping approach depicted in Figure 3.21a reveals a strong and more apparent peak for the $O_2^{\cdot-}$ species of the PANI/TiO_2 nanocomposite treated at 200°C than that of pure TiO_2 treated at the same temperature. Besides, the PL study shown in Figures 3.21b and c reveals that the hybrid PANI/TiO_2 photocatalysts are able to produce a strong band of the hydroxyl radical $\cdot$OH than that of the bare TiO_2 as well as demonstrating that radicals developed on the surface are directly related to the light illumination period. These results indicate that the generation rate of both $O_2^{\cdot-}$ and $\cdot$OH species on the PANI/TiO_2 surface is larger than that of pristine TiO_2 and hence verify the more favorable visible-driven photoactive performance for the mineralization of MO and -4-CP. The authors further performed photoelectrochemical techniques in order to study the photocurrent behavior and the charge transfer efficiency as indicated 3.21d and e. the photocurrent spectral response reveals that upon illumination, the photocurrent of the hybrid PANI/TiO_2 reaches almost 3.2 times that of pure TiO_2 which further verifies the synergetic behavior between PANI and TiO_2. It is also vividly depicted that the radius of the curvature of the Nyquist plot for PANI/TiO_2 is much shorter than that of pure TiO_2 illustrating more favorable interfacial charge transfer as well as lower charge carriers' recombination rate [40].
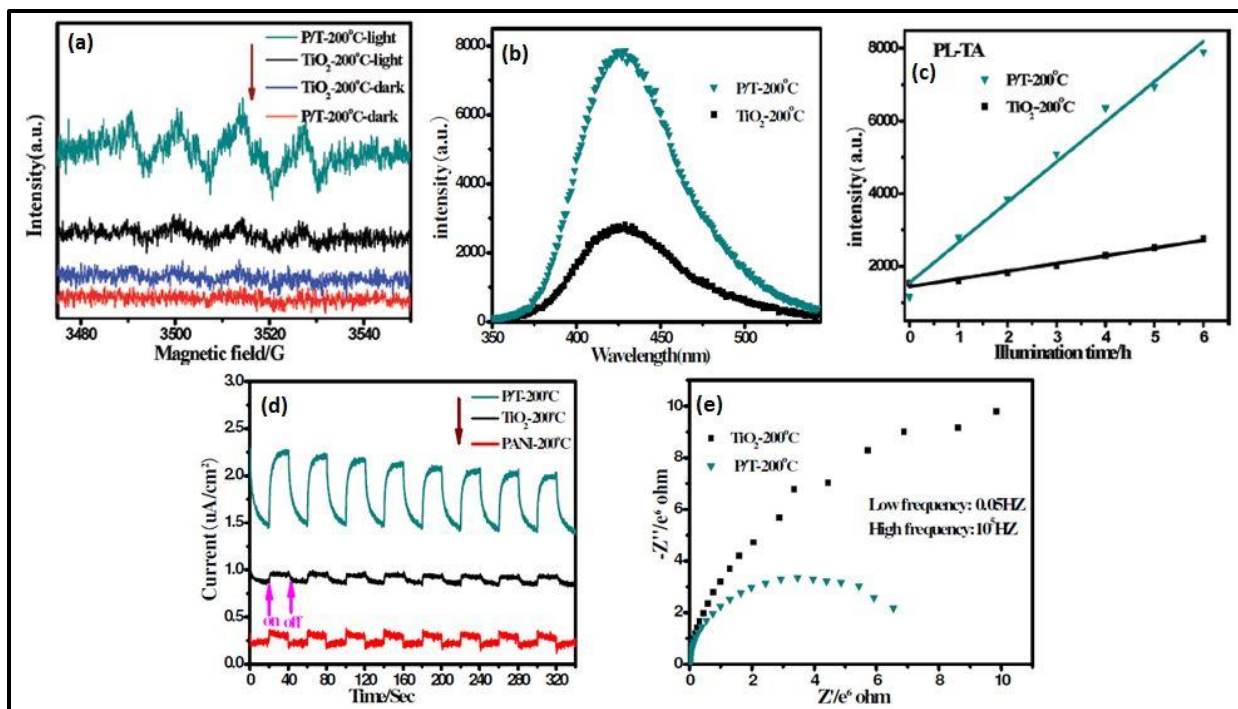
Figure 3.21: (a) Spin-trapping ESR spectra of pure TiO$_2$ and PANI/ TiO$_2$ at 200 °C under dark and illuminated conditions, (b) ·OH-trapping photoluminescence spectra of pure TiO$_2$ and PANI/ TiO$_2$ at 200 °C under visible light for 6 h, (c) Comparison plot of temporal changes in ·OH-trapping photoluminescence spectra of pure TiO$_2$ and PANI/TiO$_2$ at 200 °C under visible light for 6 h, (d) Photocurrent spectral response for pure PANI, pure TiO$_2$ and hybrid PANI/TiO$_2$ at 200 °C under visible light and (e) EIS Nyquist plot for pure TiO$_2$ and hybrid PANI/TiO$_2$ at 200 °C with an applied voltage of 1.0 V under visible irradiation [40].

In the same application of the dyes' photodegradation the role of TiO$_2$/PPy hybrid photoelectrodes has also been investigated. Li et al. examined the photoactive performance of macroporous (PPy)-TiO$_2$ hybrid photoelectrodes developed by oxidative polymerization of Pyrrole in TiO$_2$ for the decomposition of Methyl blue (MB) under solar simulated light. Table 3.2 reveals that all the hybrid materials exhibit superior photoactive performance with reference to the pristine TiO$_2$. This illustrates the presence of a very well strengthened interface and a profound synergetic effect between PPy and TiO$_2$ which is favorable for more enhanced charge carriers' separation and rapid charge transfer at the PPy/TiO$_2$ junction. Upon increasing the molar ratio of PPy:TiO$_2$ from 0.05:1 to 0.4:1, the photoactive performance was enhanced at first and then diminished. The behavior indicates that excess PPy can pile up over the TiO$_2$ surface increasing the diffusion barrier as well as the recombination rate and hence leading to a detrimental effect on the photoactivity. The authors also claimed that increasing the amount of PPy beyond the optimized limit could hinder the entry of the photon energy inside the hybrid material and also negatively affect the photoactive performance. The concept was further made clear by illustrating the mechanism of charge transfer in the PPy-TiO$_2$ nanocomposites as shown schematically in Figure 3.22. Upon illumination, the electrons are agitated from the HOMO to the LUMO level of PPy and then transferred to the conduction band of TiO$_2$ to react with water or oxygen molecules to form O$_2^-$ and ·OH radicals which are the active species responsible for the decomposition of the pollutant. This proves that PPy can act as a photosensitizer in the hybrid material to enhance the charge separation capabilities. The study reveals that the nanoscale combination between the two constituents can produce a hybrid material with a

balanced organic-inorganic interface, synergy impact and an improved photocatalytic activity that is not achievable by their individual analogues [41].

Table 3.3: The rate constant of the photodegradation reaction of MB as a function of PPy content [41]

Samples	PPy (wt.%)	k (min^{-1})
Macroporous TiO$_2$	0.00	0.0223
PPy/TiO$_2$ (0.05:1)	3.93	0.0322
PPy/TiO$_2$ (0.1:1)	7.76	0.0342
PPy/TiO$_2$ (0.2:1)	15.33	0.0271
PPy/TiO$_2$ (0.4:1)	21.04	0.0253
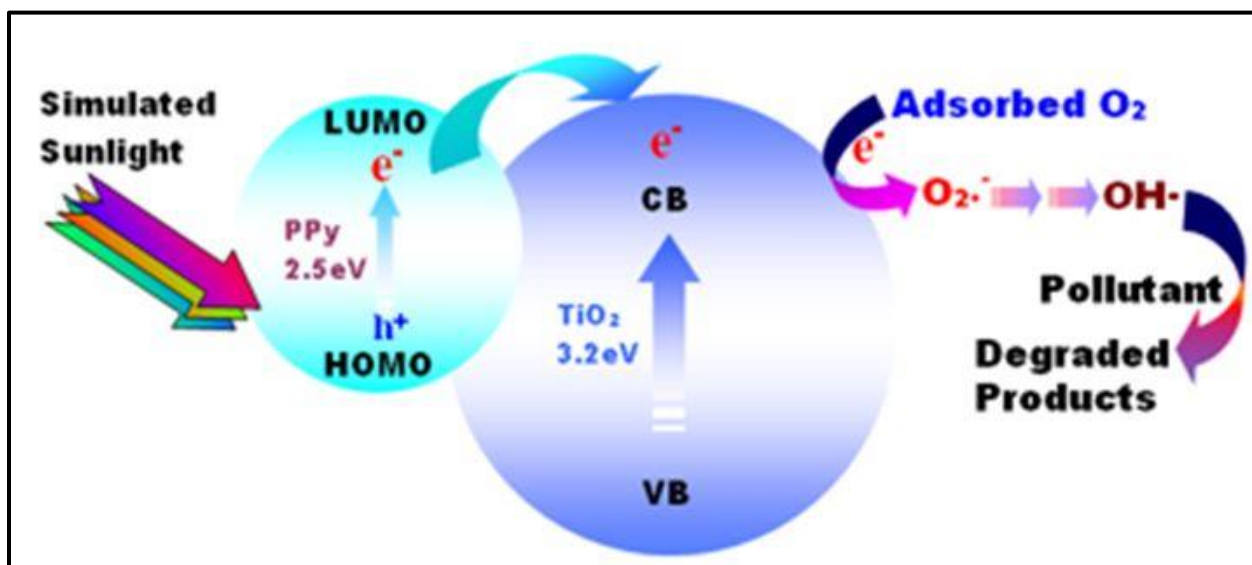
Figure 3.22: Schematic representation for the mechanism of charge transfer over hybrid PPy/TiO$_2$ [41].

The effect of PPy on TiO$_2$ was further discussed by Li et al. who performed an optical and photoelectrochemical measurements to realize the photoresponse of the mixed organic/inorganic system. The authors fabricated PPy-TiO$_2$ heterojunctions via polymerization of PPy within macro/mesoporous TiO$_2$ under UV light at various irradiation times (12, 24, 36, 48 h) for the degradation of Rhodamine B (RhB) under visible irradiation. Figure 3.23A illustrates the optical response of the fabricated samples, indicating that the photoactivity of all hybrid materials is shifted to the visible range (2.67-2.92 eV) exhibiting a band gap narrowing with respect to 3.18 eV of the pure TiO$_2$. These outcomes reveal that the hybrid materials could have a considerable activity under visible light illumination. The transient photocurrent spectrum shown in Figure 3.23B indicates that the photocurrent spectral response of bare TiO$_2$ was improved after introducing PPy into the TiO$_2$ framework. The photocurrent density reached a maximum of 2.7 µA/cm^2 for the PPy-TiO$_2$-24 which is 2.5 times higher than the 1.1 µA/cm^2 reported for pure TiO$_2$. It should be particularly noted that upon increasing the PPy content, the photocurrent response increases at the beginning and then decreased. The authors justified the

phenomenon with the fact that additional PPy may produce a non-uniform sensitizer layer and hence, enhances the excitons' recombination rate. Moreover, the behavior was further confirmed by the electrochemical impedance spectra depicted in Figure 3.23C, showing that the composites attained after 12 and 24 h of illumination exhibited a higher transfer rate of the excitons with respect to that of the bare TiO$_2$ in agreement with photocurrent spectral response. The study confirms that the PPy can be an effective sensitizer for TiO$_2$ and enhance the photocurrent efficiency [42].
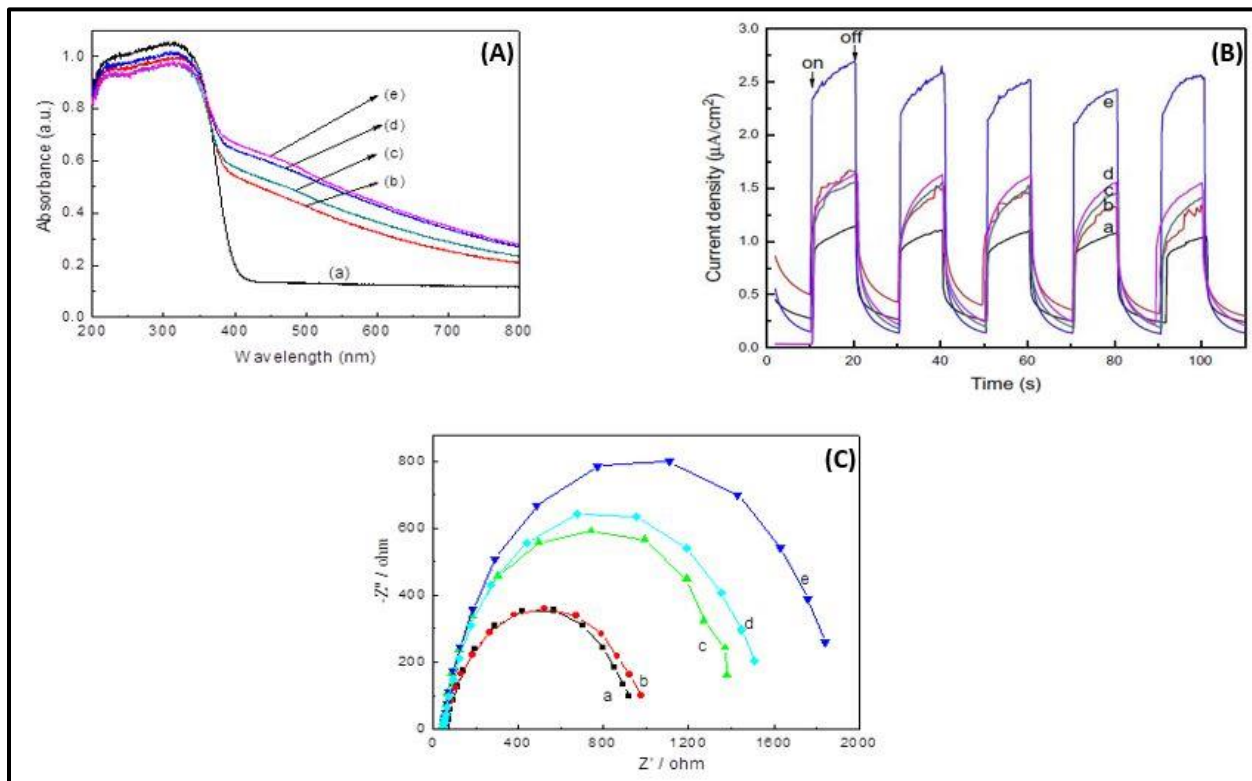
Figure 3.23: (A) Diffuse reflectance spectra of (a) pure TiO$_2$, (b) TiO$_2$-PPy-12, (c) TiO$_2$-PPy-24, (d) TiO$_2$-PPy-36 and (e) TiO$_2$-PPy-48. (B) Amperometric analysis for (a) pure TiO$_2$, (b) TiO$_2$-PPy-12, (c) TiO$_2$-PPy-36, (d) TiO$_2$-PPy-48, (e) TiO$_2$-PPy-24 at 0 V under visible illumination and (C) EIS Nyquist plot of (a) TiO$_2$ -PPy-24, (b) TiO$_2$-PPy-12, (c) pure TiO$_2$, (d) TiO$_2$-PPy-36 and (e) TiO$_2$-PPy-48 [42].

With regards to applications in water splitting, Luo et al. studied the performance of polypyrrole-TiO$_2$ nanotube array hybrids (PPy-TNTs) fabricated by an electrochemical anodization followed by a potentiostatic polymerization technique where the incorporated PPy is altered by varying the electro-polymerization time (1 min, 5 min and 10 min). The UV-vis spectra depicted in Figure 3.24a reveal that all heterojunctions exhibited higher absorption intensity than that of the pristine TiO$_2$ which illustrates that PPy can act as a photosensitizer for collecting a larger number of visible light photons. Besides, the hybrid electrodes electropolymerized at 5 (PPy5-TNTs) and 10 mins (PPy10-TNTs) possess a higher absorption intensity with respect to that of the sample electropolymerized at 1 min (PPy1-TNTs) owing to the extended polymerization period that yields a more uniform and continuous coverage of the TiO$_2$ surface. It was also noted that the visible light absorption of PPy10-TNTs is lower than that of PPy5-TNTs which is ascribed to the excess coverage of PPy that may hinder the absorption of the photons by the nanotubes and produce light reflection. The photocurrent transient spectra displayed in Figure 3.24b shows that all the fabricated electrodes possess reproducible

photocurrent begavior during the continual on/off illumination cycles. The transient response of PPy5-TiO$_2$ is approximately 3.48 mA/cm^2, a value that is almost 2.4 times greater than that of the bare TiO$_2$ (1.45 mA/cm^2). Additionally, it is vividly apparent that the PPy5-TNTs exhibited the optimum photoresponse with respect to PPy1-TNTs (2.05 mA/cm^2) and PPy10-TNTs (2.56 mA/cm^2) due to the fact that it possesses a more favorable content of PPy than PPy1-TNTs and a smaller diffusion barrier for the photogenerated charges, in comparison to that of PPy10-TNTs. Moreover, the photostability of PPy5-TNTs was studied by amperometric I-t analysis under a simulated irradiation (AM 1.5, 1000 mW/cm^2) for a period of 3500 s. Results illustrates a higher photostability and a superior photocorrosion resistance at all the times in comparison with the pure TiO$_2$ which exhibited an apparent decay at the end of the measurements (see Figure 3.24c). Accordingly, the linear sweep voltammetry (LSV) for the fabricated samples was investigated as displayed in Figure 3.24d. The behavior shows a less dark current attained by the pristine TiO$_2$ nanotubes than its photocurrent which indicates that the photocurrent generated is mainly responsible for the photoelectrochemical process. Upon illumination, the photocurrent densities increases progressively at a lower potential range (-0.8 to 0 V vs Ag/AgCl) owing to the carriers' separation by the effect of the electric field and then saturation is maintained by all the samples at higher potential ranges (0 to 0.6 V vs Ag/AgCl). It is also noticed that the open circuit potentials of all the hybrid materials are negatively shifted in comparison with that of the bare TiO$_2$ elucidating that the hybrids possess less band bending requirements and improved charge transport capabilities. Furthermore, the electrochemical impedance spectroscopy (EIS) was utilized to evaluate the charge transfer process within the samples as shown by the Nyquist plot depicted in Figure 3.24e. It was shown that the radius of the curvature on the EIS plots for all the hybrid materials is smaller than that of the bare TiO$_2$ which demonstrates that the hybrid possesses a smaller charge transfer resistance as well as an enhanced charge separation and mobility. Subsequently, Mott-Schottky (MS) plots were obtained under dark to detect the flat band potential (E$_{FB}$) as well as the carriers' density (N$_D$) of the fabricated electrodes according to the relation described hereinafter: [43].

$$\frac{1}{C^2} = \frac{2}{N_D \, e \, \varepsilon_0 \varepsilon} (E - E_{FB} - \frac{kT}{e}) \qquad\qquad (3.13)$$

Where C is the space charge capacitance in the semiconductor, N$_D$ is the electron carriers' density, e is the elemental charge, ε_0 is the permittivity of vacuum, ε is the relative permittivity of the semiconductor, E is the applied voltage, E$_{FB}$ is the flat band potential, T is the temperature and k is the Boltzmann constant.

Figure 3.24f illustrates the Mott-Schottky plots of 1/C^2 as a function of the applied voltage where it is obviously clear the positive slopes of the linear parts of the curves indicate an n-type semiconducting behavior for all the fabricated samples. This could be attributed to the smaller quantity of the p-type PPy that covers the surface of the major bulk n-type TiO$_2$. Additionally, the curves were extrapolated to 1/C^2 = 0 in order to calculate the values of E$_{FB}$ for the pure TiO$_2$ as well as the hybrid materials, the values obtained are approximately -0.5 and -0.75 V vs Ag/AgCl correspondingly. This demonstrates a negative shift in the E$_{FB}$ of the hybrids with respect to the bare TiO$_2$ which indicates a decrease in the band bending edge and hence an improved separation and transfer for the photoexcited electrons. Furthermore, the carriers' density was also estimated according to the relation described below:

$$N_D = \frac{2}{e\varepsilon_0\varepsilon}\left(\frac{dE}{d\left(\frac{1}{C^2}\right)}\right) \tag{3.14}$$

Where e=1.6 x 10^{-19} C, ε_0= 8.86 x 10^{-12} F/m and ε=48 for anatase TiO_2

The values obtained for TiO_2, PPy1-TNTs, PPy5-TNTs and PPy10-TNTs are nearly 1.47 x 10^{18}, 2.45 x 10^{18}, 7.35 x 10^{18} and 3.68 x 10^{18} respectively which illustrates that the donor density of all the hybrid materials are considerably larger than that of the pure TiO_2 owing to the existence of PPy that acts as an electron donor. It is worth to mention that PPy5-TiO_2 exhibits a superior conductive performance in comparison to the PPy10-TNTs due to the slower recombination rate of the photogenerated charges which maintains a greater level of electron donor density.
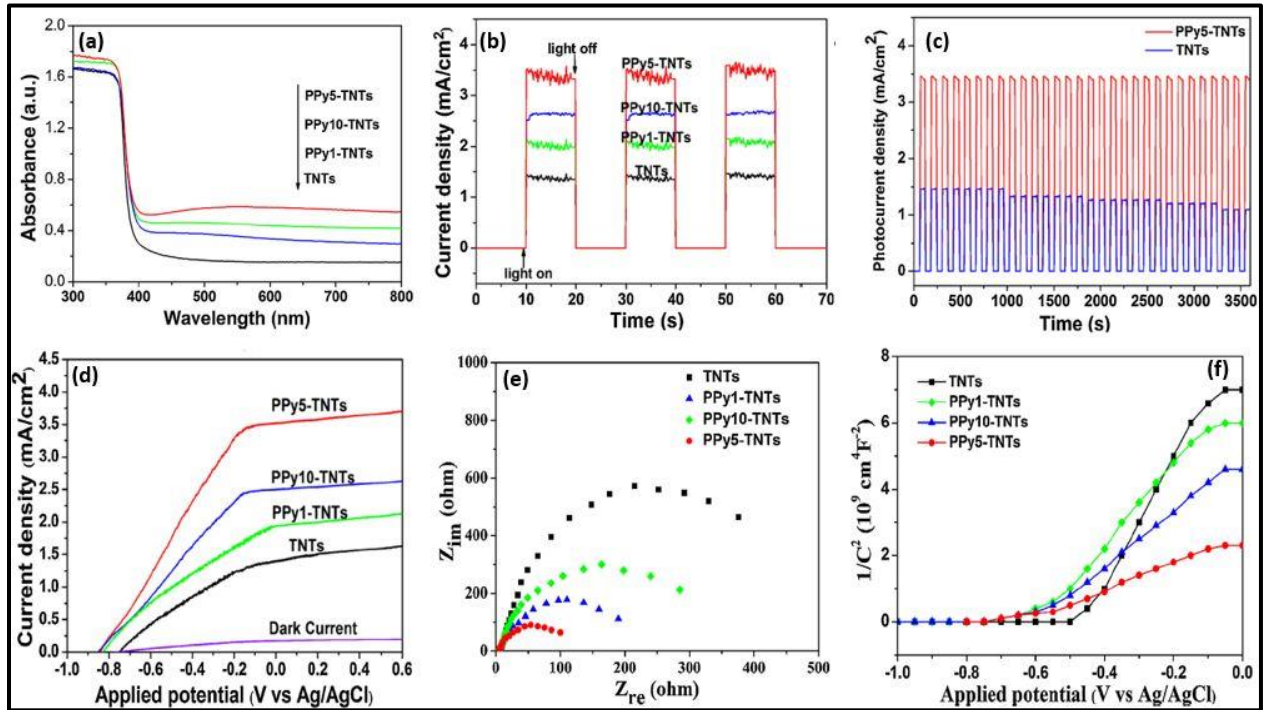
Figure 3.24: (a) Diffuse reflectance spectra for pure TiO₂ as well as PPy1-TNTs, PPy5-TNTs and PPy10-TNTs, (b) Corresponding amperometric behavior at an applied voltage of 0.23 V (vs. Ag/AgCl), (c) Photocurrent density response stability for pure TiO₂ and PPy5-TNTs, (d) Linear-sweep voltammetry for for pure TiO₂ as well as PPy1-TNTs, PPy5-TNTs and PPy10-TNTs with scanning rate of 5 mV/s, (e) Corresponding EIS Nyqusit plot at open circuit voltage under illumination and (f) Corresponding Mott-Schottky plots at a frequency of 5 Hz under dark [43].

The kinetics of the water splitting process for the PPy-TiO_2 hybrids was schematically described in Figure 3.25. In consistency with the literature, the energy gap of anatase TiO_2 is 3.2 eV and that of PPy is 2.2 eV. When the Fermi level of both TiO_2 and PPy achieves equilibrium after contact, an electric field is produced, where the p-type (PPy) zone collects the negative charge while the n-type (TiO_2) collects the positive charge. Upon illumination, the electrons are excited from the HOMO of the PPy to its LUMO then rapidly migrate to the CB of TiO_2 since it is at lower potential level than the LUMO of PPy. Concurrently, there are some electrons that are excited from the VB of TiO_2 to its CB owing to the small portion of UV light absorbed. The existence of the internal field in the p-n junction can improve the separation of the photoexcited charges, that is the agitated electrons can migrate to the Pt electrode to carry out the hydrogen

55

evolution reaction and concurrently, the holes transfer from the VB of TiO_2 to the HOMO of PPy can diffuse to the junction between the hybrid and the electrolyte to carry out the oxygen evolution reaction. The authors verified that the coated PPy can serve as a photosensitizer and an efficient hole transport layer for TiO_2 [43].
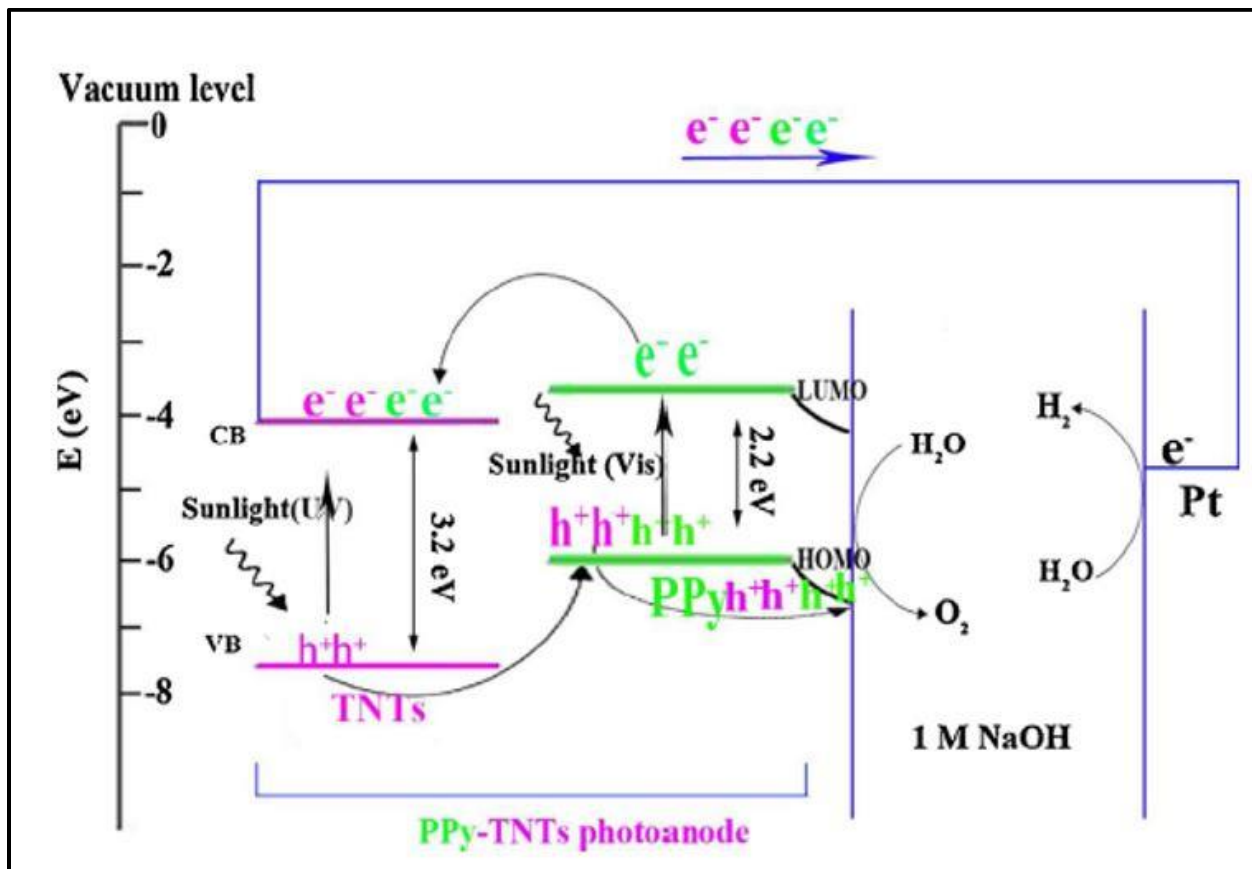
Figure 3.25: Schematic illustration for the water splitting process by PPy- TNTs [43]

Another conductive polymer that has shown promising results when combined with inorganic semiconductors in solar energy applications is PEDOT. Kowalski et al. were able to utilize the electropolymerization technique to deposit PEDOT in TiO_2 nanotubes. The method permits the fabrication of either highly ordered TiO_2-PEDOT nanocomposites or polymer nano-architecture in the form of inverse nanotubes. By precisely controlling the current pulse, the PEDOT can be easily deposited on either side of the nanotubes or in the spaces between the tubes as schematically illustrated in Figure 3.26a. Figure 3.26b displays the backscattered electron micrograph for the hybrid TiO_2-PEDOT where the PEDOT phase can be easily verified since the heavy metal titanium disperses more electrons (bright regions) while the polymer is highly translucent to the electron beam. The charge separation properties of the hybrids were also investigated via the electrochemical impedance analysis where it is clearly obvious that the charge transfer process is strongly influenced by the presence polymer phase. The Nyquist plot displayed in Figure 3.26c shows that the charge transfer resistance was decreased by almost three times upon the deposition of PEDOT. The authors further demonstrated that precise control of

the electrodeposition process may lead to production of more innovative nanostructures. For example, the spaces within the tubes could be infiltrated with the PEDOT and the spaces inside the tubes could also be infiltrated with another polymer having different HUMO and LUMO levels yielding the existence of polymer A - TiO$_2$ - polymer B hybrid photoelectrodes which could have interesting characteristics and be able to perform in various electronic and electrochemical applications [44].
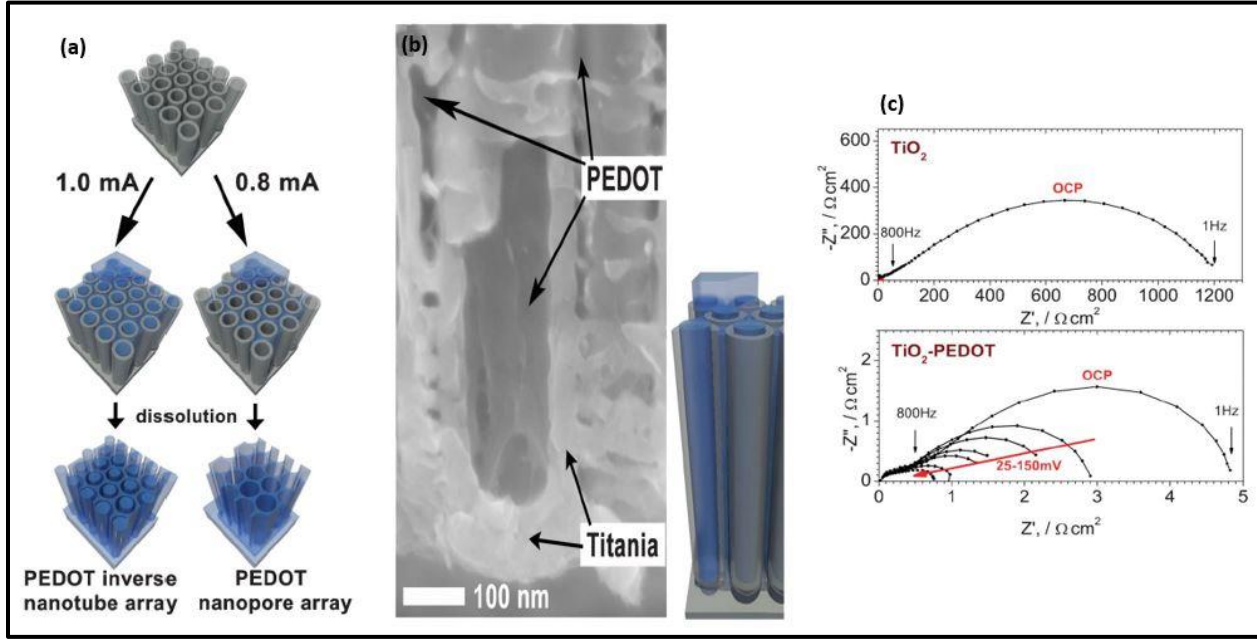
Figure 3.26: (a) Fabrication of PEDOT inverse nanotube array and nanopore array by electrodeposition with a pulse current at 1.0 and 0.8 mA respectively. (b) Backscattered-electron image of TiO$_2$-PEDOT hybrids fabricated at pulse current of 0.85 mA. (c) Nyquist impedance of (a) TiO$_2$ and (b) TiO$_2$ –PEDOT at open circuit potential [44].

The behavior of the PEDOT deposited on the TiO$_2$ semiconducting substrates was further described by Nagaboyamahina et al. who performed electrochemical characterization techniques analyzing the alteration of the semiconducting characteristics of the substrate arising from the polymer loading [45]. The authors utilized an equivalent theoretical model suggested by Deslouis et al. [46] to compare the behavior of the TiO$_2$-PEDOT nanostructures with respect to the pure TiO$_2$ nanotubes. For the estimation of the charge separation and transport, the theoretical expressions of impedance Z for a polymer layer deposited on the semiconductor substrate are described in the following manner:

$$Z = R_s + Z_{me} \tag{3.15}$$

$$\text{With } Z_{me} = \frac{Z_e}{1+j\omega C_e Z_e} + \frac{Z_i}{1+j\omega C_i Z_i} + Z_p \tag{3.16}$$

Where, R$_s$ is the resistance of the electrolyte, Z$_e$ is the impedance at the substrate/polymer interface described by a transfer resistance R$_e$ and a double layer capacitance C$_e$, Z$_i$ is the impedance at the polymer/electrolyte interface described by a transfer resistance R$_i$ and a double layer capacitance C$_i$ and Z$_p$ is the impedance of the polymer having resistance R$_p$.

57

The terms of Z_e, Z_i and Z_p are defined in the following manner:

$$Z_e = R_e + \frac{R_p + D_e}{8\,D_i}\left[\frac{\coth v}{v} - \frac{\text{th } v}{v}\right] \qquad (3.17)$$

$$Z_i = R_i + \frac{R_p + D_e}{8\,D_i}\left[\frac{\coth v}{v} + \frac{\text{th } v}{v}\right] \qquad (3.18)$$

$$Z_p = R_p + \frac{R_p + D_e}{4\,D_i}\left[\frac{\text{th } v}{v}\right] \qquad (3.19)$$

$$v^2 = \frac{j\,w\,d^2}{8D_i} \qquad (3.20)$$

Where d is the thickness of the polymer, ω is the angular frequency and $j = \sqrt{-1}$.

Considering the existence of the semiconductor substrate, an additional impedance Z_{SC} should be taken into consideration. Where, $Z_{sc} = \frac{R_{sc}}{1 + j\,\omega\,R_{sc}\,C_{sc}}$ (3.21)

Where C_S is the capacitance of the double layer and R_{sc} is the intrinsic resistance of the semiconductor. Besides, an additional resistance R_{ad} should not be neglected which is ascribed to a very thin polymer layer deposited over some regions of the substrate and not apparent by SEM. Accordingly, for the case when the polymer layer completely covers the whole surface of the semiconductor, Z_{me} and Z_{sc} are in series (Figure 3.27a). Whereas, when there are some discontinuities, Z_{me} should be in parallel with R_{ad} and Z_{sc} (Figure 3.27b).

Figure 3.27c demonstrates the Nyquist plot of the hybrid TiO_2-PEDOT. It is obvious from the plot the existence of the straight line in the low frequency region illustrating a lower ratio of D_e/D_i due to the intrinsic resistance of the polymer film which decreases the diffusion coefficient of the electrons within PEDOT. The modification of the parameters relevant to the semiconductor (R_{sc} and C_{sc}) is depicted in Figure 3.27d and e. The R_{sc} behavior shows an almost constant value of nearly 40 Ω at high potential ranges followed by a subsequent increase at lower potential ranges. The Mott-Schottky diagram illustrates the variation of $(1/C_{sc})^2$ as a function of the applied voltage. It was shown that the flat band potential for the pure TiO_2 is about -0.25 V vs SCE whereas, a negative shift is obtained after the deposition of PEDOT to about -0.4 V vs SCE. The previous values indicate that PEDOT promotes the photoexcited electrons separation and transfer. It is worth to note the high extent of discrepancy in the shape of the Mott-Schottky plot between the hybrid photoelectrode and the pure TiO_2. The presence of a jump in $1/C^2$ in the hybrid photoelectrode indicates electron trapping by the surface states of the semiconductor in the range from 0 to 0.2 V vs SCE which combine with the domain of PEDOT oxidation as indicated by the cyclic voltammogram shown in Figure 3.27f. These results support the claim that the trapped electrons are a consequence of the oxidation of the polymer [45].
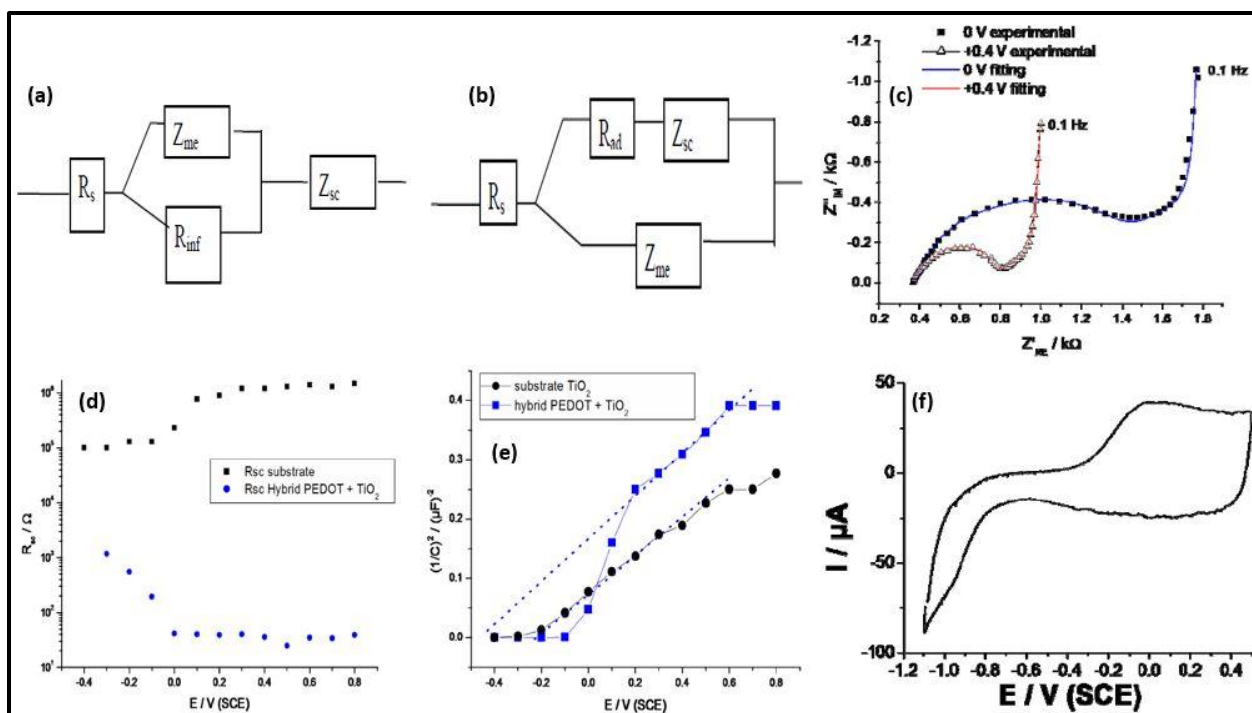
Figure 3.27: (a and b) equivalent circuits to describe the electrochemical behavior for TiO₂-PEDOT hybrids measured in LiClO₄ acetonitrile solution, (c) Corresponding EIS Nyquist plot and its fitted curves, (d) Variation of Rsc as a function of applied voltage for pure TiO₂ and hybrid TiO₂-PEDOT in LiClO₄, (e) Variation of $1/C^2$ as a function of applied voltage for pure TiO₂ and hybrid TiO₂-PEDOT in LiClO₄ and (f) Cyclic voltammogram for hybrid TiO₂-PEDOT after 40 cycles [45].

The role of PEDOT in photoelectrochemical water splitting has been further investigated with other inorganic semiconductors. Li et al. studied the photoactive performance of Si-PEDOT core-shell heterostructure fabricated by a chemical assisted etching followed by a vapor-phase polymerization of PEDOT for the decomposition of water under solar simulated irradiation. The authors showed that (3-aminopropyle) triethoxysilane (APS) adjusted Si nanowires possess a better PEDOT adhesion than the unadjusted arrays and hence an improved photocurrent spectral response as well as photostability. Figure 3.28A displays the photocurrent response for the hybrid photoelectrodes as well as the pure SiO₂ nanowires. The dark current of pure Si shows a plateau in the voltage range from -0.5 to 0 V vs SCE which is attributed to the oxidation of Si. The photocurrent behavior exhibited a subsequent decline at higher voltages values. Upon illumination, the Si nanowires exhibited almost the same behavior as that obtained under dark current other than that the peak at the beginning which is shifted to a more negative potential. However, the hybrid Si-PEDOT as well as the adjusted Si-APS-PEDOT showed an improved photocurrent response that reached values of 2.3 mA/cm² for the Si-PEDOT and 2.5 mA/cm² for the adjusted Si-APS-PEDOT which indicates that the APS layer between Si and PEDOT was able to minimize the leakage current as well as maintain a low contact resistance. Figure 3.28B displays the photocurrent stability of the fabricated samples where the pure Si shows a fast decay in the photocurrent within the intensively corrosive 1 M KOH media. This behavior is clear from the SEM image illustrated in Figure 3.28C (panel d) which shows an absolute corrosion for the nanowires in a period of three minutes. However, the hybrid Si-PEDOT samples exhibited an enhanced photostability with a photocurrent of 0.76 mA/cm² which illustrates that PEDOT is efficient in preserving the Si nanowires from the electrolyte and prevent photocorrosion. It was also shown that the adjusted Si-APS-PEDOT hybrids exhibited the optimum photostability with

a photocurrent of 1.2 mA/cm^2 within 10 minutes. The behavior was confirmed by the SEM image shown in Figure 3.27C (panel f) with no apparent change from the original morphology. It was reported that PEDOT can serve as multi-functional coating to protect the Si nanowires from photocorrosion and act as a photosensitizer to advance the oxygen-evolution reaction [47].
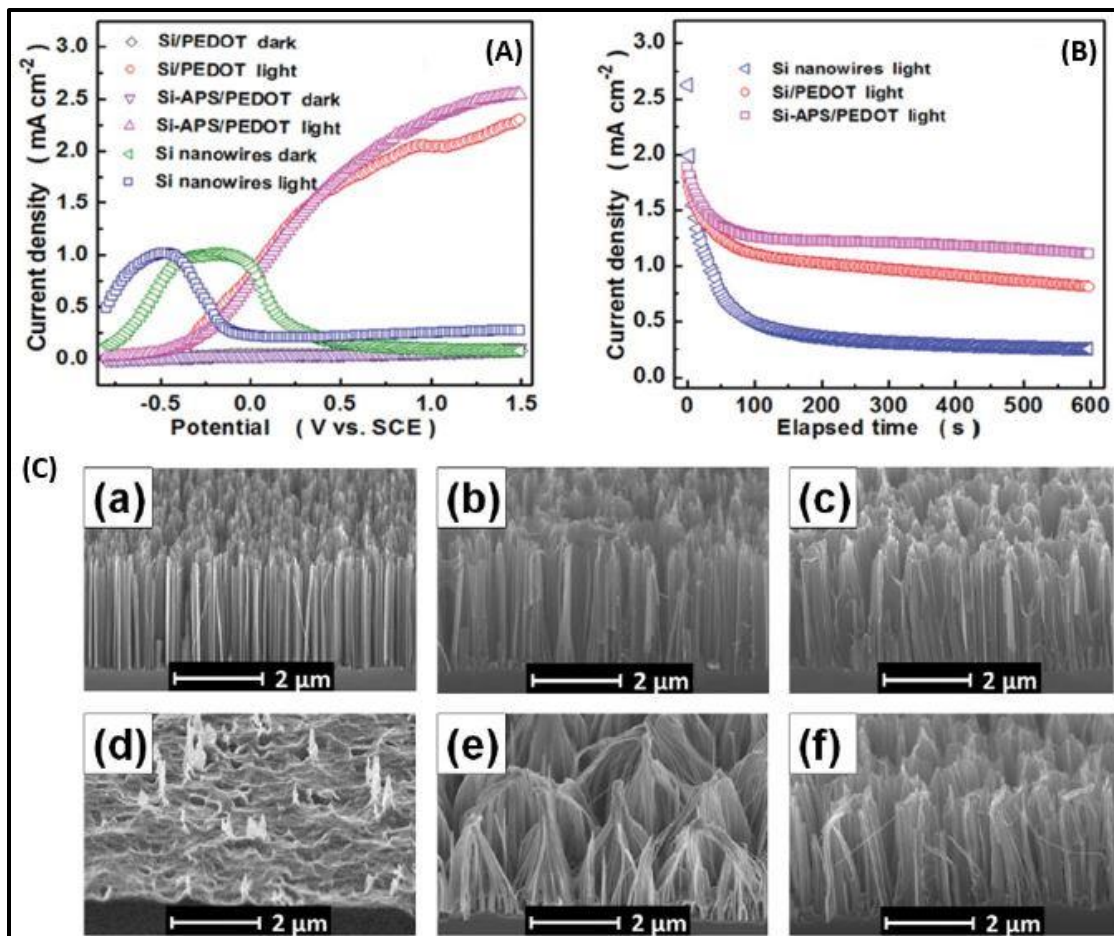
Figure 3.28 (A) Linear sweep voltammetry of pure Si nanowires, hybrid Si-PEDOT and modified Si-APS-PEDOT under dark or 100 mW cm-2 illumination. (B) Corresponding amperometric curves under 100 mW cm-2 at +0.5 V (vs SCE) (C) SEM images for (a) Si nanowire array, (b) Hybrid Si-PEDOT, (c) Modified Si-APS-PEDOT, (e-f) Corresponding SEM images after PEC test for 3 min, 1 h and 1.5 h respectively [47].

Based on the above literature survey, it can be observed that PEDOT is a very promising photosensitizer to be coupled with TiO$_2$ nanotubes due to its ideal band gap (1.6 eV) that could tremendously improve the visible light absorption properties as well as the photocurrent spectral response. The utilization of modified PEDOT, that is poly(3,4-ethylenedioxythiophene):poly(styrenesulfonate), (PEDOT:PSS) or PEDOT modified by Prussian blue to sensitize TiO$_2$ was described by another groups [44,48]. However, due to the superior electrocatalytic behavior and the high photostability of PEDOT without modifications [29] there is a prospect to couple intrinsic PEDOT with TiO$_2$ as a hybrid photoanode for water splitting. The nanocomposite will be developed by electrochemical anodization of Ti followed by spin coating of PEDOT nano thin films prepared by oxidative polymerization. We expect to maintain efficient visible-light driven water splitting.

References

1. E. Panaitescu, C. Richter and L. Menon, "A Study of Titania Nanotube Synthesis in Chloride-Ion-Containing Media", *Journal of The Electrochemical Society*, vol. 155, no. 1, p. E7, 2008.

2. G. Mor, O. Varghese, M. Paulose, K. Shankar and C. Grimes, "A review on highly ordered, vertically oriented TiO_2 nanotube arrays: Fabrication, material properties, and solar energy applications", *Solar Energy Materials and Solar Cells*, vol. 90, no. 14, pp. 2011-2075, 2006.

3. M. San Miguel, C. Calzado and J. Fernández Sanz, "First principles study of Na adsorption on TiO_2 (110) surface", *International Journal of Quantum Chemistry*, vol. 70, no. 2, pp. 351-357, 1998.

4. V. Brezová, A. Blažková, Ľ. Karpinský, J. Grošková, B. Havlínová, V. Jorík and M. Čeppan, "Phenol decomposition using $Mn+/TiO_2$ photocatalysts supported by the sol-gel technique on glass fibres", *Journal of Photochemistry and Photobiology A: Chemistry*, vol. 109, no. 2, pp. 177-183, 1997.

5. T. López, J. Hernandez-Ventura, R. Gómez, F. Tzompantzi, E. Sánchez, X. Bokhimi and A. García, "Photodecomposition of 2,4-dinitroaniline on Li/TiO_2 and Rb/TiO_2 nanocrystallite sol–gel derived catalysts", *Journal of Molecular Catalysis A: Chemical*, vol. 167, no. 1-2, pp. 101-107, 2001.

6. W. Choi, A. Termin and M. Hoffmann, "The Role of Metal Ion Dopants in Quantum-Sized TiO_2: Correlation between Photoreactivity and Charge Carrier Recombination Dynamics", *The Journal of Physical Chemistry*, vol. 98, no. 51, pp. 13669-13679, 1994.

7. S. Bouattour, W. Kallel, A. Botelho do Rego, L. Vieira Ferreira, I. Machado and S. Boufi, "Li-doped nanosized TiO_2 powder with enhanced photocalatylic acivity under sunlight irradiation", *Applied Organometallic Chemistry*, vol. 24, no. 10, pp. 692-699, 2010.

8. Y. Chen, C. Lee, M. Yeng and H. Chiu, "The effect of calcination temperature on the crystallinity of TiO_2 nanopowders", *Journal of Crystal Growth*, vol. 247, no. 3-4, pp. 363-370, 2003.

9. Y. Bessekhouad, D. Robert, J. Weber and N. Chaoui, "Effect of alkaline-doped TiO_2 on photocatalytic efficiency", *Journal of Photochemistry and Photobiology A: Chemistry*, vol. 167, no. 1, pp. 49-57, 2004.

10. A. Morawski, J. Grzechulska and K. Kałucki, "A new method for preparation of potassium-pillared layered titanate applied in photocatalysis", *Journal of Physics and Chemistry of Solids*, vol. 57, no. 6-8, pp. 1011-1017, 1996.

11. J. Grzechulska, "Photocatalytic decomposition of oil in water", *Water Research*, vol. 34, no. 5, pp. 1638-1644, 2000.

12. S. Cheng, "Photocatalytic decomposition of phenol over titanium oxide of various structures", *Catalysis Today*, vol. 26, no. 1, pp. 87-96, 1995.

13. C. Richter, C. Jaye, E. Panaitescu, D. Fischer, L. Lewis, R. Willey and L. Menon, "Effect of potassium adsorption on the photochemical properties of titania nanotube arrays", *Journal of Materials Chemistry*, vol. 19, no. 19, pp. 2963-2967, 2009.

14. C. Richter and L. Menon, "Impact of adsorbed alkali ions on photoelectrochemical hydrogen production by titania nanotubes", *Energy & Environmental Science*, vol. 3, no. 4, pp. 427-433, 2010.

15. Y. Inoue, T. Kubokawa and K. Sato, "Photocatalytic activity of alkali-metal titanates combined with ruthenium in the decomposition of water", *The Journal of Physical Chemistry*, vol. 95, no. 10, pp. 4059-4063, 1991.

16. T. Sakata, K. Hashimoto and T. Kawai, "Catalytic properties of ruthenium oxide on n-type semiconductors under illumination", *The Journal of Physical Chemistry*, vol. 88, no. 22, pp. 5214-5221, 1984.

17. S. Ogura, M. Kohno, K. Sato and Y. Inoue, "Photocatalytic activity for water decomposition of RuO_2-combined $M_2Ti_6O_{13}$ (M = Na, K, Rb, Cs)", *Applied Surface Science*, vol. 121-122, pp. 521-524, 1997.

18. S. Ogura, M. Kohno, K. Sato and Y. Inoue, "Photocatalytic properties of $M_2Ti_6O_{13}$ (M=Na, K, Rb, Cs) with rectangular tunnel and layer structures: Behavior of a surface radical produced by UV irradiation and photocatalytic activity for water decomposition", *Physical Chemistry Chemical Physics*, vol. 1, no. 1, pp. 179-183, 1999.

19. M. Graetzel and F. Rotzinger, "Raman spectroscopic evidence for the existence of titanyl (TiO^{2+}) in acidic aqueous solutions", *Inorganic Chemistry*, vol. 24, no. 14, pp. 2320-2321, 1985.

20. S. Andersson and A. Wadsley, "The structures of $Na_2Ti_6O_{13}$ and $Rb_2Ti_6O_{13}$ and the alkali metal titanates", *Acta Crystallographica*, vol. 15, no. 3, pp. 194-201, 1962.

21. L. Yu, Q. Wang, Q. Zhi, K. Dong, Q. Xue and Z. Yaping, "Photoelectrochemical Properties of Alkali Metal Doped TiO_2 Nano-Honeycomb Film", *Energy and Environment Focus*, vol. 4, no. 3, pp. 191-195, 2015.

22. K. Yamaguti and S. Sato, "Photolysis of water over metallized powdered titanium dioxide", *Journal of the Chemical Society, Faraday Transactions 1: Physical Chemistry in Condensed Phases*, vol. 81, no. 5, pp. 1237-1246, 1985.

23. S. Ma, T. Hisatomi, K. Maeda, Y. Moriya and K. Domen, "Enhanced Water Oxidation on Ta_3N_5 Photocatalysts by Modification with Alkaline Metal Salts", *Journal of the American Chemical Society*, vol. 134, no. 49, pp. 19993-19996, 2012.

24. Y. Kado, R. Hahn, C. Lee and P. Schmuki, "Strongly enhanced photocurrent response for Na doped Ta_3N_5-nano porous structure", *Electrochemistry Communications*, vol. 17, pp. 67-70, 2012.

25. J. Xu, C. Ma, M. Balasubramanian and Y. Meng, "Understanding $Na_2Ti_3O_7$ as an ultra-low voltage anode material for a Na-ion battery", *Chem. Commun.*, vol. 50, no. 83, pp. 12564-12567, 2014.

26. J. Eid, A. Usman, I. Gereige, J. Duren, V. Lyssenko, K. Leo and O. Mohammed, "Ultrafast pump-probe reflectance spectroscopy: Why sodium makes $Cu(In,Ga)Se_2$ solar cells better", *Solar Energy Materials and Solar Cells*, vol. 140, pp. 33-37, 2015.

27. S. Wei, S. Zhang and A. Zunger, "Effects of Na on the electrical and structural properties of $CuInSe_2$", *Journal of Applied Physics*, vol. 85, no. 10, pp. 7214-7218, 1999.

28. A. Rockett, "The effect of Na in polycrystalline and epitaxial single-crystal $CuIn_{1-x}Ga_xSe_2$", *Thin Solid Films*, vol. 480-481, pp. 2-7, 2005.

29. B. Winther-Jensen and D. MacFarlane, "New generation, metal-free electrocatalysts for fuel cells, solar cells and water splitting", *Energy & Environmental Science*, vol. 4, no. 8, pp. 2790-2798, 2011.

30. G. Yu, J. Gao, J. Hummelen, F. Wudl and A. Heeger, "Polymer Photovoltaic Cells: Enhanced Efficiencies via a Network of Internal Donor-Acceptor Heterojunctions", *Science*, vol. 270, no. 5243, pp. 1789-1791, 1995.

31. S. Park, A. Roy, S. Beaupré, S. Cho, N. Coates, J. Moon, D. Moses, M. Leclerc, K. Lee and A. Heeger, "Bulk heterojunction solar cells with internal quantum efficiency approaching 100%", *Nature Photonics*, vol. 3, no. 5, pp. 297-302, 2009.

32. R. Bashyam and P. Zelenay, "A class of non-precious metal composite catalysts for fuel cells", *Nature*, vol. 443, no. 7107, pp. 63-66, 2006.

33. Y. Cao, G. Yu, C. Zhang, R. Menon and A. Heeger, "Polymer light-emitting diodes with polyethylene dioxythiophene–polystyrene sulfonate as the transparent anode", *Synthetic Metals*, vol. 87, no. 2, pp. 171-174, 1997.

34. G. Milczarek and O. Inganas, "Renewable Cathode Materials from Biopolymer/Conjugated Polymer Interpenetrating Networks", *Science*, vol. 335, no. 6075, pp. 1468-1471, 2012.

35. P. Kulesza, M. Matczak, A. Wolkiewicz, B. Grzybowska, M. Galkowski, M. Malik and A. Wieckowski, "Electrocatalytic properties of conducting polymer based composite film containing dispersed platinum microparticles towards oxidation of methanol", *Electrochimica Acta*, vol. 44, no. 12, pp. 2131-2137, 1999.

36. A. Mourato, S. Wong, H. Siegenthaler and L. Abrantes, "Polyaniline films containing palladium microparticles for electrocatalytic purposes", *Journal of Solid State Electrochemistry*, vol. 10, no. 3, pp. 140-147, 2005.

37. D. Wang, J. Zhang, Q. Luo, X. Li, Y. Duan and J. An, "Characterization and photocatalytic activity of poly(3-hexylthiophene)-modified TiO_2 for degradation of methyl orange under visible light", *Journal of Hazardous Materials*, vol. 169, no. 1-3, pp. 546-550, 2009.

38. J. Huang, M. Ibrahem and C. Chu, "Interfacial engineering affects the photocatalytic activity of poly(3-hexylthiophene)-modified TiO_2", *RSC Advances*, vol. 3, no. 48, pp. 26438-26442, 2013.

39. X. Li, D. Wang, G. Cheng, Q. Luo, J. An and Y. Wang, "Preparation of polyaniline-modified TiO_2 nanoparticles and their photocatalytic activity under visible light illumination", *Applied Catalysis B: Environmental*, vol. 81, no. 3-4, pp. 267-273, 2008.

40. Y. Lin, D. Li, J. Hu, G. Xiao, J. Wang, W. Li and X. Fu, "Highly Efficient Photocatalytic Degradation of Organic Pollutants by PANI-Modified TiO_2 Composite", *The Journal of Physical Chemistry C*, vol. 116, no. 9, pp. 5764-5772, 2012.

41. X. Li, J. Sun, G. He, G. Jiang, Y. Tan and B. Xue, "Macroporous polypyrrole-TiO_2 composites with improved photoactivity and electrochemical sensitivity", *Journal of Colloid and Interface Science*, vol. 411, pp. 34-40, 2013.

42. X. Li, G. Jiang, G. He, W. Zheng, Y. Tan and W. Xiao, "Preparation of porous PPy-TiO_2 composites: Improved visible light photoactivity and the mechanism", *Chemical Engineering Journal*, vol. 236, pp. 480-489, 2014.

43. J. Luo, Y. Ma, H. Wang and J. Chen, "Preparation of polypyrrole sensitized TiO_2 nanotube arrays hybrids for efficient photoelectrochemical water splitting", *Electrochimica Acta*, vol. 167, pp. 119-125, 2015.

44. D. Kowalski, S. Albu and P. Schmuki, "Current dependent formation of PEDOT inverse nanotube arrays", *RSC Advances*, vol. 3, no. 7, pp. 2154-2157, 2013.

45. E. Ngaboyamahina, H. Cachet, A. Pailleret and E. Sutter, "Electrochemical impedance spectroscopy characterization of conducting polymer/TiO_2 nanotube array hybrid structures", *Journal of Electroanalytical Chemistry*, vol. 737, pp. 37-45, 2015.

46. C. Deslouis, T. El Moustafid, M. Musiani and B. Tribollet, "Mixed ionic-electronic conduction of a conducting polymer film. Ac impedance study of polypyrrole", *Electrochimica Acta*, vol. 41, no. 7-8, pp. 1343-1349, 1996.

47. X. Li, W. Lu, W. Dong, Q. Chen, D. Wu, W. Zhou and L. Chen, "Si/PEDOT hybrid core/shell nanowire arrays as photoelectrodes for photoelectrochemical water-splitting", *Nanoscale*, vol. 5, no. 12, pp. 5257-5261, 2013.

48. K. Siuzdak, M. Szkoda, J. Karczewski, J. Ryl and A. Lisowska-Oleksiak, "Titania nanotubes infiltrated with the conducting polymer PEDOT modified by Prussian blue – a novel type of organic–inorganic heterojunction characterised with enhanced photoactivity", *RSC Adv.*, vol. 6, no. 80, pp. 76246-76250, 2016.

Chapter 4

Experimental Methods and Materials

4.1 Materials and Supplies

Titanium foil with thickness 0.25 mm and purity 99.95 % was purchased from Alfa Aesar. Formamide (anhydrous) 99.8 %, Ammonium Fluoride (NH$_4$F) A.C.S. reagent 98 + % purity, were purchased from Sigma Aldrich. 3,4-Ethylenedioxythiophene, Iron (III) P-toluenesulfonate were purchased from Sigma Aldrich with purity 99.99 %. The photoelectrochemical (PEC) characterization was performed in collaborative work with Swiss Federal Laboratories for Materials Science and Technology (EMPA) in Dubendorf, Switzerland.

4.2 Potentiostatic Anodization

Before anodization, Ti foil was ultrasonically cleaned in aceton, ethyl alcohol and distilled water. The electrochemical oxidation was implemented in a two-electrode configuration with Ti metal acting as working electrode and Pt foil acting as a cathode. Agielnt E3612A DC power supply was employed to provide the necessary voltage. The samples were rinsed in deionized water and ethyl alcohol after removal from the anodization bath then dried with nitrogen blowing. The potentiostatic anodization setup is displayed in Figure 4.1.
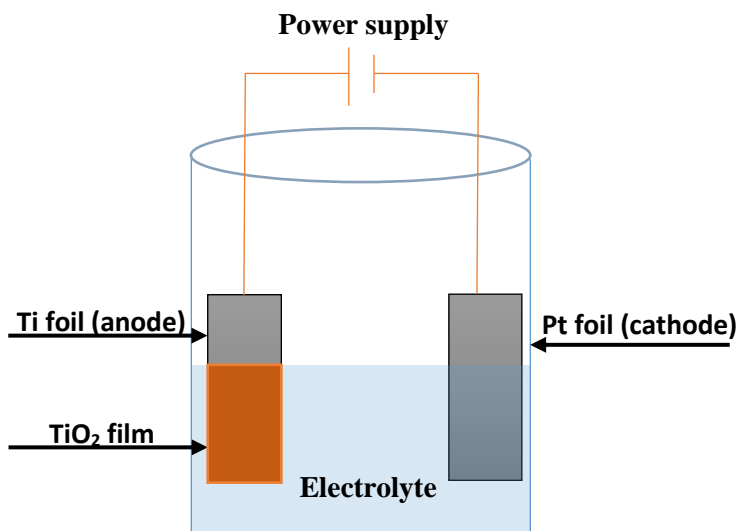
Figure 4.1: Schematic illustration of potentiostatic anodization setup.

4.3 Thermal Annealing

The as-prepared samples were loaded in a muffle furnace to crystallize the structure. Constant flow of air was conserved during the annealing process. The temperature was raised from room temperature up to 450°C by a ramp rate of 1°C/min and kept constant for 4 hours then permitted to cool back again to room temperature.

4.4 Soaking Treatment

Na-modified TiO_2 photoelectrodes were developed by immersing TiO_2 substrates in two aqueous solutions containing various concentrations of NaOH and Na_2SO_4 at room temperature and same concentration for NaOH at 80°C.

4.5 Solution Casting Polymerization

PEDOT nano thin films were prepared by straightforward casting process. EDOT acts as the monomer utilized in the polymerization of PEDOT since it is simple to derivatize (produce the reaction's products) and obtain multi-ring monomers with extended π system. Chemical oxidant (Iron-III p-toluenesulfonate) is used as an efficient and non-toxic catalyst to oxidize the monomer and produce the polymer chain via the reaction between Iron (III) salt and the monomer. Pyridine acts as a base to impair the immense reactivity of Iron-III p-toluenesulfonate [1-3]. Accordingly the exact synthesis protocol is descrbed as follows:

1.85 g of isopropanol is added to 1.07 g of Iron-III p-toluenesulfonate and this blend is stirred for 1 hour at room temperature. An amount of 0.06 g of pyridine is then added to the obtained solution and mixed for an additional hour. Ethylenedioxythiophene (EDOT) is finally added to the mixture and stirred for 5 more minutes and then spin-coated over the scaffolds at 2500 rpm for 40 seconds. The scaffolds were then heated at 60°C to produce oxidative polymerization [4].

4.6 Spin Coating

Spin coating method was used for the application of PEDOT nano thin films onto the TiO_2 scaffold. Depositing various amount of the liquid resin onto the substrate and then spinning the substrate at 2500 rpm for a period of 40 seconds. Central acceleration will spread the solution to the edges of the scaffold forming a thin film of the polymer over the TiO_2 nanotubes surfaces'.

4.7 Morphological and Crystal Structural Characterization

The morphological and surface structure was inspected using field emission scanning electron microscope FESEM Zeiss Ultra-60. The InLens detector was mainly utilized because it is located at a proper inclination from the sample holder. The SE2 detector was not used since it does not yield good resolution images at short working distances. The crystalline phases analysis was done using X-ray diffractometer (XRD; PANalytical X'pert PRO diffractometer with Cu Kα radiations at $\lambda = 1.54059$ Å). The X-ray tube is immobile, whereas the sample holder and the detector are revolving at an angle of θ and 2θ respectively [5].

Fourier Transform Infrared (FTIR) was utilized to analyze the vibrational excitations of the polymers species by FT-IR spectrometer (Thermo Nicolet Model 380) supplied with DTGS detector. All spectra were gathered for 256 interferograms at a resolution of 4 cm^{-1}. Raman analysis was done on a Raman microscope (ProRaman-L Analyzer) using excitation wavelength of 532 nm.

4.8 Optical and Photoelectrochemical Measurements

The optical properties were evaluated by Cary 5000 UV/vis/NIR spectrophotometer with a sample holder for reflectance measurements and an integrated sphere. The photo-electrochemical measurements of the Na-modified TiO_2 photoelectrodes were performed in 0.05 M $Ba(OH)_2$ solution with saturated Ag/AgCl reference electrode and Pt cathode. Whereas, the photo electrochemical properties for the PEDOT-TiO_2 hybrid photoanodes were examined in 1 M KOH with saturated Ag/AgCl reference electrode and Pt cathode. A scanning potentiostat was utilized to obtain dark and illuminated currents at a scan rate 10 mV/s where potential sweeps from -1.23 V to +1.23 V vs Ag/AgCl and the solar energy was simulated by xenon lamp at 100 mW cm^{-2}. The assembly of the electrochemical setup is shown in Figure 4.2.

Electrochemical impedance spectra (EIS) were collected in intervals of 200 mV from -1000mV to 600 mV at frequencies of 100 KHz to 50 mHz. EC-Lab software was utilized to fit the collected spectra according to the appropriate equivalent circuits and Mott-Schottky plots were adjusted and demonstrated vs Ag/AgCl.
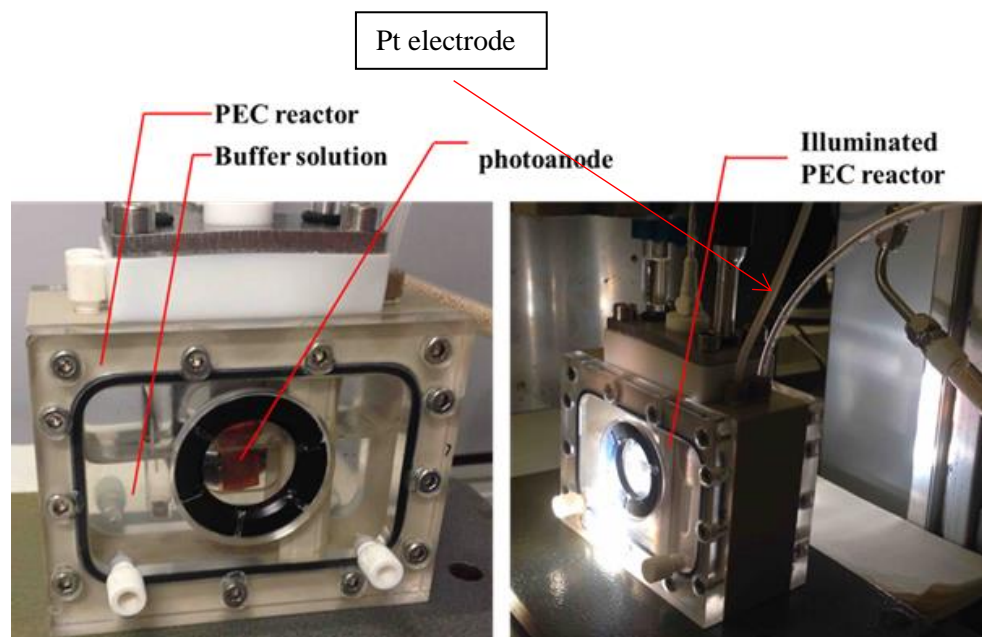
Figure 4.2: Setup of PEC reactor including PEC photoanode (left). Image of a working PEC reactor (right). Images were captured at EMPA Dübendorf.
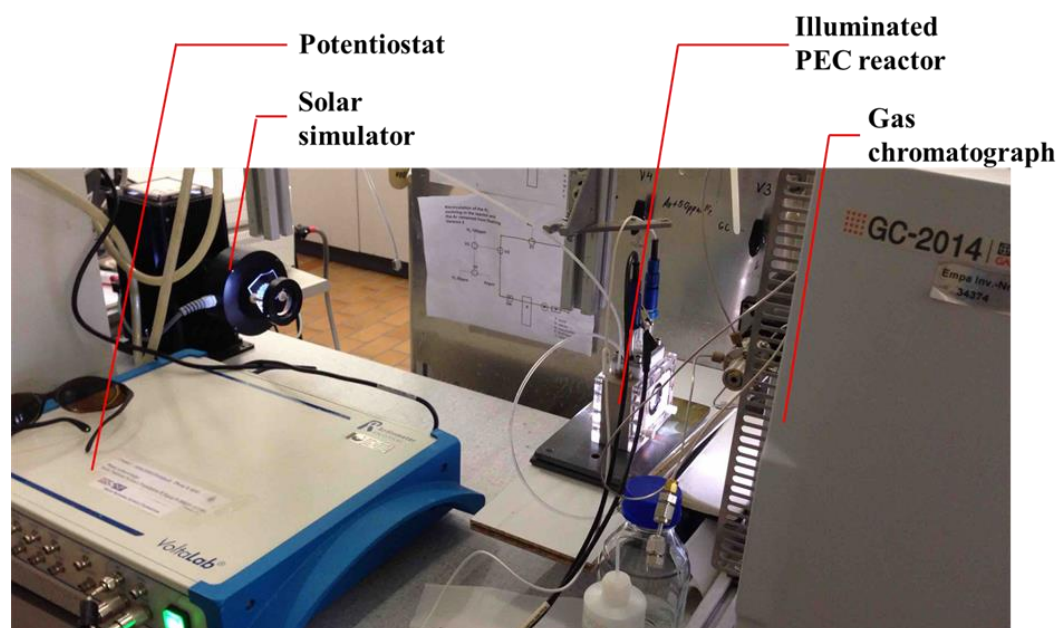
Figure 4.3: The PEC workstation at EMPA Dübendorf.

4.9 Density Functional Theory Calculations

All the estimations of the Projective Density Of State (PDOS) as well as the band structure for the pure and Na-modified TiO_2 were implemented by Quantum Espresso software package with plane wave basis sets where less than 0.0001 Ry/Bohr force was adjusted for attaining minimum energy configurations. Calculations were performed by a 3x3x3 Monkhorst-Pack k-point grid, with an energy cutoff of 45 Ry, using the generalized gradient approximation PBE functional [6].

References

1. G. A. Sotzing, J. R. Reynolds, and P. J. Steel, "Poly(3,4-ethylenedioxythiophene) (PEDOT) prepared via electrochemical polymerization of EDOT, 2,2'-Bis(3,4-ethylenedioxythiophene) (BiEDOT), and their TMS derivatives", *Advanced Materials*, vol. 9, no. 10, pp. 795–798, 1997.

2. M. A. Ali, H. Kim, C. Lee, H. Nam, and J. Lee, "Effects of iron(III) p-toluenesulfonate hexahydrate oxidant on the growth of conductive poly(3,4-ethylenedioxythiophene) (PEDOT) nanofilms by vapor phase polymerization", *Synthetic Metals*, vol. 161, no. 13-14, pp. 1347–1352, 2011.

3. T. Park, C. Park, B. Kim, H. Shin, and E. Kim, "Flexible PEDOT electrodes with large thermoelectric power factors to generate electricity by the touch of fingertips", *Energy & Environmental Science*, vol. 6, no. 3, pp. 788–792, 2013.

4. J. You, J. Heo, J. Kim, T. Park, B. Kim, H. Kim, Y. Choi, H. Kim and E. Kim, "Noninvasive Photodetachment of Stem Cells on Tunable Conductive Polymer Nano Thin Films: Selective Harvesting and Preserved Differentiation Capacity", *ACS Nano*, vol. 7, no. 5, pp. 4119-4128, 2013.

5. A. Terent'ev, V. Vil, I. Yaremenko, O.Bityukov, D. Levitsky, V. Chernyshev, G. Nikishin and F. Fleury, "Preparation of a microsized cerium chloride-based catalyst and its application in the Michael addition of β-diketones to vinyl ketons", *New J. Chem.*, vol. 38, no. 4, pp. 1493-1502, 2014.

6. J. Perdew, K. Burke and M. Ernzerhof, "Generalized Gradient Approximation Made Simple", *Physical Review Letters*, vol. 77, no. 18, pp. 3865-3868, 1996.

Chapter 5

Na-modified TiO$_2$ Photoanodes for Solar Fuel Generation: Experimental and Theoretical Insights

On the basis of the literature discussed in chapter 3, it is evident that the photoelectrochemical performance of the Na-modified TiO$_2$ photoelectrodes is mainly dependent on the Na doping procedure, the type of salts utilized, as well as its concentration. Since Na possesses a closed-shell electronic structure it is not expected to have considerable improvement on the absorption properties upon coupling with TiO$_2$. However, the improvement is expected in maintaining lower band bending requirements in order to reduce the external bias needed per liter of H$_2$ generated in pursuit of developing new photocatalysts that can break down H$_2$O unassisted by an external bias. An noticeable enhancement in the photocurrent spectral response by suppressing the electron-hole recombination pathway and improving the charge carriers separation is also expected.

In an attempt to achieve the above mentioned objective, the fabricated TiO$_2$ nanotubes were immersed in two aqueous solutions involving quantitative NaOH and Na$_2$SO$_4$ (0.05, 0.1, 0.2 and 0.4 M) at room temperature as well as the same concentration for NaOH at 80°C for a period of 30 mins. The fabricated photoelectrodes were readily get after drying in air at 100°C. The established treatment of NaOH and Na$_2$SO$_4$ didn't induce a noticeable variation in the crystal structure or the band gap of the pristine TiO$_2$ however, the photoelectrochemical activity was apparently enhanced after this simple soaking treatment.

Hereinafter, the results of the fabrication of such 1D Na-modified TiO$_2$ photoelectrodes formed via electrochemical anodization followed by soaking treatment are presented.

5.1 Morphological and Structural Characterization

The electrochemical oxidation of Ti in formamide electrolytes leads to the development of homogenous nanotubular structure that is covering the whole surface of the substrate with apparently invariable wall thickness all over the length of the tube and this in return has a decisive impact on the photocurrent produced [1,2]. For this reason the anodization was performed in formamide-based electrolyte including 0.56 g of ammonium fluoride and 5 mL deionized water at 20 V [3].

Figure 5.1 displays the morphology of the as-anodized TiO$_2$ nanotubes and the NaOH modified ones at room temperature. Figure 5.1a reveals the development of self-organized TiO$_2$ nanotubes with an average wall thickness of 10±2 nm and an average length of 7±2 µm. Figure 5.1 panels b-e reveal the morphology of the Na-modified TiO$_2$ nanotubes formed via soaking treatment of the array film detailed in Figure 5.1a in 0.05, 0.1, 0.2 and 0.4 M of NaOH at room temperature for 30 mins. We noticed the surface adsorption of NaOH amorphous layer composed of adsorbed Na$^+$ and OH$^-$ ions modifying the surface of the TiO$_2$ nanotubes with higher extent of the adsorbed ions formed upon increasing the concentration of the aqueous solution. Noteworthy is the inhomogeneity of the adsorbed layer and that there is no complete coverage attained over the top opening of the anodic nanotubes, however, the nanotubular structure is still very well

intact in all cases. It is interesting also to elucidate that this treatment is believed not to result in any intermediate compounds (such as sodium titanates) due to the controlled time and temperature adopted within the synthesis technique employed in this study which will be further confirmed by XRD patterns and Raman analyses. Figure 5.2 displays no major morphological changes upon carrying out the soaking treatment at 80°C. The surface layer didn't show any decay which indicates that the adsorbed ions seem to be stable under elevated temperatures.
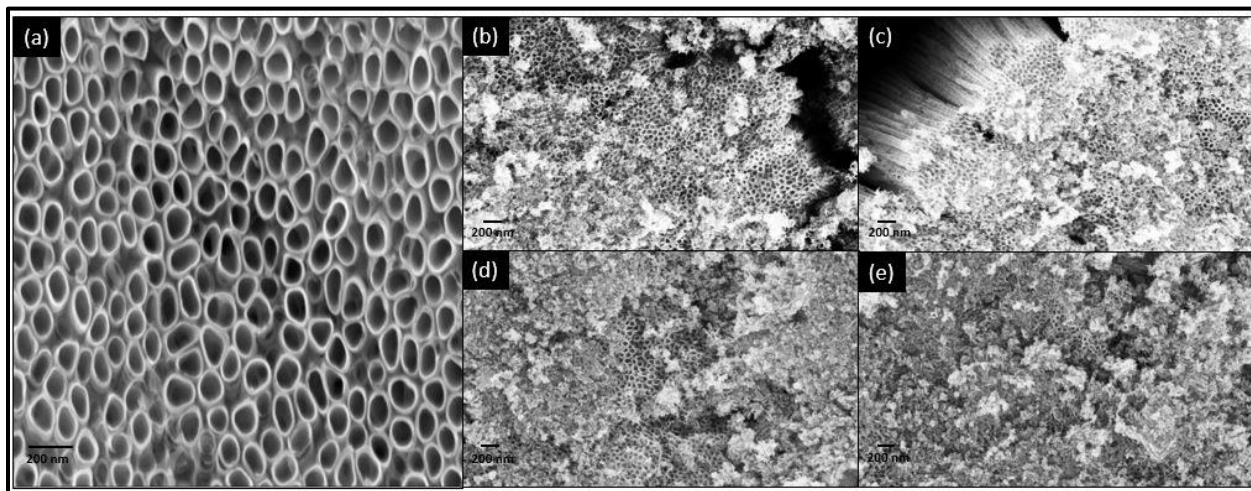
Figure 5.1: FESEM top-view images of (a) as-anodized TiO$_2$ nanotubes, and the Na-modified TiO$_2$ nanotubes formed via soaking in (b) 0.05 M, (c) 0.1 M, (d) 0.2 M and (e) 0.4 M NaOH for 30 min at room temperature.
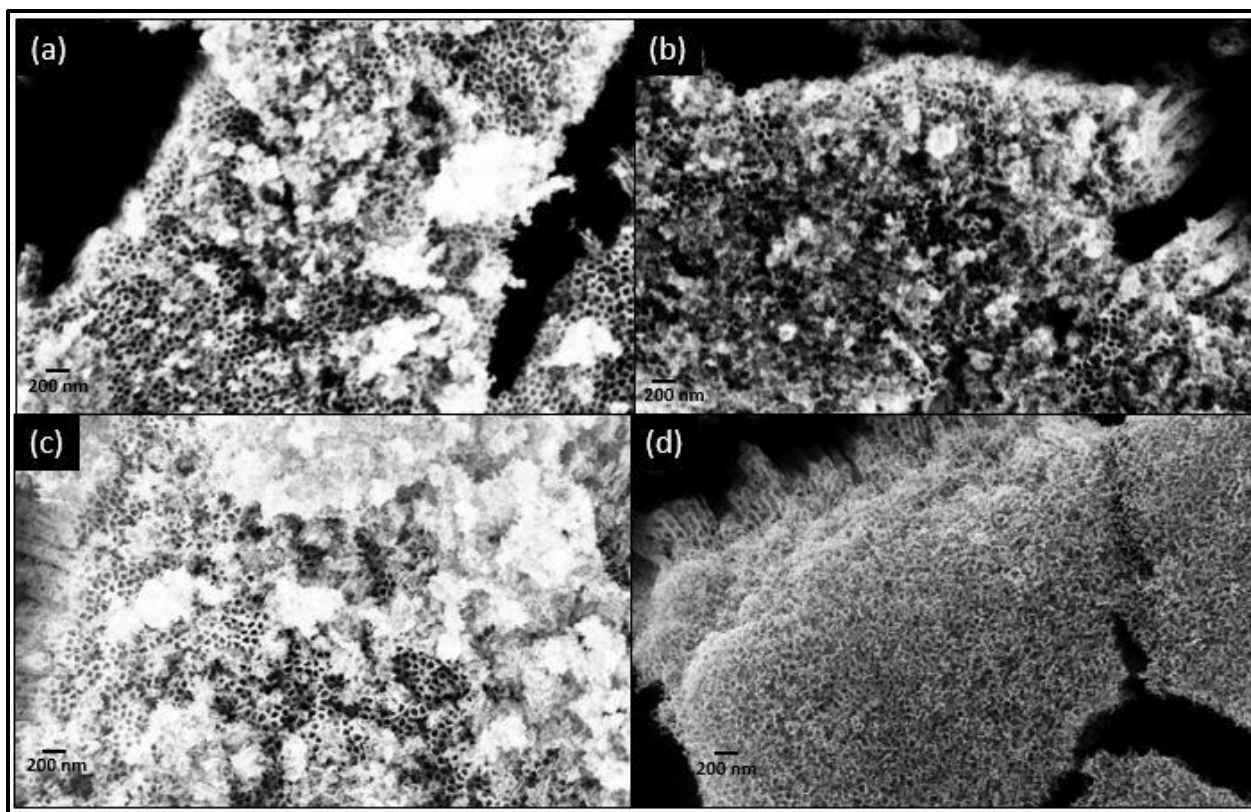
Figure 5.2: FESEM top-view images of Na-modified TiO$_2$ nanotubes formed via soaking in (a) 0.05 M, (b) 0.1 M, (c) 0.2 M and (d) 0.4 M NaOH for 30 min at 80°C.

The same approach applies for the morphology of Na-modified TiO$_2$ nanotubes formed via soaking treatment in 0.05, 0.1, 0.2 and 0.4 M of Na$_2$SO$_4$ at room temperature for 30 mins that are depicted in Figure 5.3 where chemisorbed Na$^+$ and SO$_4^{2-}$ are formed over the surface of the anodically fabricated TiO$_2$ nanotubes.
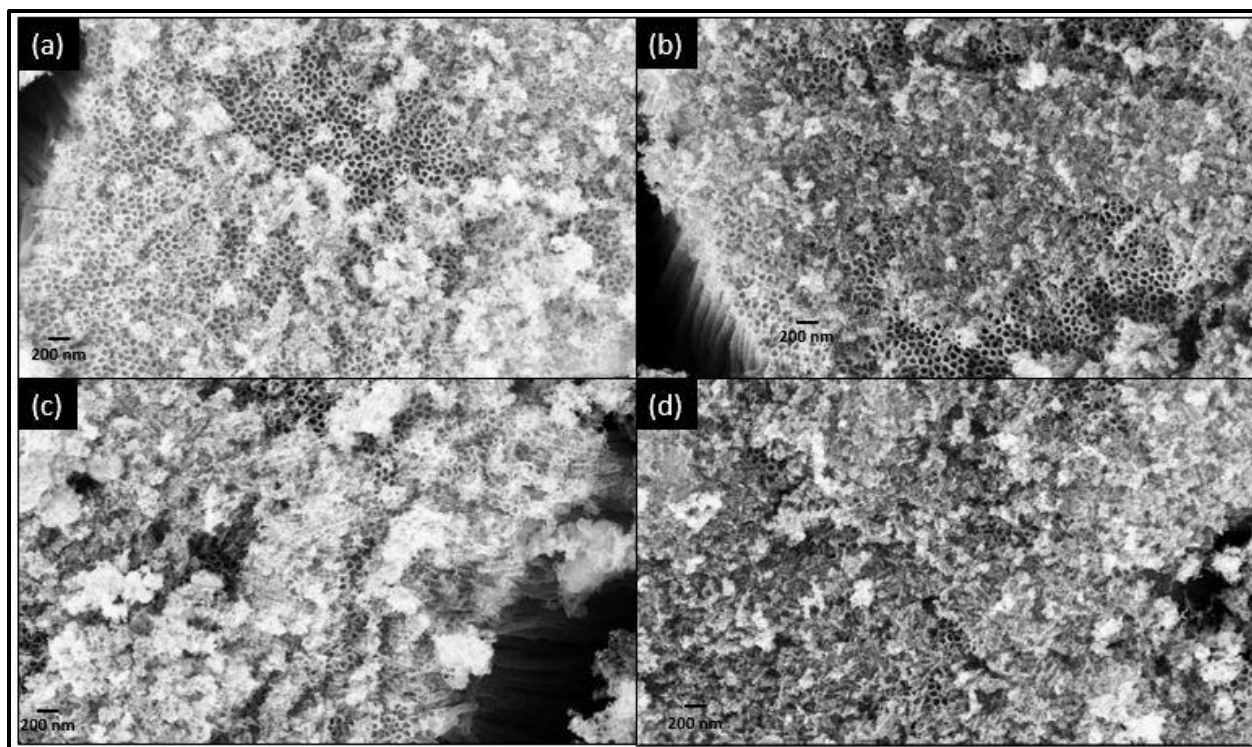
Figure 5.3: FESEM top-view images of the Na-modified TiO₂ nanotubes formed via soaking in (a) 0.05 M, (b) 0.1 M, (c) 0.2 M and (d) 0.4 M Na₂SO₄ for 30 min at room temperature.

X-ray diffraction (XRD) analysis was used in an interest to study the structural characteristics of the pure TiO_2 nanotubes as well as the sodium containing ones, all the patterns displayed in Figure 5.4 (panels a-c) clearly affirm the existence of tetragonal TiO_2 anatase which crystallizes within the $I4_1$ space group; lattice parameters a=b=3.78354 Å and c= 9.61464 Å; α=β=γ= 90° with the characteristic peaks of 25.2°, 37.6°, 47.3°, 53.8° and 54.8° related to the (101), (004) (200) (105) (211) facets respectively [4]. It should be noted that the peaks present at $2\theta \cong 40°$ and 52° are commonly attributed to the Ti substrate as earlier declared by [5]. The XRD patterns proved that no Na-Ti-O metal oxide crystal phase was present which demonstrates that the alkali metal only modified the surface of TiO_2 instead of being doped inside its crystal structure with no additional peaks observed as previously revealed by [6,7] who obtained analogous XRD diffractograms. It is also important to indicate that no significant shift in the diffraction peaks of the pure TiO_2 either towards higher or lower 2θ values were observed upon Na modification, which could be attributed to the low amount of Na in the composite. The structure of the prepared Na-modified TiO_2 nanotubes obtained at 80°C are mostly alike, with only single phase of anatase TiO_2 and no additional impurity peaks recognized. These observations agree very well with the FESEM results obtained above.
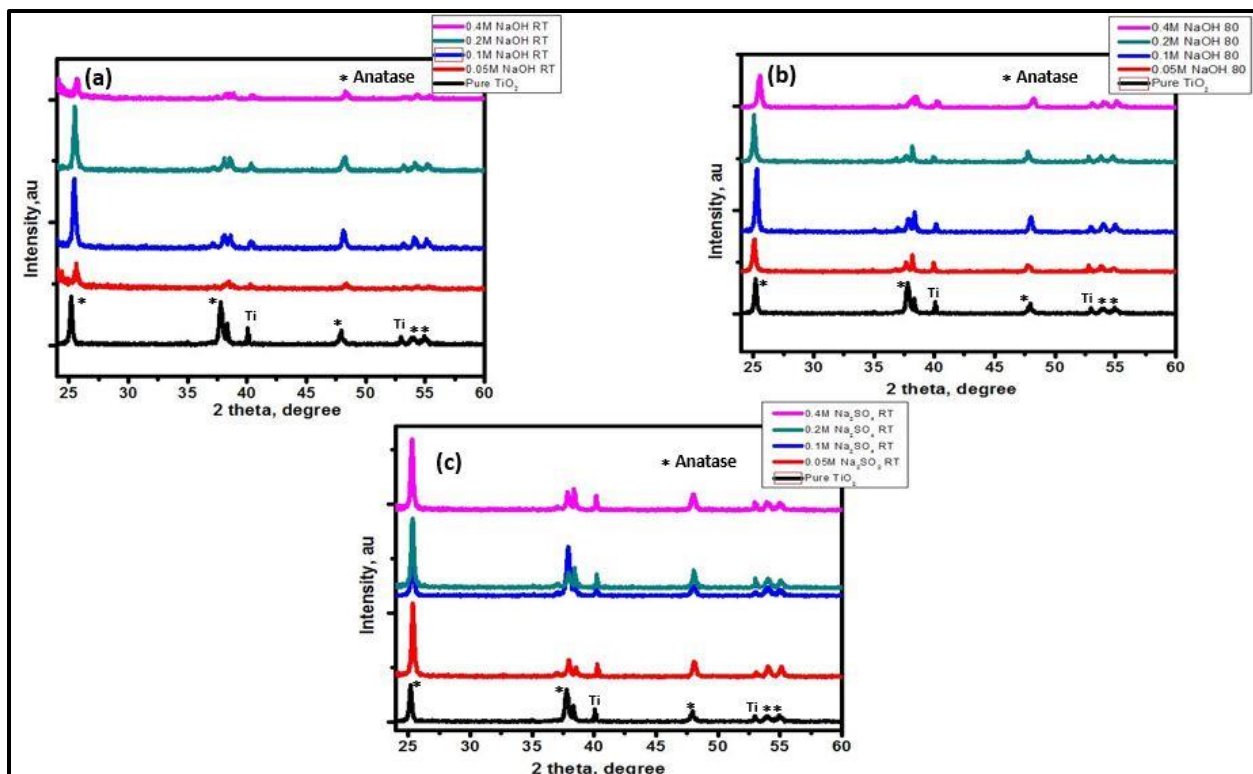
Figure 5.4: X-ray diffraction patterns of the annealed TiO₂ nanotubes (450°C, 4 h) and TiO₂ nanotubes immersed in 0.05 M, 0.1 M, 0.2 M, and 0.4 M of (a) NaOH at room temperature, (b) NaOH at 80 °C and (c) Na₂SO₄ at room temperature for 30 mins.

To further investigate the structural properties, Raman-scattering is another useful approach to explore the crystallinity as well as the vibrational characteristics of the materials since the Raman signals are highly responsive to any defects or noticeable change in the crystal structure. The phase components depicted in Figure 5.5 (panels a-c) shows that the fabricated samples have four Raman active modes (A_{1g}, B_{1g}, $2E_g$) with four significant peaks at 145 cm^{-1} (E_g), 394 cm^{-1} (B_{1g}), 514 cm^{-1} (A_{1g}) , 634 cm^{-1} (E_g) that are assigned to anatase TiO₂ [8] without any extra peaks detected to other titanate structures. Additionally, it is apparent that no peak broadening takes place as the amount of Na$^+$ is increased, illustrating no structural changes in the crystal lattice of TiO₂ [9]. This allows us to interpret that the alkali ions are widely dispersed on top of the crystal surface within the framework Ti-O-Ti [6,7] that is by way of explanation in good agreement with the XRD data.
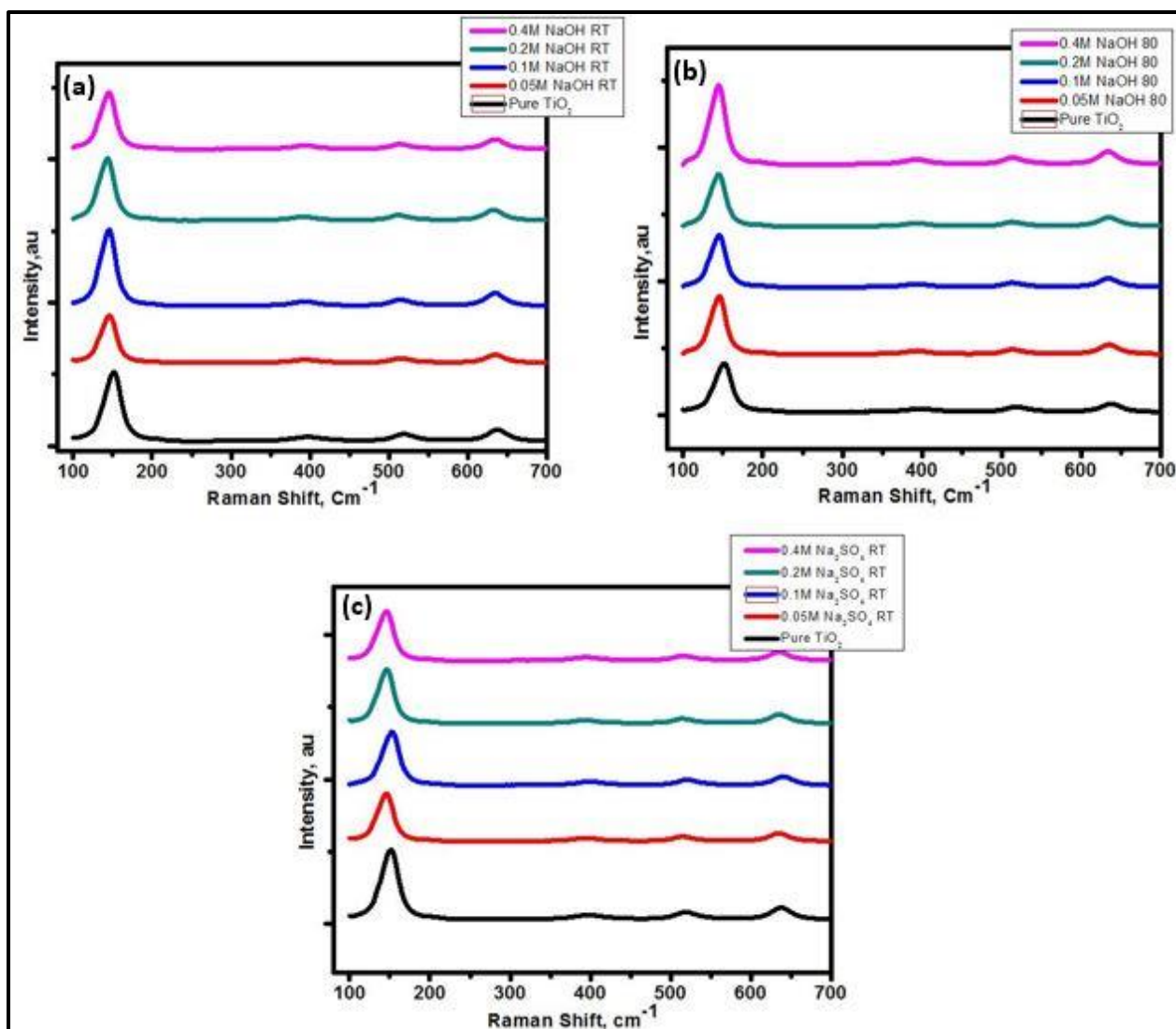
Figure 5.5: Raman spectra of the annealed TiO₂ nanotubes (450°C, 4 h) and TiO₂ nanotubes immersed in 0.05 M, 0.1 M, 0.2 M, and 0.4 M of (a) NaOH at room temperature, (b) NaOH at 80 °C and (c) Na₂SO₄ at room temperature for 30 mins.

5.2 Optical and Photoelectrochemical Characterization

To investigate the optical characteristics of the fabricated photoelectrodes, ultraviolet-visible diffuse reflectance spectroscopy (UV-vis DRS) has been utilized to probe the electronic structure of the sodium free as well as the sodium containing nanotube arrays. The fraction of the visible light absorbed by the Na modified TiO_2 nanotubes was not our intended target, however, shifting the absorption edge towards higher wavelength regions was the primary concern. Figure 5.6 (panels a-d) demonstrates the alteration of the DRS UV- vis spectra of both the unmodified and the surface modified TiO_2 nanotubes. The band gap of titania can be predicted by the intersection of the straight line from the absorption edge to the wavelength axis [10]. According to this approach, the band gap (E_g) for all the fabricated samples are indexed in table 5.1. It is observed that all the Na-containing samples exhibited almost similar absorption profiles with respect to that of the Na-free sample. The optical band edge of the pristine TiO_2 was predicted to

be approximately at 397.216 nm which relates to a band gap of 3.1217 eV whereas some of the surface modified samples exhibit minor shift in the optical band edge towards higher wavelengths. The red shift can be on one hand attributed to improved crystallinity in compliance with the literature [11]. On the other hand, it could also be originating from mid gap states that could either up-shift the valence band or down-shift the conduction band yielding visible light absorption properties [12]. Another possible approach that could attain a relatively narrowed band gap is the existence of a disordered layer on the nanocrystal surface, this effect would not induce a significant change in the band gap, nevertheless, it would induce conduction band tail states emerging from the disorder that exists below the conduction band minimum. This renders regions within the band where charge carriers can be trapped hence promote the charge transport efficiency by minimizing the recombination between the excited electrons and holes and consequently improve the light-driven photocatalytic performance [13,14]. While the observation of a slender blue shift in other modified TiO_2 nanotubes does not have an obvious interpretation so far, some reports have a plausible explanation to relate the shift towards lower wavelengths regions with higher band energies in TiO_2 to the quantum size effect [15,16] while others attributed it to the procedures of material preparation and crystal structure [17]. In most cases, adequate understanding of this behavior needs further investigation [18]. The optical properties investigation confirms the results obtained from the XRD and Raman analyses.
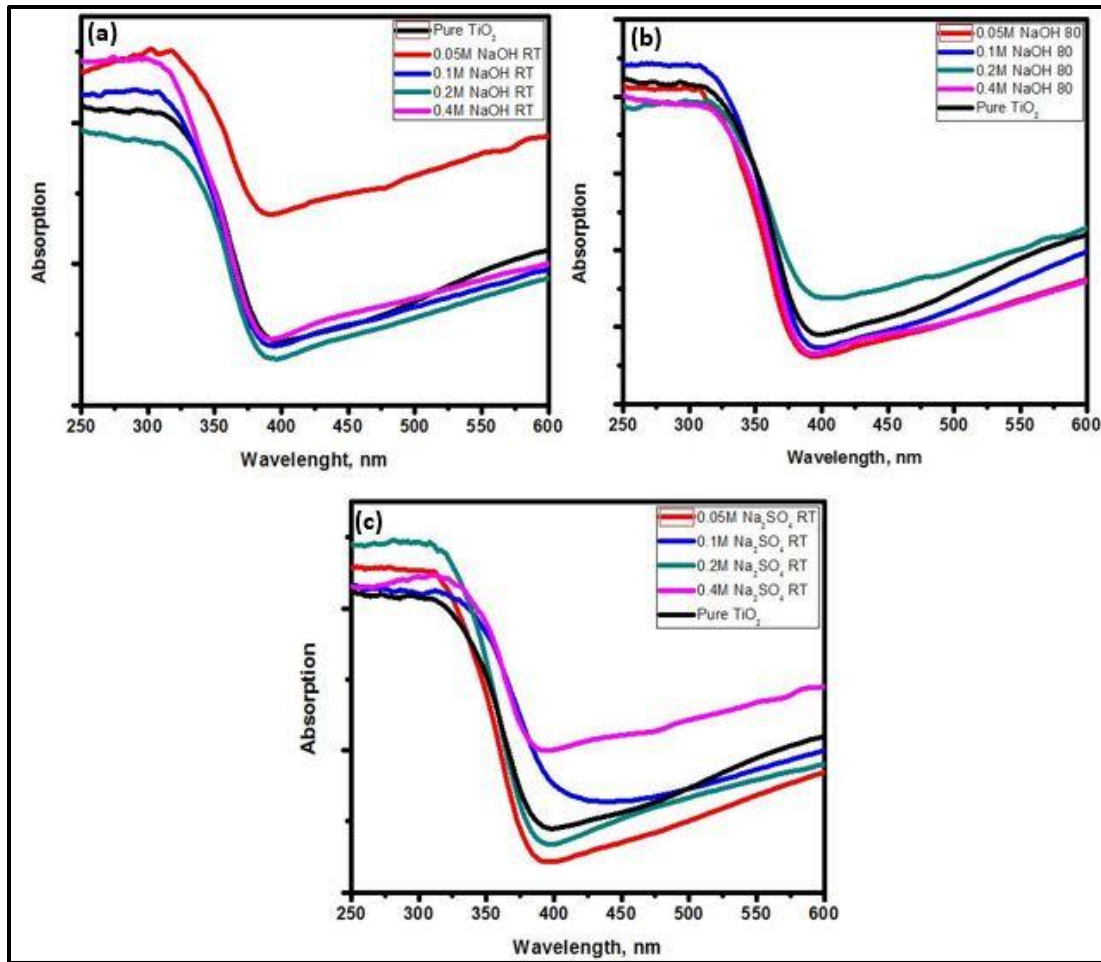
Figure 5.6: The absorption spectra of the annealed TiO₂ nanotubes and TiO₂ nanotubes immersed in 0.05 M, 0.1 M, 0.2 M, and 0.4 M of (a) NaOH at room temperature, (b) NaOH at 80 °C and (c) Na₂SO₄ at room temperature for 30 mins.

Table 5.1: Absorption edges and energy gaps for pure TiO₂ and Na-modified TiO₂ samples.

Sample	Absorption edge (nm)	Band gap (E_g; eV)
Pristine TiO_2	~ 397.2164	~ 3.1217
0.05 M NaOH RT	~440.2749	~2.8164
0.1 M NaOH RT	393.60824	~3.1503
0.2 M NaOH RT	~390	~3.1794
0.4 M NaOH RT	~392.8865	~3.1561
0.05 M NaOH 80°C	~387.8350	~3.1972
0.1 M NaOH 80°C	~395.0515	~3.13883
0.2 M NaOH 80°C	~414.4558	~2.9918
0.4 M NaOH 80°C	~390.7216	~3.1736
0.05 M Na_2SO_4 RT	~387.0904	~3.20338
0.1 M Na_2SO_4 RT	~424.753	~2.91934
0.2 M Na_2SO_4 RT	~394.4215	~3.1438
0.4 M Na_2SO_4 RT	~412.4742	~3.00624

With the existence of disordered-engineered TiO_2 nanostructure as confirmed from the above analyses, an enhancement in the solar water splitting photocurrent is predicted. The photoactive performance for the electrolysis of water utilizing the developed photoelectrodes has been appraised in 0.05M $Ba(OH)_2$ electrolyte solution adopting the ordinary three-electrode electrochemical cell. Dark currents demonstrate nearly insignificant values in the range of 0.1 $\mu A/cm^2$. At the time of illumination (AM 1.5 G), Figure 5.7 shows a remarkable enhancement in the photocurrent spectral response with increasing applied bias for the bare TiO_2 nanotubes as well as the surface modified ones. This improvement in the photocurrent signifies that the currents under illuminated conditions are typically produced by the incident photons without the contribution of the dark current which represents favorable electron transfer ability for the fabricated electrodes. The highest maintained photocurrent density for pristine TiO_2 was 0.1821 mA cm^{-2} in accordance with literature [19,20]. Nonetheless, the photocurrent response improved remarkably upon the process of NaOH-soaking of TiO_2 nanotubes reaching 0.629 mA cm^{-2} for the 0.4 M surface modified electrode at room temperature. A possible approach for the enhancement of the photocurrent is that TiO_2 will endure an immense level of hydroxylation when it is soaked in NaOH and the presence of the hydroxide ions on the surface can act as hole acceptors that play a crucial role to trap the valence band holes supplying hydroxyl radicals which can promote the water photooxidation reaction and minimize the carriers' recombination rate [7]. This is in consistency with the experimental results of Yamaguti et al. [21] which indicates an enhanced photoelectrochemical performance for TiO_2 in alkaline media.

From an attentive observation of Figure 5.7a it was realized that the onset potential of the surface modified samples is becoming more negative with increasing the Na^+ adsorption reaching -1.2033 $V_{Ag/AgCl}$ for the 0.4 M modified sample with respect to -1.1698 $V_{Ag/AgCl}$ for the pristine TiO_2. The open-circuit voltage indicates the input of light towards the least possible external bias required for the water splitting reaction [22]. This means that all the Na^+ containing samples require less external bias for the water oxidation reaction to take place in preference to TiO_2. This may be attributed to the considerable alteration in the surface charge that would impact the band bending properties and in return affect the charge separation kinetics. The energy bands of the sodium containing titania photocatalysts are pinned at electrochemical potentials that are marginally more positive than that of the sodium free counterpart and hence the band bending becomes less steep as the sodium is adsorbed on the surface, reducing the external bias required for the photoelectrode to generate hydrogen [23].

Figure 5.7b displays the J-V curves for the TiO_2 samples treated in aqueous NaOH solution at 80°C. Likewise the behavior at room temperature, the plot shows a cathodic shift in the open-circuit potentials for all the modified samples with respect to the pristine TiO_2. This is a consequence of the adsorbed sodium on the surface causing a reduction in the slope of the band bending. With a closer view at Figure 5.7b, it is obvious that the enhancement in the photocurrent density for all the surface modified nanotubes reached an optimum value of 0.647 mA cm^{-2} for the 0.1 M modified sample. However, the samples modified at higher concentrations of 0.2 and 0.4 M exhibit a reduction in the photocurrent to 0.2032 mA cm^{-2} and 0.316 mA cm^{-2} respectively. This behavior could be ascribed to the high susceptibility of the surface to be etched away at elevated temperatures. That is, more elemental Ti is being removed from the bulk TiO_2 leading to decrease the surface area of the nanotubes available to interact with the electrolyte as well as the incident photons and hence reduce their contribution to the photoelectrochemical

reaction [24]. This signifies that the optimized loading of NaOH (0.1 M) at 80 °C maintains an adequate mediation between the amount of holes to be trapped and the available surface area of the catalyst for hydrogen production.
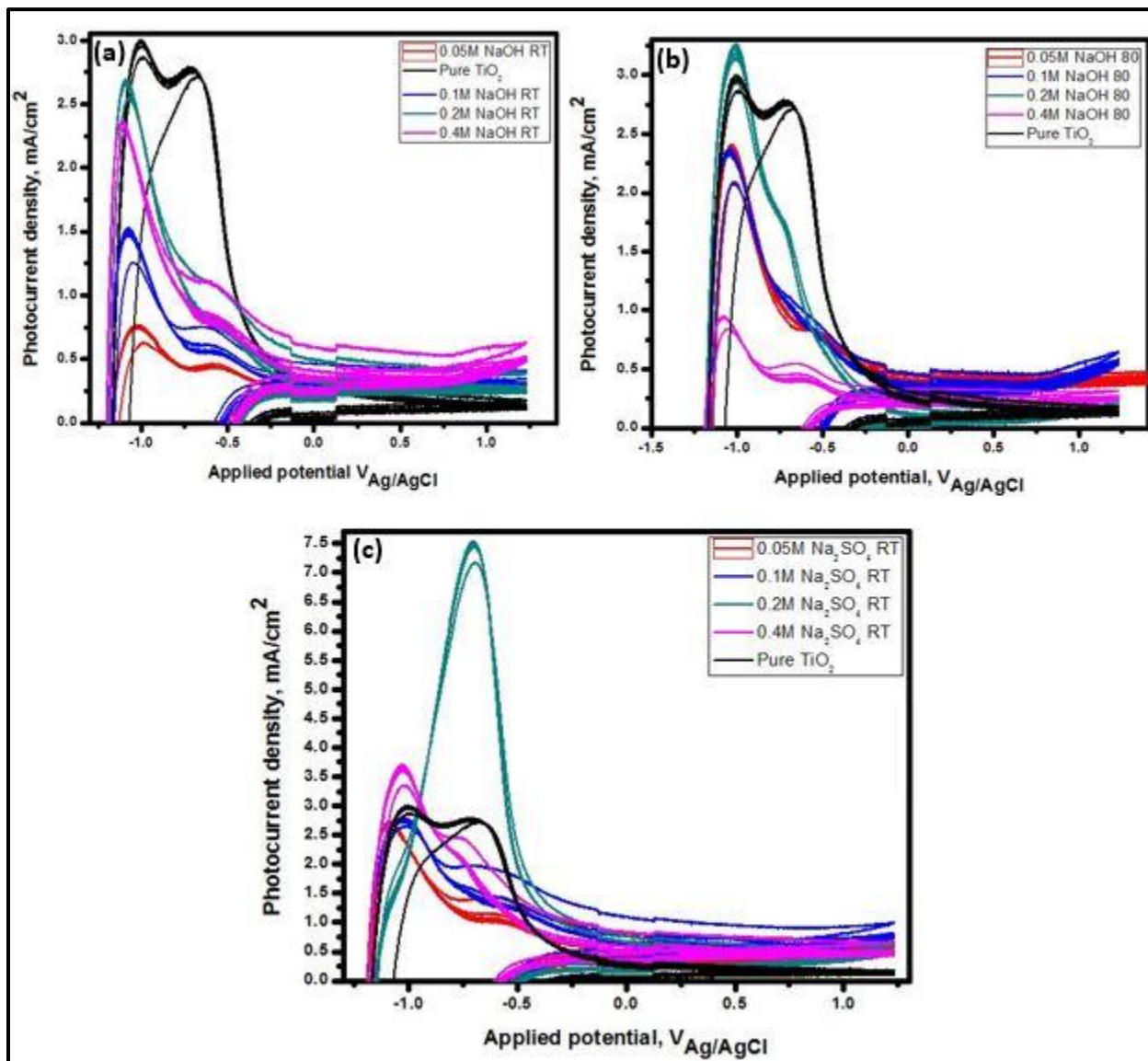
Figure 5.7: Photocurrent density against applied potential in 0.05 M Ba(OH)$_2$ electrolyte under AM 1.5G for pure TiO$_2$ nanotubes as well as TiO$_2$ nanotubes immersed in 0.05 M, 0.1 M, 0.2 M, and 0.4 M of (a) NaOH at room temperature, (b) NaOH at 80 °C and (c) Na$_2$SO$_4$ at room temperature, for 30 mins.

We have additionally examined the effect of using a different counter ion (SO$_4^{2-}$) to the Na$^+$ to alter the surface of TiO$_2$ and compare the outcomes obtained from NaOH modifications. Distinctively from the OH$^-$ modification, as it was apparently deduced that the presence of the hydroxide ions play a crucial role in trapping the photoexcited holes hence suppress the recombination rate and promote the water oxidation reaction, the improved photocurrent behavior of TiO$_2$ upon SO$_4^{2-}$ alteration mostly relies on the negative electrostatic field formed on the surface layers which will considerably increase the lifetime of the photoexcited charges and accordingly enhance the activity for PEC water splitting [25, 26]. Figure 5.7c shows the J-V

plots for the Na$_2$SO$_4$ treated TiO$_2$ nanotubes at room temperature illustrating an enhancement in the solar photocurrent for all the modified photoelectrodes with an optimum value of 0.9928 mA cm^{-2} for the 0.1 M treated sample which is almost five folds that of the pristine TiO$_2$. It is interesting to observe that the photocurrent responses at lower concentrations (0.05 and 0.1 M) are superior to those at higher concentrations (0.2 and 0.4 M) which indicates more favorable electric field properties that enhance the separation probability of the charge carriers. We should bear in mind that all the values are still higher than that of the unmodified TiO$_2$ [27]. Charts 5.1-5.3 provide all the short-circuit current and open-circuit potential values for all the fabricated samples with respect to the pristine TiO$_2$.
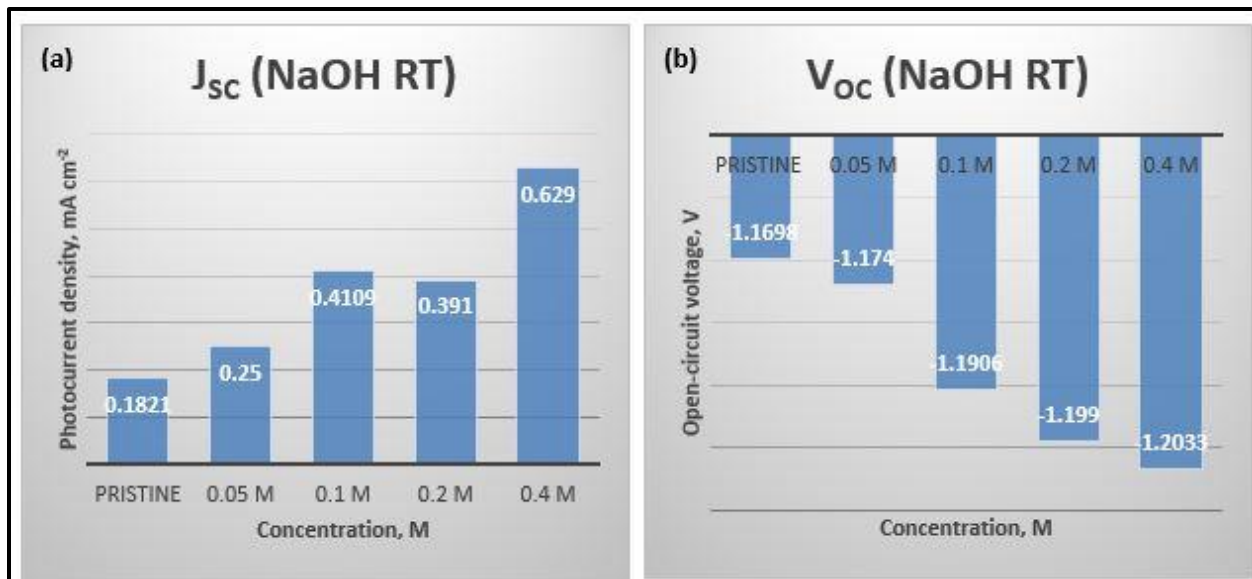
Chart 5.1: (a) J$_{SC}$ and (b) V$_{OC}$ of pure TiO$_2$ nanotubes as well as TiO$_2$ nanotubes immersed in 0.05, 0.1, 0.2 and 0.4 M NaOH at room temperature for 30 mins.
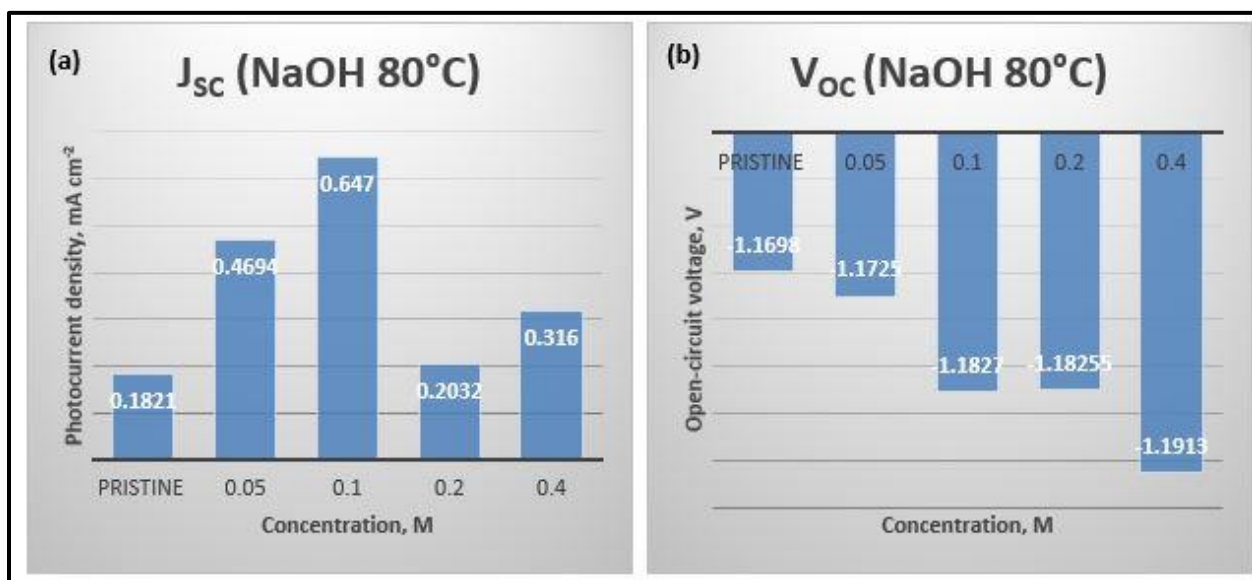
Chart 5.2: (a) J$_{SC}$ and (b) V$_{OC}$ of pure TiO$_2$ nanotubes as well as TiO$_2$ nanotubes immersed in 0.05, 0.1, 0.2 and 0.4 M NaOH at 80 °C for 30 mins.

81
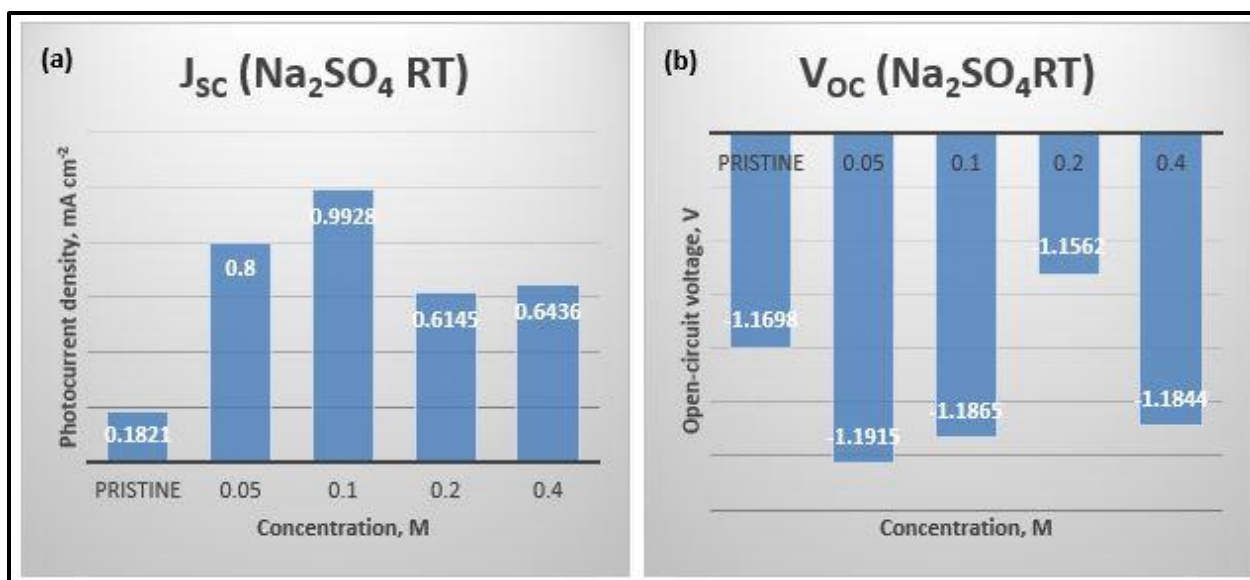
Chart 5.3: (a) J_{SC} and (b) V_{OC} of pure TiO₂ nanotubes as well as TiO₂ nanotubes immersed in 0.05, 0.1, 0.2 and 0.4 M Na₂SO₄ at room temperature for 30 mins.

Considering the above results, it could be speculated that the enhanced photoactive performance was mainly related to the surface modifications that suppress the recombination process and prolong the life time of the charge carriers when compared with unmodified surface as well as producing cathodic shift in the V_{OC} which indicates low external bias required to produce H_2. Subsequently, additional analyses were necessary to verify the improvement in the PEC process kinetics.

Electrochemical impedance spectroscopy (EIS) was carried out to describe the charge transfer process in the PEC cell and to affirm the contribution of the improved charge carriers' dynamics to the enhanced performance. Figure 5.8 displays the Nyquist plots at zero voltage for the unmodified and surface modified electrodes. The plot displays set of points each of which expresses the magnitude and direction of the impedance vector at a certain frequency where the X-axis is the real part (resistive behavior of the cell) and the Y-axis is the imaginary part (capacitive behavior of the cell). The Nyquist plot has been usually elucidated to represent the low frequency data on the right side of the curve and the higher frequency ones on the left side since the impedance usually drops when the frequency increases [28].
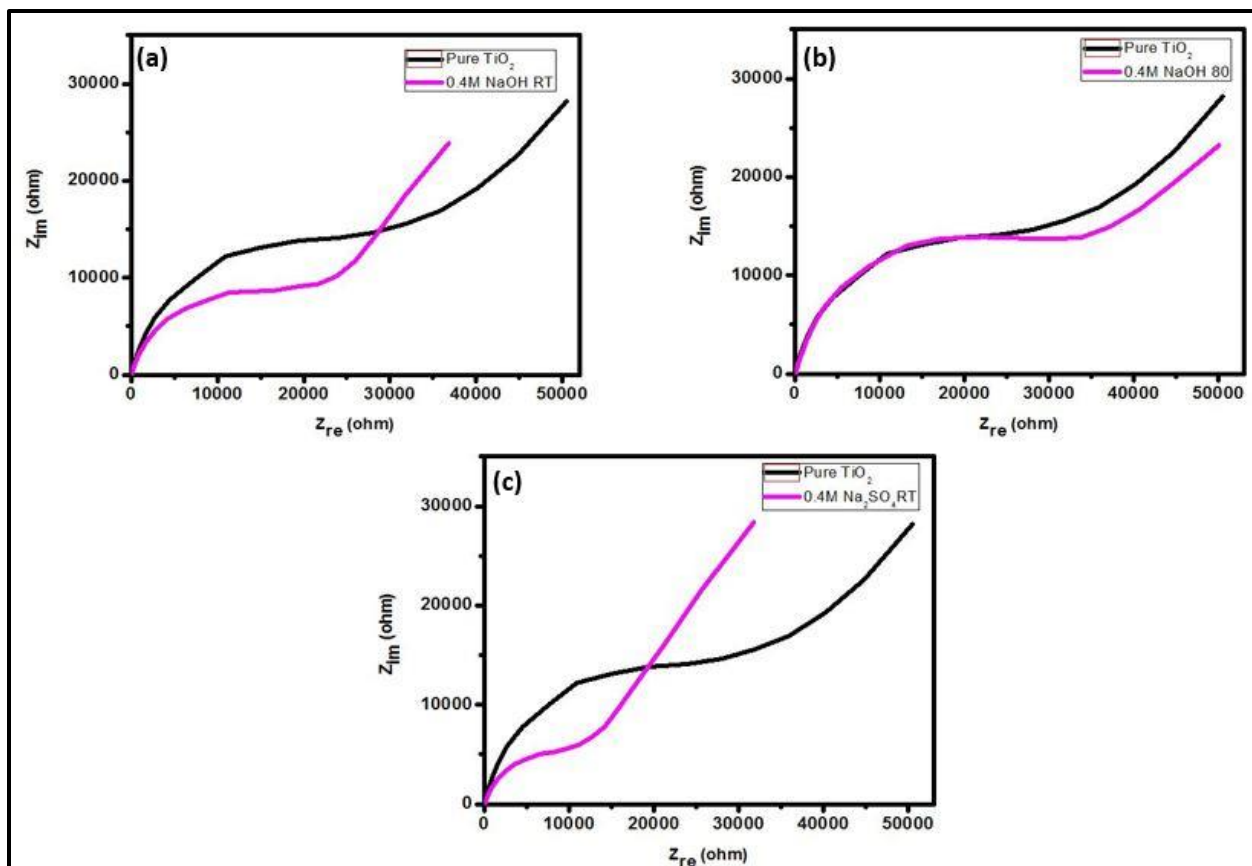
Figure 5.8: Illuminated Nyquist plots of pure TiO₂ nanotubes and 0.4 M soaked TiO₂ nanotubes in (a) NaOH at room temperature, (b) NaOH at 80 °C and (c) Na₂SO₄ at room temperature for 30 mins.

The perception of the EIS plot counts on the electrical components (resistance, capacitance and Warburg impedance) used to describe physical processes affecting the photoanode's performance like electrolyte resistance, charge transfer resistance for the electrochemical reaction taking place at the electrode's surface, double layer capacitance present at the junction between the working electrode and the electrolyte solution (mainly caused by the buildup of charges at the electrode surface) and mass transfer resistance due to the diffusion of the reactants (i.e; electroactive species towards the electrode). That being said, analyzing all probable faradic and non-faradic processes that can take place over the photoanode's surface [29, 30].

In a typical PEC cell, the working electrode at the high frequency region where the mass transfer effect is insignificant can be modeled by the simple Randles circuit as described below (Figure 5.9 a). Where R1 is the solution resistance, C is the capacitance of the double layer and R2 is the charge transfer resistance however, at low frequencies we should account for the mass-transfer resistance that is displayed by a diagonal line with a slope of 0.5 and expressed by a Warburg circuit element making the whole physical model appear as in Figure 5.9b [31].

The Nyquist plot of the Randles cell is usually a semicircle where the frequency at 90° represents 1/RC and the electrolyte resistance can be obtained by the intercept of the X-axis at the high frequency range. Whereas the other intercept at the low frequency range represents the totality of both charge-transfer and solution resistances (the diameter of the semicircle therefore

represents the charge-transfer resistance) as depicted in Fig 5.9c [29]. From Fig 5.8 it's obvious that the impedance behavior of the fabricated samples endures an oppressed semicircle at the high frequency range and an inclined line at the low frequency one. The semicircle of the high frequency range is ascribed to the charge-transfer resistance as well as the double-layer capacitance of the photoanode, whereas the inclined line at the low frequency range is ascribed to the diffusion of the electroactive species within the bulk of the photoelectrode represented by the Warburg diffusion. The EIS studies indicate that the obtained spectra are due to mixed kinetic and diffusive processes.
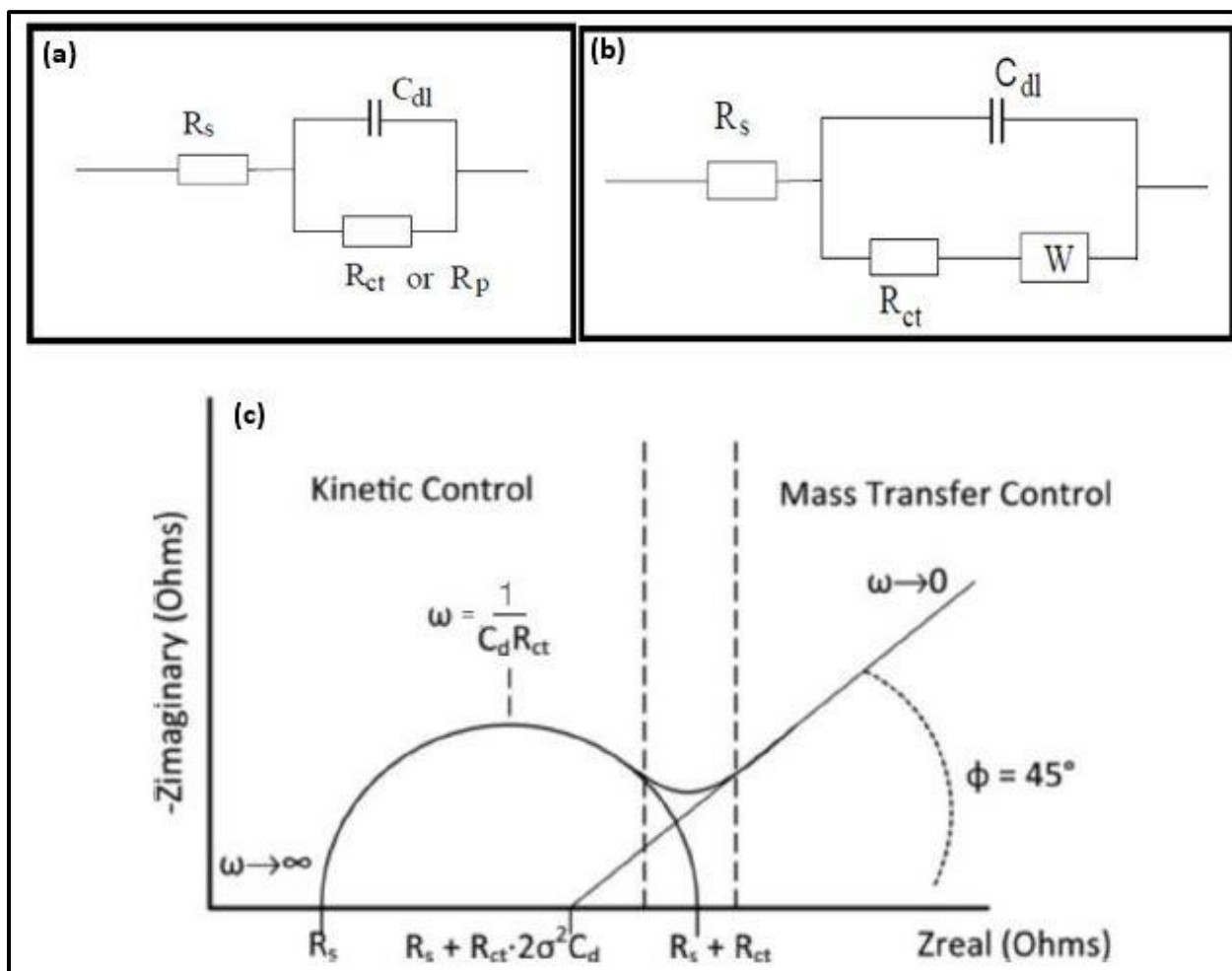
Figure 5.9: (a) Schematic diagram of the simple Randles cell, (b) Schematic diagram of Randless cell with Warburg impedance and (c) Nyquist impedance for mixed kinetic and mass transfer control [29,31].

Table 5.3 displays the values of the circuit elements to which the pristine sample as well as the 0.4 M NaOH modified at room temperature samples were fitted using the EC-Lab software. An identical approach could be followed for other samples. Figure 5.10 displays both the fitted and empirical curves for the two samples. It is noticed, due to the higher curvature of the Nyquist diagram, that the pristine sample possesses a higher charge-transfer resistance and double layer capacitance with respect to the modified one. The analysis points out that the photogenerated charge carriers of the pure TiO_2 sample exhibit more hindrance to reach the semiconductor/electrolyte interface where the water splitting reaction takes place and thus many charges have the probability to recombine before carrying out the reaction. The improved

photoelectrochemical performance of the surface modified electrodes can be attributed to the slower recombination rate considering the low polarization resistance and double layer capacitance providing superior separation and mobility for the e^-/h^+ pairs that is in agreement with the previously reported photoelectrochemical activity tests.

Table 5.2: Extracted circuit elements for pure TiO₂ and 0.4 M NaOH modified TiO₂ at room temperature

Circuit element	Extracted values for Pure TiO$_2$	Extracted values for 0.4M NaOH RT
R_{ct}	27 653 Ohm	17 362 Ohm
Q_{dl}	2.707e-6 F	2.333e-6 F
W	16 611 Ohm.s^-1/2	13 813 Ohm.s^-1/2
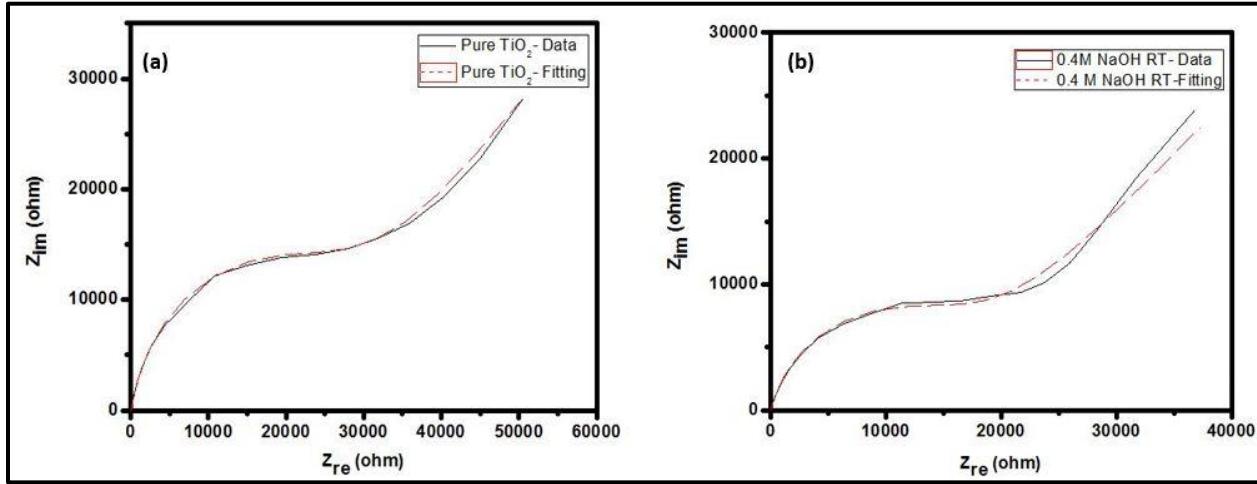
Figure 5.10: Empirical curve (solid) against fitted curve (dotted) of (a) pure TiO₂ and (b) 0.4 M NaOH modified TiO₂ at room temperature.

Concerning the phenomenon that the surface modified TiO$_2$ nanotubes possess superlative photoelectrochemical properties relative to the pristine electrode, it is recognized that a key factor is the change in the position of the flat band potential (E_{fb}). Relying on the Mott-Schottky principle, E_{fb} can be estimated by the extrapolation of the tangent of the plot of the square of the space charge capacitance with the applied potential through the equation 5.1

$$\frac{1}{C^2} = \frac{2}{\varepsilon \varepsilon_0 e\, N_d}(E - E_{fb} - \frac{KT}{e})$$ (5.1)

Where C is space charge layer capacitance (F cm^{-2}), e is the electronic charge ($1.6*10^{-19}$ C), ε_0 permittivity of vacuum ($8.86*10^{-14}$ F cm^{-1}), ε is the dielectric constant of the semiconductor (ε= 48 for anatase TiO$_2$), N_d carriers' concentration, E is the applied voltage, E_{fb} is the flat band potential, T is the temperature in Kelvin and K is Boltzmann's constant ($1.38*10^{-23}$ J K^{-1}) [32].

The discrepancy in the behavior of the alkali-modified nanotubes with respect to that of the pristine, endorse direct the contribution of Na to the water splitting reaction. Figure 5.11 (panels a-e) illustrates the Mott-Schottky plots of $1/C^2$ as a function of the applied bias where the existence of the positive slop affirms an n-type behavior for the fabricated samples. It was found that the value of E_{fb} for the unmodified TiO$_2$ is approximately determined at -0.583837 V$_{Ag/AgCl}$

in agreement with literature [33], whereas, the values for the 0.1, 0.2 and 0.4 M NaOH modified electrodes at room temperature are about -0.70911 $V_{Ag/AgCl}$, -0.62776 $V_{Ag/AgCl}$, -0.62230 $V_{Ag/AgCl}$ respectively. This indicates that E_{fb} of the treated samples has shifted from 0.03847 V to 0.12528 V negatively, which suggests that a higher fermi level could be accomplished upon Na modification leading to an enhancement in the V_{oc} of the surface modified TiO_2 photoelectrodes. Furthermore, the values for the NaOH modified samples at 80°C also exhibit a negative shift in the E_{fb} where the 0.1, 0.2 and 0.4 M treated samples maintain -0.7419 $V_{Ag/AgCl}$,-0.78561 $V_{Ag/AgCl}$, -1.00841 $V_{Ag/AgCl}$ respectively. The results signify a decline in the steepness of the band bending and hence promotion of the photoexcited charge carriers' separation and transfer, justifying the enhancement in the open circuit voltage (V_{oc}) obtained previously from the J-V characteristics. It is also worth noting that when the external bias becomes more negative (that is near that of the flat band) the energy gap becomes more confined and hence excess electrons will pile up at the electrode's interface. This behavior will collect more charge for the electrical double layer capability and larger current densities will be attained. The previous analysis will offer an explanation as to why the shape of the J-V curve is higher at more negative voltages with respect to positive voltages [34].
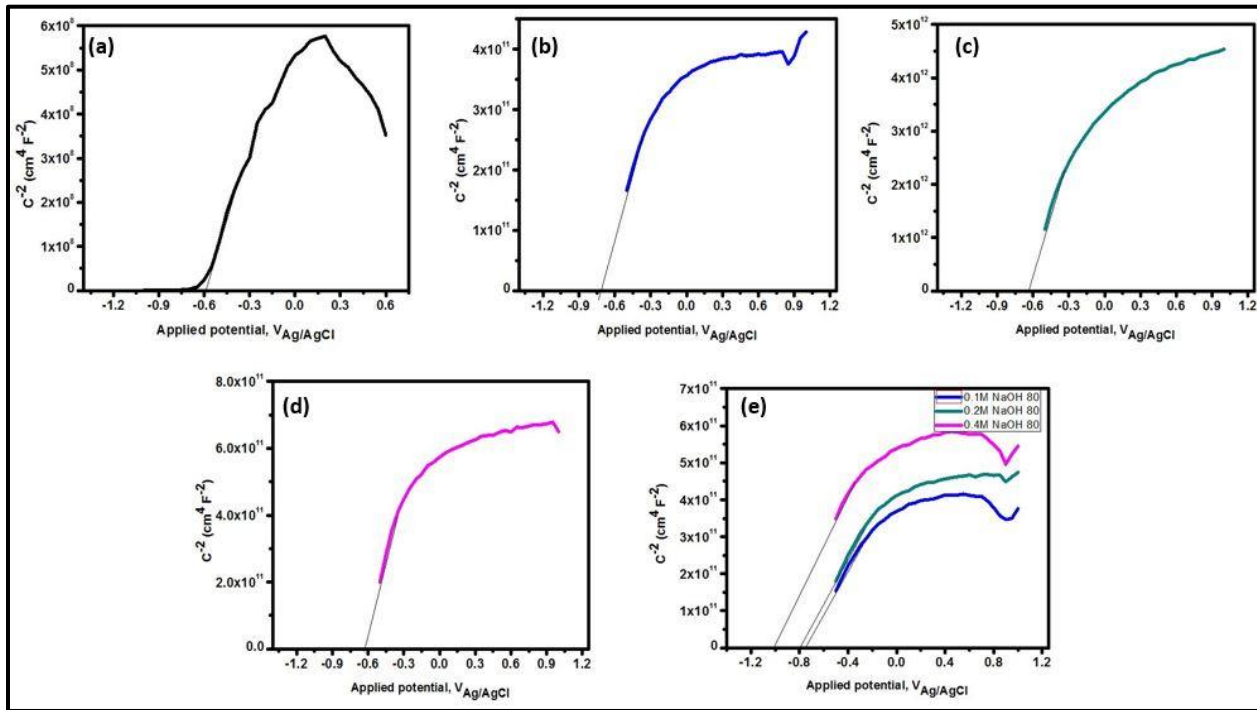
Figure 5.11: Illuminated Mott-Schotky plots of (a) Pure TiO₂ nanotubes, TiO₂ nanotubes immersed in (b) 0.1 M (c) 0.2 M, (d) 0.4 M NaOH at room temperature and TiO₂ nanotubes immersed in (e) 0.1 M, 0.2 M and 0.4 M NaOH at 80°C.

5.3 DFT Calculations

To have more insight on the optical and structural characteristics, we carried out density functional theory (DFT) calculations to examine the influence of Na modification on the density of states (DOS) and band structure of TiO_2 as described in Figure 5.12-14. Quantum Espresso software package was utilized in electronic structure calculations. Less than 0.0001 Ry/Bohr force was adjusted for attaining minimum energy configurations. Calculations were performed by a 3x3x3 Monkhorst-Pack k-point grid, with an energy cutoff of 45 Ry, using the generalized gradient approximation PBE functional [35].
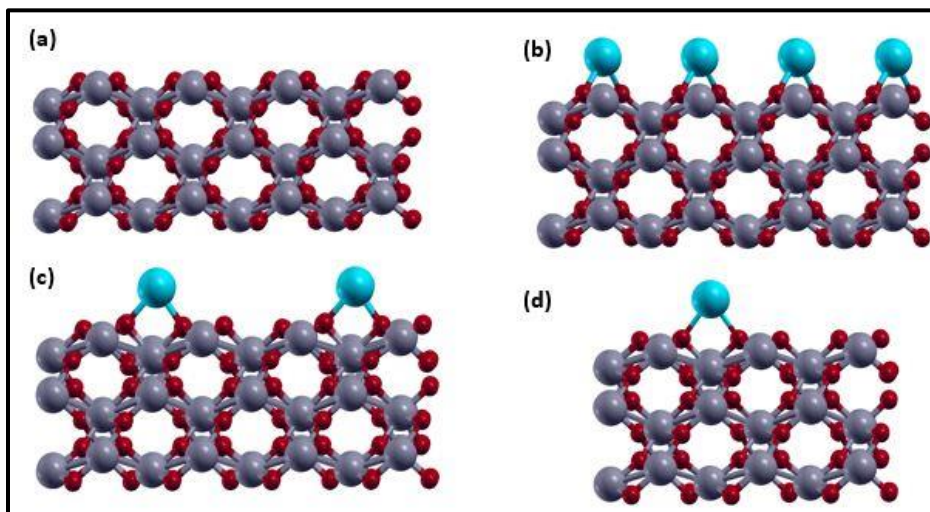
Figure 5.12: Crystal structure of (a) TiO_2, (b) $Ti_6O_{12}Na$, (c) $Ti_{24}O_{48}Na$ and (d) $Ti_{54}O_{108}Na$. (Grey, red and blue balls represent Ti, O and Na atoms respectively).

The Projective Density Of State (PDOS) showed a disorder in the TiO_2 structure upon the adsorption of Na leading to the existence of band tail states; an expansion within the conduction band minimum lowering it down. The sensitivity of the conduction band to the Na adsorption demonstrates the contribution of the Na states to the bottom of the conduction band, confirming that the conduction band tails is the main reason for the narrowing of the energy gap. The apparent discrepancy in the energy gap values predicted from the DRS UV-vis measurements and those calculated by the DFT are ascribed to the larger modification ratios utilized in the DFT calculations in comparison with those utilized empirically. However, the DFT shows the same trend as the DRS UV-vis measurements, highlighting that Na modifications can yield band gap narrowing in TiO_2. This provides new path-ways for further advancement and suggests new structures that can adhere more precisely with the empirical results.
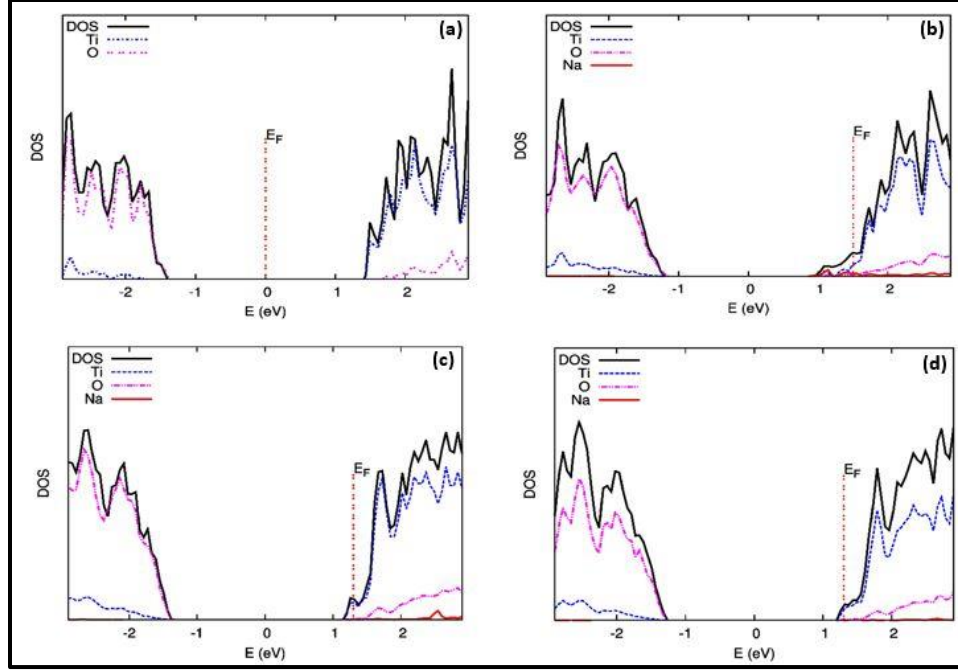
Figure 5.13: Projective Density Of States for (a) TiO_2, (b) $Ti_6O_{12}Na$, (c) $Ti_{24}O_{48}Na$ and (d) $Ti_{54}O_{108}Na$ structure.
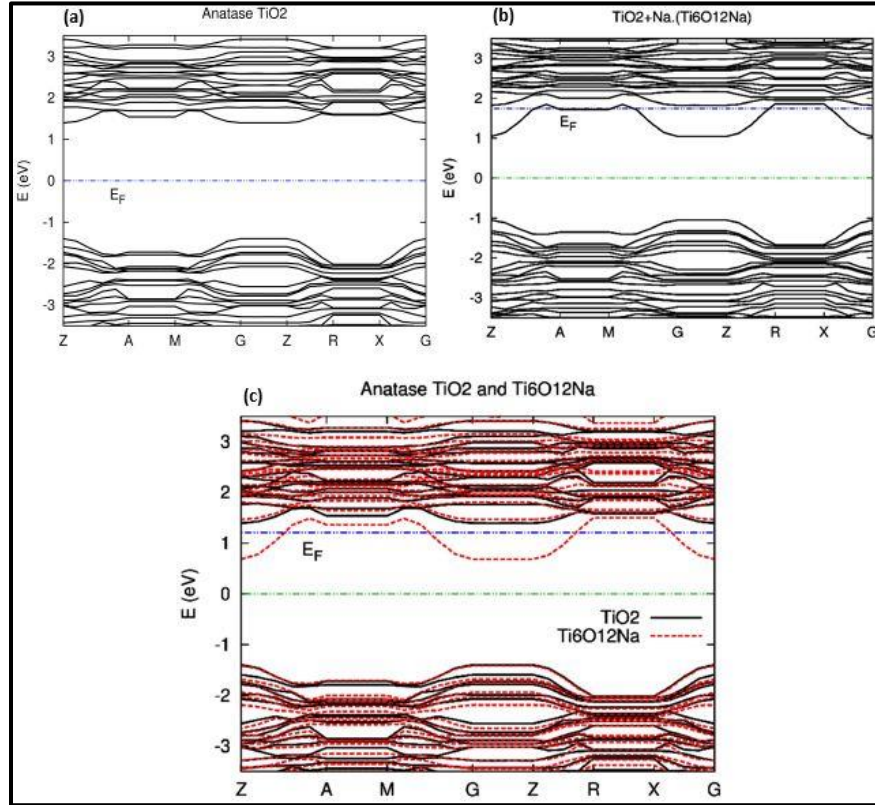
Figure 5.14: Corresponding band structure for the (a) Undoped TiO_2, (b) $Ti_6O_{12}Na$ and (c) Overlaid pure TiO_2 and $Ti_6O_{12}Na$.

In summary, the photoelectrochemical performance of Na-modified TiO_2 nanotube arrays formed via electrochemical oxidation of Ti followed by simple soaking treatment in aqueous solution of sodium salts was demonstrated. The morphological and structural properties verified the existence of a disordered layer on the top surface of the anodic nanotubes with no change in the characteristic peaks position and shape relative to the pristine TiO_2 which indicates that the existence of Na does not impact the crystal lattice of TiO_2 while it only modifies its surface. With the results of lacking long range order within the TiO_2 network, the optical properties confirmed the existence of conduction band tails causing a slight red shift in the onset of the absorption edge with respect to the unmodified TiO_2. Being utilized as a photocatalyst to promote the water splitting reaction, the surface modified samples showed an almost five fold enhancement in the solar photocurrent (0.9928 mA cm^{-2}) compared to that of the pristine one (0.1821 mA cm^{-2}) under (AM 1.5 G) which was related to the superior charge carriers' separation and mobility. This was asserted by the impedance measurements which prove that modified samples possess a lower charge transfer resistance as well as a double layer capacitance and hence exhibit better kinetics for the water splitting reaction. The treated samples also maintained a more negative open-circuit potential in comparison with the bare one which was attributed to the less steepness of the band bending reducing the external bias required to promote the reaction. This was also confirmed by the Mott-Schottky results which illustrate a negative shift in the flat band potential with respect to that of the pristine TiO_2.

References

1. K. Shankar, J. Basham, N. Allam, O. Varghese, G. Mor, X. Feng, M. Paulose, J. Seabold, K. Choi and C. Grimes, "Recent Advances in the Use of TiO_2 Nanotube and Nanowire Arrays for Oxidative Photoelectrochemistry", *The Journal of Physical Chemistry C*, vol. 113, no. 16, pp. 6327-6359, 2009.

2. N. Allam and M. El-Sayed, "Photoelectrochemical Water Oxidation Characteristics of Anodically Fabricated TiO_2 Nanotube Arrays: Structural and Optical Properties", *The Journal of Physical Chemistry C*, vol. 114, no. 27, pp. 12024-12029, 2010.

3. K. Shankar, G. Mor, H. Prakasam, S. Yoriya, M. Paulose, O. Varghese and C. Grimes, "Highly-ordered TiO_2 nanotube arrays up to 220 µm in length: use in water photoelectrolysis and dye-sensitized solar cells", *Nanotechnology*, vol. 18, no. 6, p. 065707, 2007.

4. C. Carlucci, F. Conciauro, B. Scremin, A. Antico, M. Muscogiuri, T. Sibillano, C. Giannini, E. Filippo, C. Lorusso, P. Congedo and G. Ciccarella, "Properties of Aluminosilicate Refractories with Synthesized Boron-Modified TiO_2 Nanocrystals", *Nanomaterials and Nanotechnology*, vol. 5, p. 8, 2015.

5. S. Chaguetmi, F. Mammeri, S. Nowak, P. Decorse, H. Lecoq, M. Gaceur, J. B. Naceur, S. Achour, R. Chtourou, and S. Ammar, "Photocatalytic activity of TiO_2 nanofibers sensitized with ZnS quantum dots," *RSC Advances*, vol. 3, no. 8, pp. 2572–2580, 2013.

6. L. Yu, Q. Wang, Q. Zhi, K. Dong, Q. Xue and Z. Yaping, "Photoelectrochemical Properties of Alkali Metal Doped TiO_2 Nano-Honeycomb Film", *Energy and Environment Focus*, vol. 4, no. 3, pp. 191-195, 2015.

7. X. Meng, S. Ouyang, T. Kako, P. Li, Q. Yu, T. Wang and J. Ye, "Photocatalytic CO_2 conversion over alkali modified TiO_2 without loading noble metal cocatalyst", *Chem. Commun.*, vol. 50, no. 78, pp. 11517-11519, 2014.

8. Y. Yu, J. Yu, J. Yu, Y. Kwok, Y. Che, J. Zhao, L. Ding, W. Ge and P. Wong, "Enhancement of photocatalytic activity of mesoporous TiO_2 by using carbon nanotubes", *Applied Catalysis A: General*, vol. 289, no. 2, pp. 186-196, 2005.

9. M. Wang, J. Ioccozia, L. Sun, C. Lin and Z. Lin, "Inorganic-modified semiconductor TiO_2 nanotube arrays for photocatalysis", *Energy & Environmental Science*, vol. 7, no. 7, pp. 2182-2202, 2014.

10. T. López, J. Hernandez-Ventura, R. Gómez, F. Tzompantzi, E. Sánchez, X. Bokhimi and A. García, "Photodecomposition of 2,4-dinitroaniline on Li/TiO$_2$ and Rb/TiO$_2$ nanocrystallite sol–gel derived catalysts", *Journal of Molecular Catalysis A: Chemical*, vol. 167, no. 1-2, pp. 101-107, 2001.

11. N. Allam, K. Shankar and C. Grimes, "A General Method for the Anodic Formation of Crystalline Metal Oxide Nanotube Arrays without the Use of Thermal Annealing", *Advanced Materials*, vol. 20, no. 20, pp. 3942-3946, 2008.

12. C. Fan, C. Chen, J. Wang, X. Fu, Z. Ren, G. Qian and Z. Wang, "Enhanced photocatalytic activity of hydroxylated and N-doped anatase derived from amorphous hydrate", *J. Mater. Chem. A*, vol. 2, no. 38, pp. 16242-16249, 2014.

13. X. Chen, L. Liu, P. Yu and S. Mao, "Increasing Solar Absorption for Photocatalysis with Black Hydrogenated Titanium Dioxide Nanocrystals", *Science*, vol. 331, no. 6018, pp. 746-750, 2011.

14. T. Merdzhanova, "Fundamentals", in *Microcrystalline Silicon Films and Solar Cells Investigated by Photoluminescence Spectroscopy*, 1st ed. Jülich, Germany: Forschungszentrum Jülich GmbH, 2004, pp. 7-26.

15. G. Mor, O. Varghese, M. Paulose, K. Shankar and C. Grimes, "A review on highly ordered, vertically oriented TiO$_2$ nanotube arrays: Fabrication, material properties, and solar energy applications", *Solar Energy Materials and Solar Cells*, vol. 90, no. 14, pp. 2011-2075, 2006.

16. T. Takagahara and K. Takeda, "Theory of the quantum confinement effect on excitons in quantum dots of indirect-gap materials", *Physical Review B*, vol. 46, no. 23, pp. 15578-15581, 1992.

17. X. Quan, S. Yang, X. Ruan and H. Zhao, "Preparation of Titania Nanotubes and Their Environmental Applications as Electrode", *Environmental Science & Technology*, vol. 39, no. 10, pp. 3770-3775, 2005.

18. H. C. Liang, X. Z. Li, and J. Nowotny, "Photocatalytical Properties of TiO$_2$ Nanotubes", *Solid State Phenomena*, vol. 162, pp. 295–328, 2010.

19. C. Ampelli, G. Centi, R. Passalacqua and S. Perathoner, "Synthesis of solar fuels by a novel photoelectrocatalytic approach", *Energy & Environmental Science*, vol. 3, no. 3, pp. 292-301, 2010.

20. A. El Ruby Mohamed and S. Rohani, "Modified TiO$_2$ nanotube arrays (TNTAs): progressive strategies towards visible light responsive photoanode, a review", *Energy & Environmental Science*, vol. 4, no. 4, pp. 1065-1086, 2011.

21. K. Yamaguti and S. Sato, "Photolysis of water over metallized powdered titanium dioxide", *Journal of the Chemical Society, Faraday Transactions 1: Physical Chemistry in Condensed Phases*, vol. 81, no. 5, pp. 1237-1246, 1985.

22. C. Grimes, O. Varghese and S. Ranjan, "Photoelectrolysis", in *Light, Water, Hydrogen*, 1st ed., Springer Science+Business Media, LLC, 2008, pp. 115-190.

23. C. Richter and L. Menon, "Impact of adsorbed alkali ions on photoelectrochemical hydrogen production by titania nanotubes", *Energy & Environmental Science*, vol. 3, no. 4, pp. 427-433, 2010.

24. N. Kamarozaman, Z. Aznilinda, R. Bakar, S. Herman and M. Rusop, "Memristive Behavior of NAOH-Immersed Titania Nanostructures", *Journal of Mechanical Engineering and Sciences*, vol. 5, pp. 688-695, 2013.

25. L. Jing, J. Zhou, J. Durrant, J. Tang, D. Liu and H. Fu, "Dynamics of photogenerated charges in the phosphate modified TiO$_2$ and the enhanced activity for photoelectrochemical water splitting", *Energy & Environmental Science*, vol. 5, no. 4, pp. 6552-6558, 2012.

26. X. Zhang, H. Cui, M. Humayun, Y. Qu, N. Fan, X. Sun and L. Jing, "Exceptional performance of photoelectrochemical water oxidation of single-crystal rutile TiO$_2$ nanorods dependent on the hole trapping of modified chloride", *Scientific Reports*, vol. 6, no. 1, pp. 1-8, 2016.

27. C. Chen, F. Wu, H. Geng, W. Shen and M. Wang, "Analytical model for the photocurrent-voltage characteristics of bilayer MEH-PPV/TiO$_2$ photovoltaic devices", *Nanoscale Research Letters*, vol. 6, no. 1, p. 350, 2011.

28. D. Ribeiro, C. Souza and J. Abrantes, "Use of Electrochemical Impedance Spectroscopy (EIS) to monitoring the corrosion of reinforced concrete", *Revista Ibracon de Estruturas e Materiais*, vol. 8, no. 4, pp. 529-546, 2015.

29. T. Mallouk, "Chem 524 - Experiment 3 Electrochemical Impedance Spectroscopy of a Lithium Ion Battery", Departement of Chemistery., The Pennsylvania State University, Pennsylvania, Tech. Rep, 2017.

30. K. Gelderman, L. Lee and S. Donne, "Flat-Band Potential of a Semiconductor: Using the Mott–Schottky Equation", *Journal of Chemical Education*, vol. 84, no. 4, pp. 685-688, 2007.

31. "Electrochemical Impedance Spectroscopy Primer", Gamry Instruments., Warminster, Pennsylvania., Tutorials and Primers, 2005.

32. H. Lu, F. Li, G. Liu, Z. Chen, D. Wang, H. Fang, G. Lu, Z. Jiang and H. Cheng, "Amorphous TiO_2 nanotube arrays for low-temperature oxygen sensors", *Nanotechnology*, vol. 19, no. 40, p. 405504, 2008.

33. J. Luo, Y. Ma, H. Wang, and J. Chen, "Preparation of polypyrrole sensitized TiO_2 nanotube arrays hybrids for efficient photoelectrochemical water splitting," *Electrochimica Acta*, vol. 167, pp. 119–125, 2015.

34. Z. Endut, M. Hamdi and W. Basirun, "An investigation on formation and electrochemical capacitance of anodized titania nanotubes", *Applied Surface Science*, vol. 280, pp. 962-966, 2013.

35. J. Perdew, K. Burke and M. Ernzerhof, "Generalized Gradient Approximation Made Simple", *Physical Review Letters*, vol. 77, no. 18, pp. 3865-3868, 1996.

Chapter 6

PEDOT-Sensitized TiO₂ Photoelectrochemical System for Solar Hydrogen Production

As previously introduced in the literature review (Chapter 3), poly (3,4- ethylenedioxythiophene) (PEDOT) has shown very desirable features in various electronic applications. The material's utilization as a photosensitizer for solar-driven fuel production could be very promising. This could be related to the very low band gap that reaches almost 1.6 eV as well as its excellent electrochemical stability and large absorption coefficient. Henceforward, the results of spin coating PEDOT over the surface of TiO₂ nanotube arrays will be discussed concerning the morphological, structural and optical properties as well as the photoelectrochemical performance [1].

6.1 Morphological and Structural Characterization of TiO₂ Nanotubes

Figure 6.1 displays the scanning electron micrographs as well as the structural analysis of the TiO₂ nanotube array film fabricated as detailed in the previous chapter. Figure 6.1a displays the development of self-organized TiO₂ nanotube arrays which maintain an average length of 7 ± 2 µm and wall thickness of 10 ± 2 nm. Figure 6.1b shows the X-ray diffraction patterns obtained from the developed nanotubes annealed in air for 4 h at 450°C. The patterns affirm the development of anatase phase that crystallizes within the I4₁ space group with the lattice constants a=b=3.78354 Å and c= 9.61464 Å; $\alpha=\beta=\gamma=90°$ [2]. And the characteristic peaks of 25.09°, 37.63° , 47.87°, 53.86° and 54.746° affiliated to the (101), (004) (200) (105) (211) planes respectively as displayed in Figure 6.1b. It is worth to recognize that the sharp peak appearing at 40.072° is attributed to the Ti substrate [3].
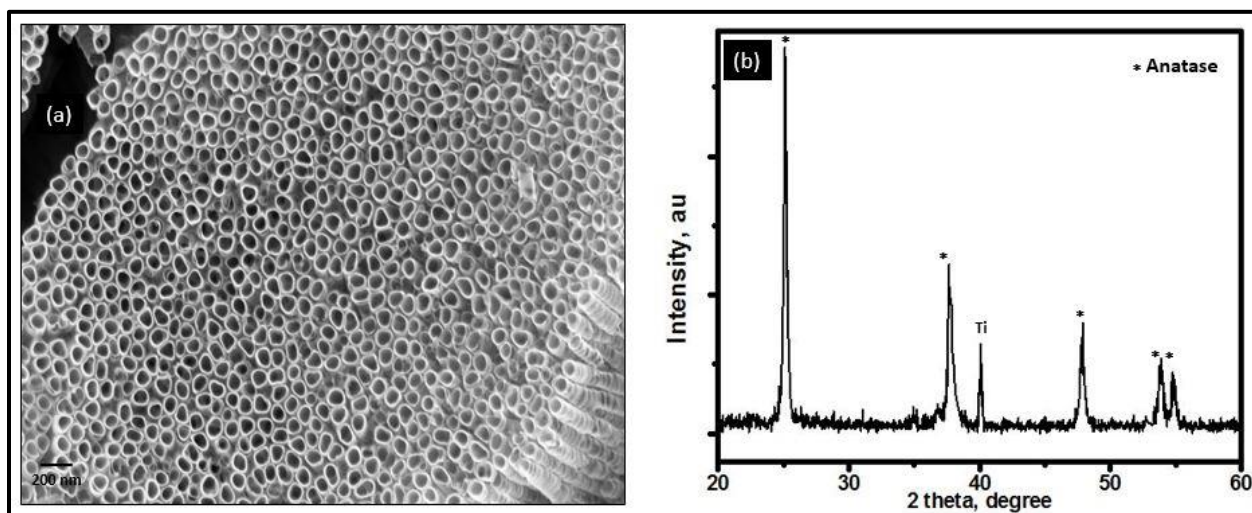
Figure 6.1: (a) FESEM top-view image of TiO₂ nanotubes anodized for 20 h at 20 V in formamide electrolytes containing 0.56 g NH₄F, at room temperature. (b) XRD patterns of annealed TiO₂ nanotubes at 450 °C for 4 h.

6.2 Fabrication and Characterization of PEDOT

Poly (3,4- ethylenedioxythiophene) (PEDOT), Figure 6.2a, is an immensely conductive, π conjugated polymer which can be synthesized either by oxidative chemical or electrochemical polymerization. Having an interchangeable single and double bonds leads to the existence of a delocalized system which is the main reason for the immense conductivity (300 S/cm) [4]. Thereupon, it is widely utilized in anti-static coatings, light emitting [1] and photovoltaic systems [5]. Similar to other conductive polymers like polypyrrole (PPy), PEDOT possesses a positive charge on each third consecutive ring while being in its oxidative form [6]. Hence, the conductivity is typically originates via hole transfer whereas in the reduced form, PEDOT is said to be non-conductive [7]. As formerly mentioned, electrochemical polymerization can be utilized to synthesize PEDOT, however, it is hard to scale up this process. In addition, it requires conductive substrates for the polymerization to take place and more importantly, elevated oxidation potentials can cause more oxidation to the polymer [8]. For the purpose of this research, chemical synthesis that can overcome these limitations was utilized where chemical oxidant (Iron-III p-toluenesulfonate) was used for the oxidation of the monomer (EDOT) producing a radical cation that reacts with another monomer to form a dimer [9] as precisly described in the experimental procedures.

The realization of the synthesized PEDOT has been verified by means of Fourier Transform Infrared (FT-IR) and Raman analyses. By evaluating the FT-IR spectrum of the PEDOT film along with the monomer spectrum as shown in Figure 6.2b and c, it is evident the absence of the strong band attributed to the C-H bending mode at 890 cm^{-1} in the polymer's spectrum with respect to that of the monomer confirms the formation of PEDOT chains. Bands at 1535, 1488 and 1396 cm^{-1} are assigned to the stretching modes of C=C and C-C within the thiophene ring. Vibrations at 984, 844 and 683.6 cm^{-1} are relevant to the C-S bond within the thiophene ring. The bands at 1190 and 1126 cm^{-1} are relevant to the stretching modes of the ethylenedioxy group. For more verification, Raman analysis (Figure 6.2d) shows the formation of strong peak at 1431 cm^{-1} where analogous peak patterns were previously reported by Selvaganesh et al (2007) for chemically synthesized PEDOT [10]. In this scenario, the obtained results validate the attainment of the polymerization process.
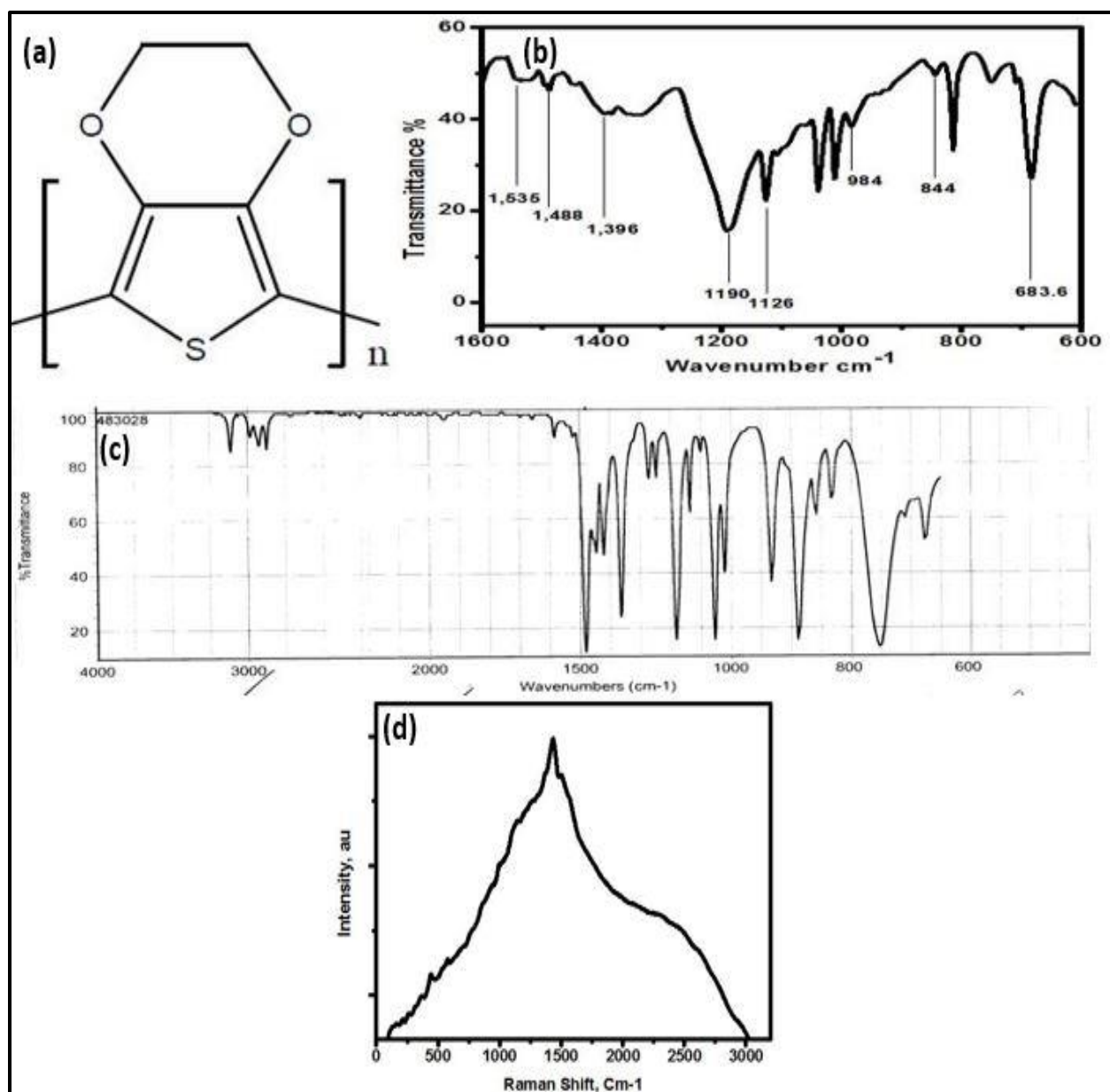
Figure 6.2: (a) Poly (3,4- ethylenedioxythiophene) (PEDOT), (b) FT-IR spectrum of PEDOT, (c) FT-IR spectrum of EDOT monomer and (d) Raman spectrum of PEDOT.

6.3 Realization and Characterization of PEDOT-TiO$_2$ Heterojunctions

Figure 6.3 illustrates the FESEM top-view images of the hybrid PEDOT-TiO$_2$ nanotubes formed via spin coating of 0.25, 0.5, 0.75 and 1 ml PEDOT respectively, over an active area of 2 cm^2 of the anodically fabricated TiO$_2$ nanotubes. Considering the dominant influence of the coating amount on the morphology of the PEDOT film developed over the TiO$_2$ nanotubes. While spin coating of 0.25 ml yields the formation of random, non-continuous layer over the surface of the tubes leaving some open pores, total coverage of the nanotubes' surface is

observed upon spin coating of 1 ml. under all conditions, the nanotubular structure is very well conserved. The morphological observations affirm the existence of PEDOT in the PEDOT/TiO$_2$ hybrids.
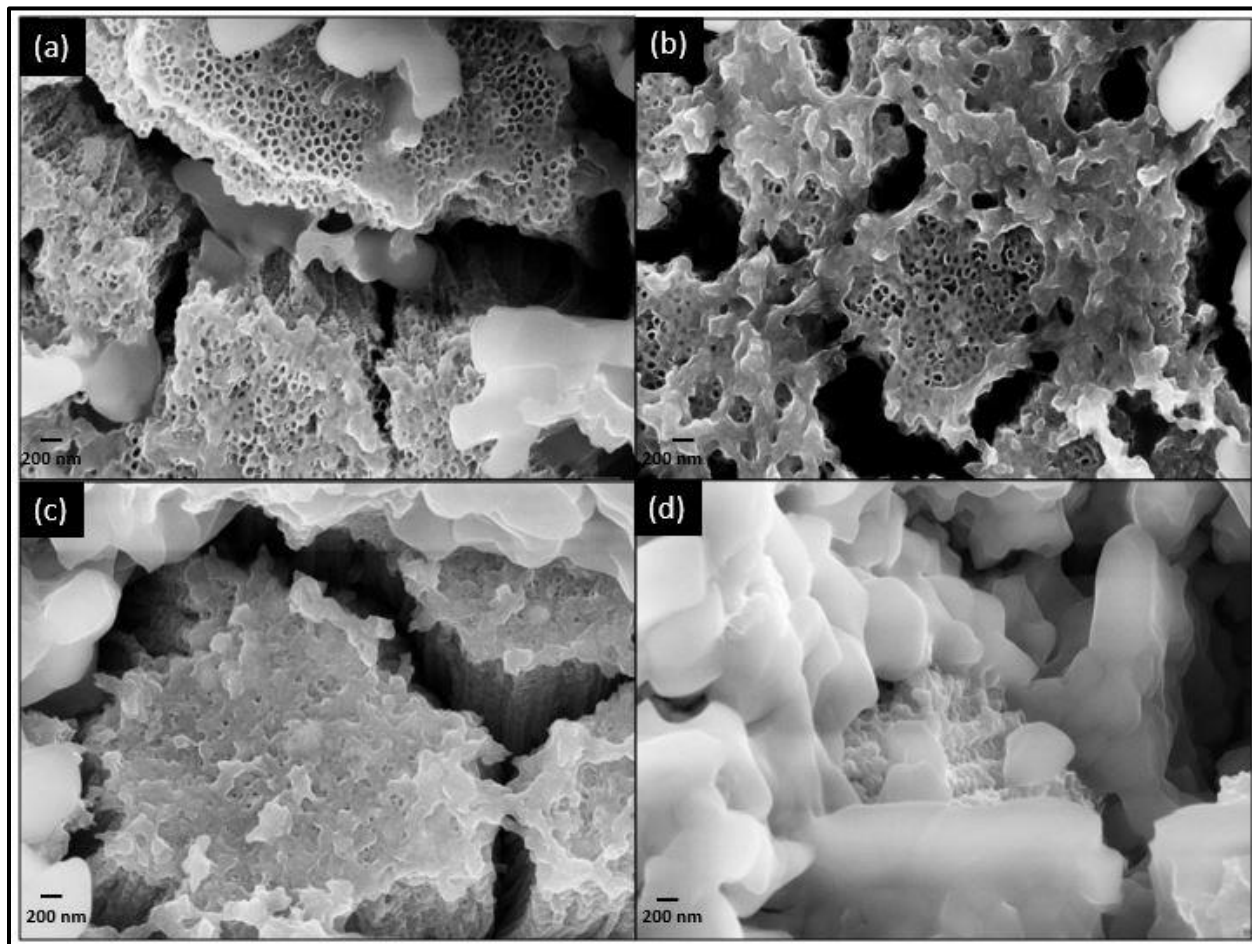
Figure 6.3: FESEM top-view images of PEDOT-TiO$_2$ hybrid photoelectrodes formed via spin coating of (a) 0.25 ml, (b) 0.5 ml, (c) 0.75 ml and (d) 1 ml of PEDOT over the surface of TiO$_2$ nanotube array.

In the interest of investigating the development of visible light active photoelectrodes, the optical properties for all the fabricated samples were appraised via the ultraviolet-visible diffuse reflectance spectra (UV-vis DRS) as shown in Figure 6.4. In this part of the thesis, the quantity of the visible light absorbed is our main concern instead of just shifting the absorption edge to higher wavelengths. It could be recognized that the bare TiO$_2$ nanotubes maintained an absorption band edge at nearly 382.6299 nm, related to a band gap of 3.24072 eV. Upon spin coating of PEDOT, the absorption band edge has been pushed in the direction of longer wavelengths within the visible spectrum indicating that PEDOT can act as a sensitizer to capture a large number of photons. The spectrum shows that the extent of red shift increases with increasing the amount of sensitizer PEDOT maintaining 405.2865 nm (3.05956 eV), 479.92003 nm (2.58376 eV) and 694.7578 nm (1.78479 eV) for 0.25, 0.5 and 0.75 ml sensitized samples respectively whereas, the absorption of 1ml PEDOT-modified TiO$_2$ is kept lower than that of all other hybrid electrodes which signifies that excess PEDOT film that entirely covers the TiO$_2$ nanotubes' surface could impede the absorption of the underlying tubes and could possibly cause

light reflection [11]. We should bear in mind that, all the band gap energies of the PEDOT-sensitized TiO_2 electrodes are kept lower than that of the pristine one implying that this binary architecture system could be photoexcited to generate more electron-hole pairs under visible illumination. Table 6.1 lists the obtained band gap values for all the fabricated samples. The enhancement in the optical properties of the hybrid photoelectrodes could be further elucidated based on the fact that the positions of the highest occupied molecular orbit (HOMO) and lowest unoccupied molecular orbit (LUMO) levels of PEDOT are noticeably more negative with respect to the valence band (VB) and conduction band (CB) of TiO_2. That is upon illumination, PEDOT is excited first with the photoexcited electrons migrating to the CB of TiO_2 whereas the photoinduced holes follow to the PEDOT layer in a manner analogous to photosensitizer that acts as a hole transport layer for decisive charge carriers' separation [12].
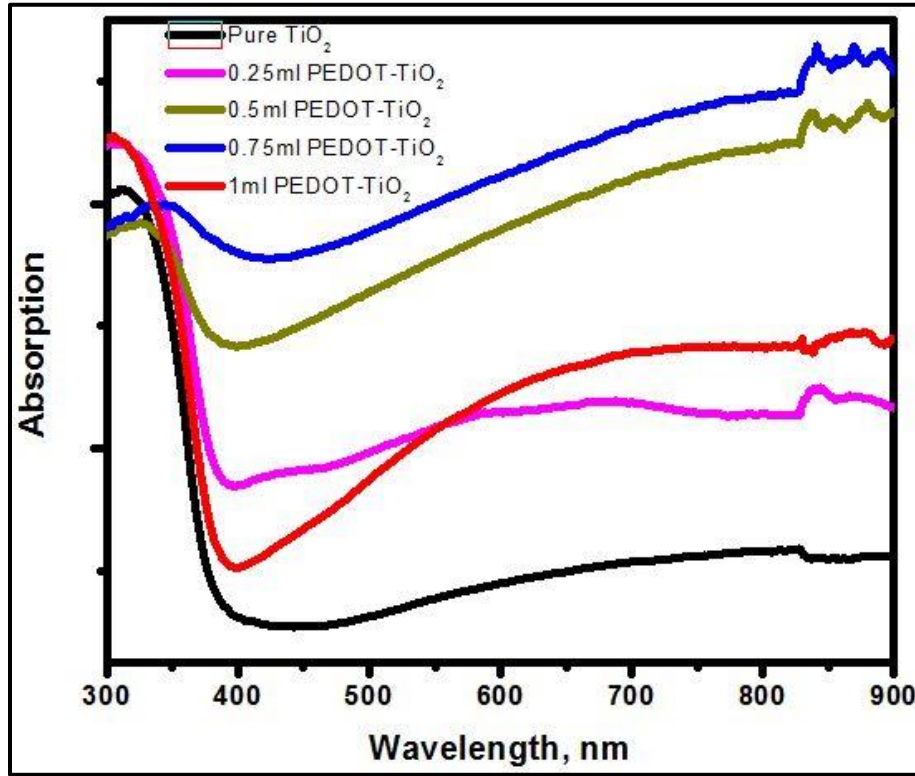
Figure 6.4: Diffuse reflectance spectra (DRS) for pure TiO₂ and PEDOT-TiO₂ hybrid photoelectrodes.

Table 6.1: Absorption edges and energy gaps for pure TiO₂ and PEDOT-TiO₂ samples.

Sample	Absorption edge (nm)	Band gap (E_g; eV)
Pristine TiO_2	~382.6299	~ 3.24072
0.25ml PEDOT-TiO_2	~405.2865	~3.05956
0.5ml PEDOT-TiO_2	~479.92003	~2.58376
0.75ml PEDOT-TiO_2	~694.7578	~1.78479
1ml PEDOT-TiO_2	~388.8938	~3.18853

The photocatalytic activity utilizing the developed PEDOT-sensitized TiO_2 heterojunctions was carried out in 1 M KOH electrolyte via the ordinary three-electrode electrochemical cell. Dark scan exhibits an imperceptible photocurrent response in the range of 0.1 µA/cm^2. Under simulated light (AM 1.5 G), Figure 6.5 indicates large increase in the photocurrent densities as the applied voltage for both the bare TiO_2 nanotubes as well as the PEDOT/TiO_2 heterojunctions is increased. This behavior indicates that the current under illumination conditions is mainly produced by the effect of the incident photons without the contribution of the dark current which could be related to the better electron transfer ability of the fabricated electrodes. It should be considered that all the tested photoelectrodes exhibit n-type behavior that is positive photocurrents at anodic potentials, which indicates that the amount of spin-coated p-type PEDOT is greatly less in comparison with the host n-type TiO_2.

The highest achievable photocurrent response is approximately 2.89 mA cm^{-2}, obtained for the 0.5 ml modified sample which illustrate a 15 fold increase relative to that of the pristine TiO_2 (0.1821 mA cm^{-2}). The attained enhancement in the photocurrent spectral response is principally related to the internal electric field developed upon coupling PEDOT with TiO_2. Accordingly, the p-type region will attract negative charges and the n-type TiO_2 will attract positive charges and this in return will be beneficial for favorable separation of photoinduced charge carriers and rapid transfer at the organic/inorganic interface. It is worth noting that the 0.5 ml modified sample exhibited a higher photocurrent density than the 0.25 ml as well as the 0.75 and the 1 ml modified counterparts, which implies that the 0.5 ml modified sample acquires more sensitizer amount of PEDOT than the 0.25 ml as well as more favorable p-n junction than the 0.75 and 1 ml samples. The results suggest that as the PEDOT content increases beyond an optimal value, the PEDOT film starts to accumulate over the surface of the nanotubes increasing the possibility of undesired recombination between charge carriers and reducing the photocatalytic activity.

It should be also mentioned that it is not just the dominance of the carriers' separation within the p-n junction that is accountable for the relative enhancement in photocurrent. Other aspects could contribute to the improved response which may be related to the enhanced absorbance capability that PEDOT favors the system with visible light absorption and hence more active electrons along with the ordered orientation of the TiO_2 nanotubes that not only promote electron percolation but also provide large surface area for polymer's deposition [13,14].
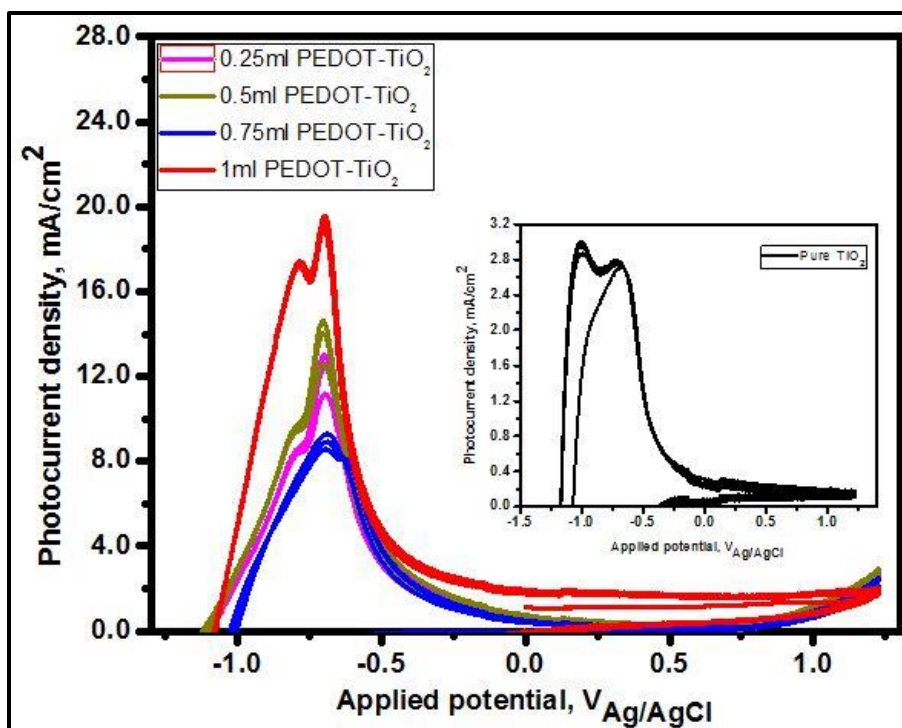
Figure 6.5: Photocurrent density against applied potential in 1 M KOH electrolyte under AM 1.5G for pure TiO₂ (inset) and PEDOT- TiO₂ hybrid photoelectrodes.

Table 6.2: Photocurrent densities and open-circuit potentials for pure TiO₂ and PEDOT-TiO₂ samples.

Pristine TNTs	J_{SC}	V_{OC}
	0.1821 mA/cm^2	-1.1698 V$_{Ag/AgCl}$
PEDOT-sensitized TNTs	J_{SC}	V_{OC}
0.25ml	2.57 mA/cm^2	-1.11838 V$_{Ag/AgCl}$
0.5ml	2.89 mA/cm^2	-1.11825 V$_{Ag/AgCl}$
0.75ml	2.467 mA/cm^2	-1.0228 V$_{Ag/AgCl}$
1ml	2.008 mA/cm^2	-1.0771 V$_{Ag/AgCl}$

In order to have more insight on the charge transfer kinetics of the fabricated electrodes, electrochemical impedance spectra (EIS) were measured to estimate the resistive and capacitive components ascribed to the processes occurring on the working electrode within a frequency interval from 100 KHz to 50 mHz. Figure 6.6 illustrates the Nyquist plot for the pristine as well as the polymer sensitized sample. It is clearly evident that the impedance behavior endures two semicircles, emphasizing typical two time constants behavior related to the process at the depletion region of the semiconductor in series with the Helmholtz layer within the electrolyte. This perception will be the basis of the analysis for the obtained spectra as well as the selection of the equivalent circuit. When a semiconductor is immersed in the electrolyte a depletion region originates in the vicinity close to the junction with the electrolyte. Balance between the electrochemical potentials within the two sides occurs by electron migration from the electrode to the solution, since the fermi level of the n-type semiconductor is ordinarily above the redox potentials of the solution. The semiconductor is thus depleted of electrons creating what is known as the depletion region and a positive charge layer emerges on the electrode side. The produced positively charged layer attracts the closest approaching negative mobile ions from the

solution creating the so-called Helmholtz layer. Having the principle, that both the space charge region as well as the Helmholtz layer can be modeled as capacitors, the electrode/solution interface can then be described as a lineup of electrical analogs like resistors and capacitors [15,16].
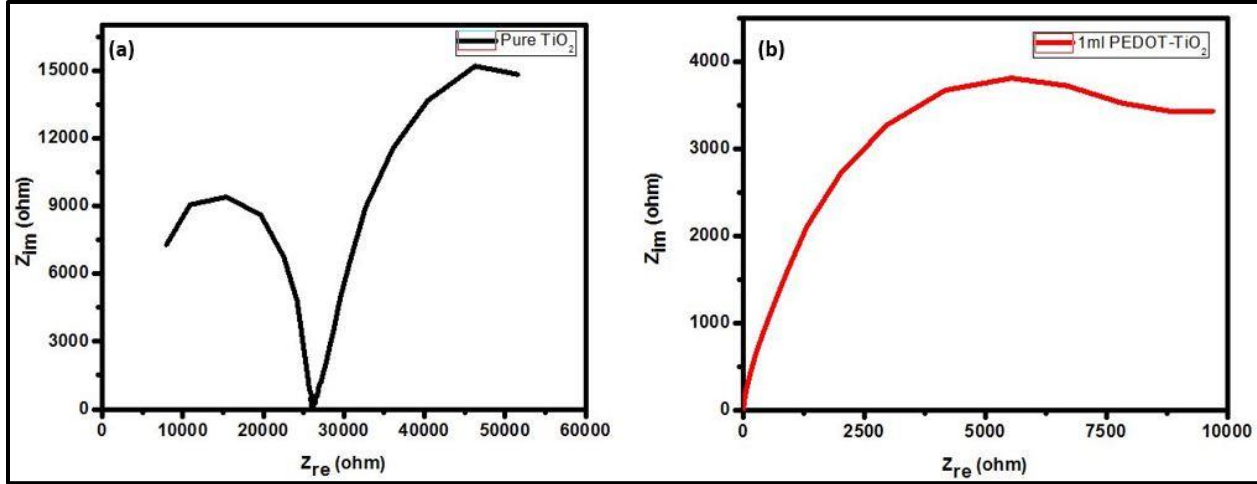
Figure 6.6: Illuminated Nyquist plots of (a) Pure TiO₂ nanotubes and (b) 1ml PEDOT-sensitized TiO₂.

Using this model, the impedance behavior at each interface is described according to the circuit displayed in Figure 6.7a where two interfaces can be recognized, one at high frequency range that is related to charge transfer process within the space charge layer and the other at low frequency range related to the electron transfer at the Helmholtz layer. The process occurring within the polymer sensitized photoelectrode will be represented by similar electrical analog except with the addition of a typical feature related to the resistance within the polymeric film itself. (See Figure 6.7b) [17].
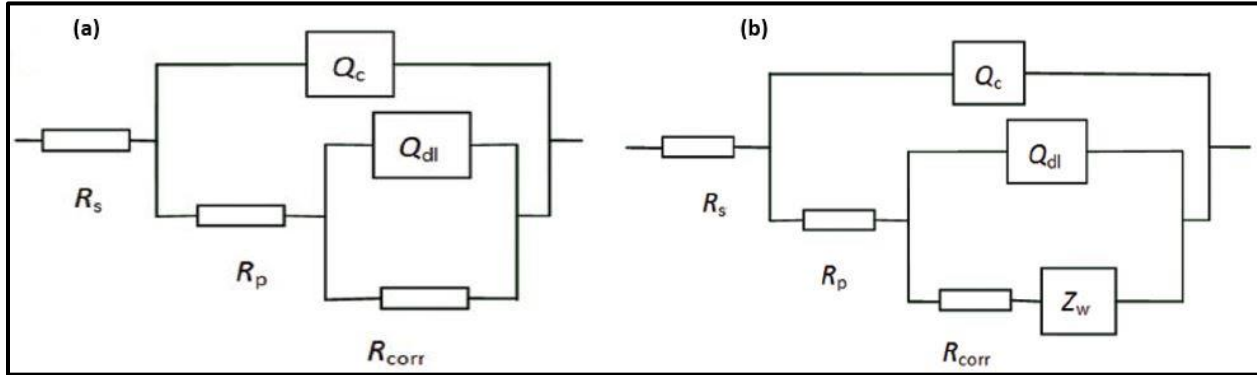
Figure 6.7: Equivalent circuit model for (a) pure TiO₂ and (b) PEDOT-sensitized TiO₂ [18].

These equivalent circuits have been utilized to fit the empirical impedance data obtained for the fabricated samples. Table 6.3 illustrates the values of circuit elements to which the pure TiO_2 as well as the 1ml PEDOT sensitized TiO_2 nanotubes were fitted using EC-Lab software (same approach could be followed for other samples) and Figure 6.8 represents both fitted and experimental curves for the two samples.

Table 6.3: Extracted circuit elements for pure TiO₂ and 1ml PEDOT-sensitized TiO₂

Circuit element	Extracted values for Pure TiO$_2$	Extracted values for 1ml PEDOT sensitized TiO$_2$
R$_{ct1}$	21102 Ohm	1814 Ohm
Q$_{ct1}$	0.259 1e-9 F.s^(a-1)	20.33e-6 F.s^(a-1)
R$_{ct2}$	48855 Ohm	7322 Ohm
Q$_{ct2}$	38.94 e-6 F.s^(a-1)	26.39 e-6 F.s^(a-1)
W		1292 Ohm.s^-1/2
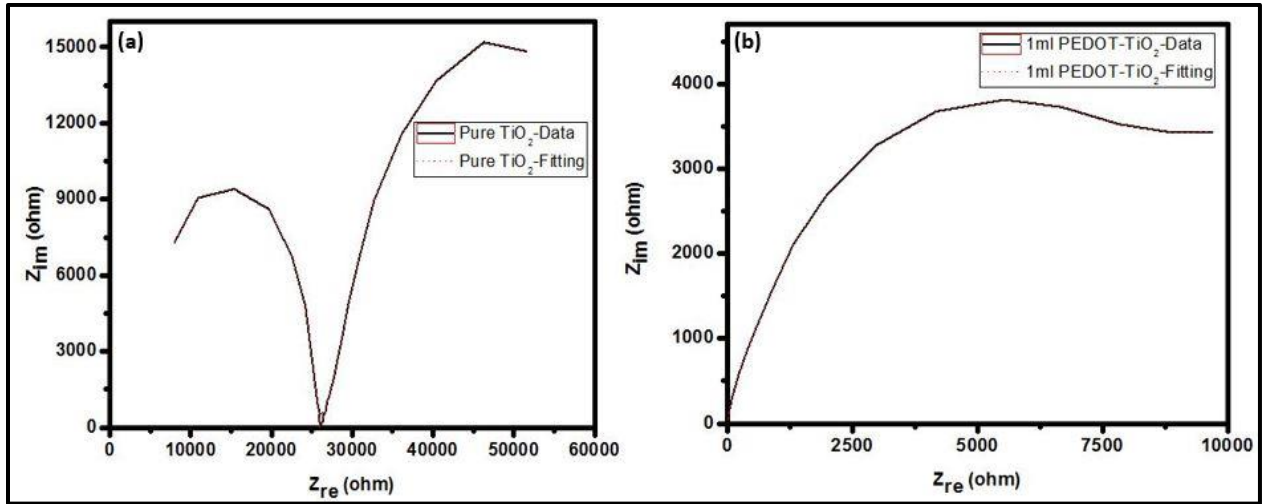
Figure 6.8: Empirical curve (solid) against fitted curve (dotted) of (a) Pure TiO₂ and (b) 1ml PEDOT-sensitized TiO₂.

The fitting results validate that heterojunction exhibits more rapid interfacial electron transfer capabilities and hence superior catalytic performance for the oxygen-evolution reaction (OER) as indicated by the smaller radius of the arc of the Nyquist diagram depicted in Figure 6.6. This implies that the incorporation of PEDOT could provide more enhanced separation and mobility as well as efficiently suppress the undesired electron-hole recombination. It is worth highlighting, that more adequate compliance has been obtained between the fitted and the empirical results due to the replacement of all chemical capacitance by constant phase elements (CPE) (i.e; pesudocapacitance) that can describe the behavior at the double layer as a pragmatic, non-intuitive capacitor accompanied with random allocation of current within the photoelectrode [17]. Giving an initial look at the extracted circuit elements, we noticed that the interface capacitance of the PEDOT sensitized sample is greater than that of the pristine TiO$_2$. This on one side could be attributed to the existence of surface states that can trap photoexcited charges leading to increase the capacitance at the interface as previously indicated [19]. However, this phenomenon is commonly associated with depreciation in the photocurrent response. On the other side, the increased capacitance could be explained based on the fact that conductive polymers exhibit pseudo-faradic behavior, that is the ability to store electric charges through charge transfer among the semiconductor and the solution. Accordingly, energy is retained in the polymer by building-up of charges in the electrical double layer [20,21]**.**

Further analysis was performed to appraise the PEC performance for the PEDOT sensitized TiO$_2$ photoelectrodes according to the Mott-Schottky equation:

$$\frac{1}{C^2} = \frac{2}{\varepsilon\varepsilon_0 e\, N_d}\left(E - E_{fb} - \frac{KT}{e}\right) \qquad (6.1)$$

Where C is the capacity of the space charge layer, ε is the dielectric constant (ε= 48 for anatase TiO$_2$), ε_0 is the vacuum permittivity (8.86 *10^{-14} F cm^{-1}), e is the electronic charge (1.6*10^{-19} C), N$_D$ carriers' concentration, E is the applied voltage, E$_{fb}$ is the flat band potential, T is the absolute temperature and K is the Boltzmann constant (1.38 *10^{-23} J K^{-1}) [22]. Figure 6.9 represents the Mott-Schottky plots for the bare as well as PEDOT sensitized TiO$_2$ nanotubes, where the flat band potential (E$_{fb}$) can be estimated from the intercept with the x-axis. For the pristine TiO$_2$, E$_{fb}$ is approximately indicated at -0.583837 V$_{Ag/AgCl}$ as reported earlier in the previous chapter. Whereas, upon anchoring PEDOT over the titania surfaces, the E$_{fb}$ is valued at -0.552978 V$_{Ag/AgCl}$, -0.54473 V$_{Ag/AgCl}$, -0.61025 V$_{Ag/AgCl}$ and - 0.51174 V$_{Ag/AgCl}$ for the 0.25, 0.5, 0.75 and 1 ml sensitized samples. Supported with the values of E$_{fb}$ as well as the energy gaps estimated by the UV-vis DRS, we can predict the band edge positions of the fabricated samples. Based on the certainty that TiO$_2$ is considered a highly doped n-type semiconductor due to the existence of the intrinsic non-stoichiometry produced by the oxygen vacancies [15], it is believed that the conduction band (E$_{CB}$) is said to be 0.1 eV more negative than that of the flat band potential (E$_{fb}$) according to [23,24]. Hence, the positions of the band energy levels for all the fabricated samples are demonstrated as shown in the schematic of Figure 6.10 and table 6.4.
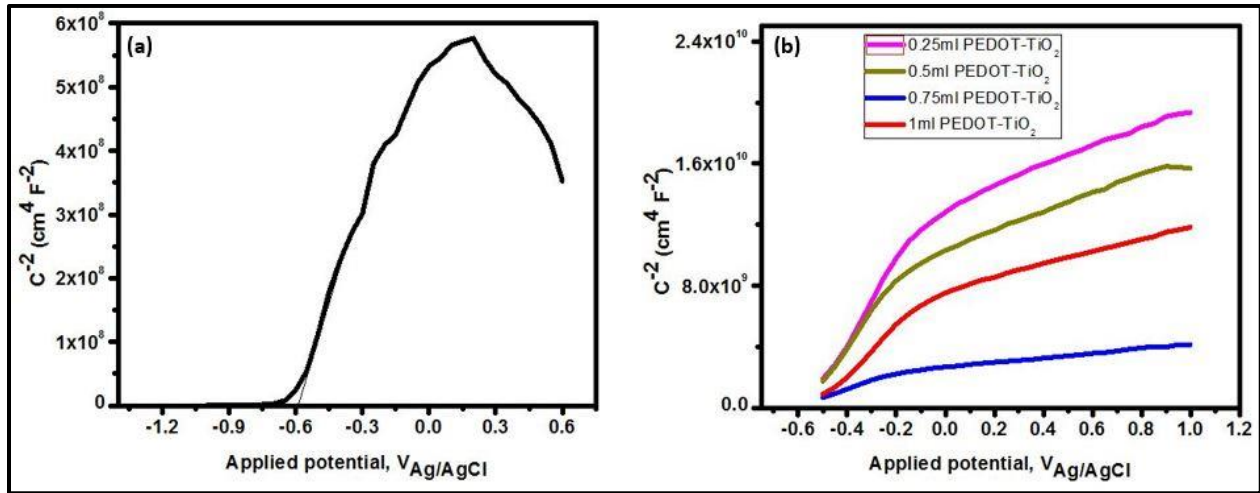

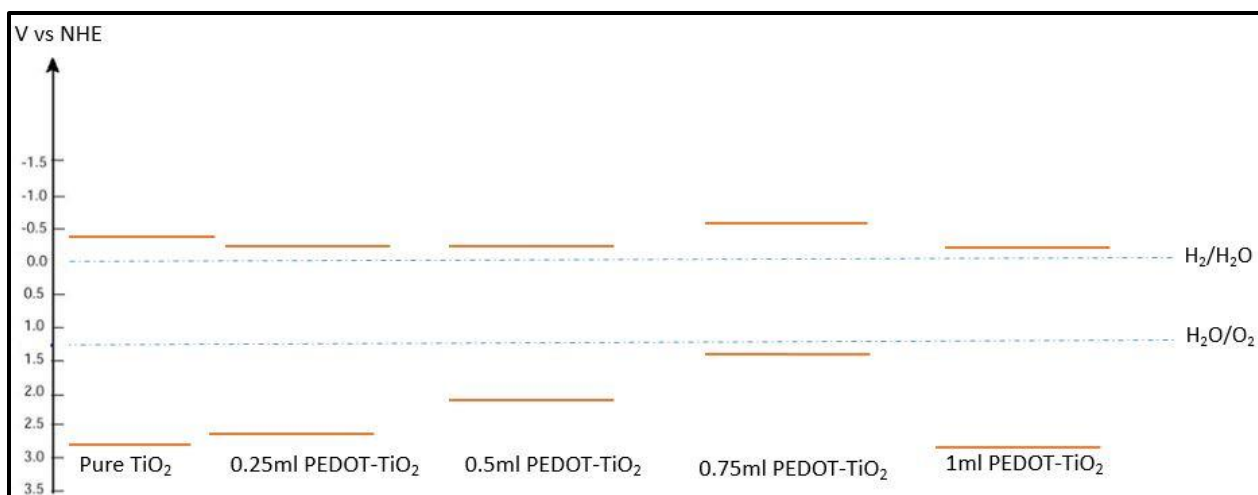*Figure 6.9: Illuminated Mott-Schotky plots of (a) Pure TiO$_2$ and (b) PEDOT- TiO$_2$ hybrid photoelectrodes.*

Figure 6.10: Band edge positions of pure TiO₂ as well as PEDOT-TiO₂ hybrid photoelectrodes relative to the redox potentials of water splitting.

Table 6.4: Electrochemical potentials of VB and CB as well as band gap values pure TiO₂ and PEDOT-TiO₂ samples.

Sample	VB; V vs NHE	CB; V vs NHE	E_g; eV
Pure TiO$_2$	2.75389	-0.486837	3.24072
0.25ml PEDOT-TiO$_2$	2.60358	-0.455978	3.05956
0.5ml PEDOT-TiO$_2$	2.13603	-0.44773	2.58376
0.75ml PEDOT-TiO$_2$	1.271544	-0.51325	1.78479
1ml PEDOT-TiO$_2$	2.77379	-0.41474	3.18853

To adequately recognize the mechanism of PEC water splitting using the fabricated PEDOT-sensitized TiO$_2$ photoelectrodes, a schematic illustration of the potential energy diagram for the hybrid structure is represented in Figure 6.11. Upon directing simulated sunlight to the junction, the electrons within the HOMO level of PEDOT are firstly excited towards the LUMO then the electrons transport could readily follow towards the CB of TiO$_2$, since the CB of TiO$_2$ is said to be more positive than the LUMO of PEDOT. Simultaneously, some electrons are agitated from the VB to the CB of TiO$_2$ due the inclusion of some UV light within the incident radiations. Due to the influence of the internal electric field produced within the p-n junction, the separation of the photoexcited charges can be considerably improved where the photogenerated holes of TiO$_2$ migrate to HOMO level of PEDOT and hence they can be easily transported to the interface between the semiconductor and the electrolyte to carry out water oxidation reaction prohibiting all recombination pathways. In turn, all the photogenerated electrons migrate towards the counter Pt electrode to proceed for the hydrogen generation reaction. The key point is related to the synergistic response in this binary architecture system utilizing PEDOT as continually donating electrons and accepting holes from TiO$_2$, hence, prolonging the lifetime of the produced charge carriers and significantly improving the photocatalytic activity [12,25].
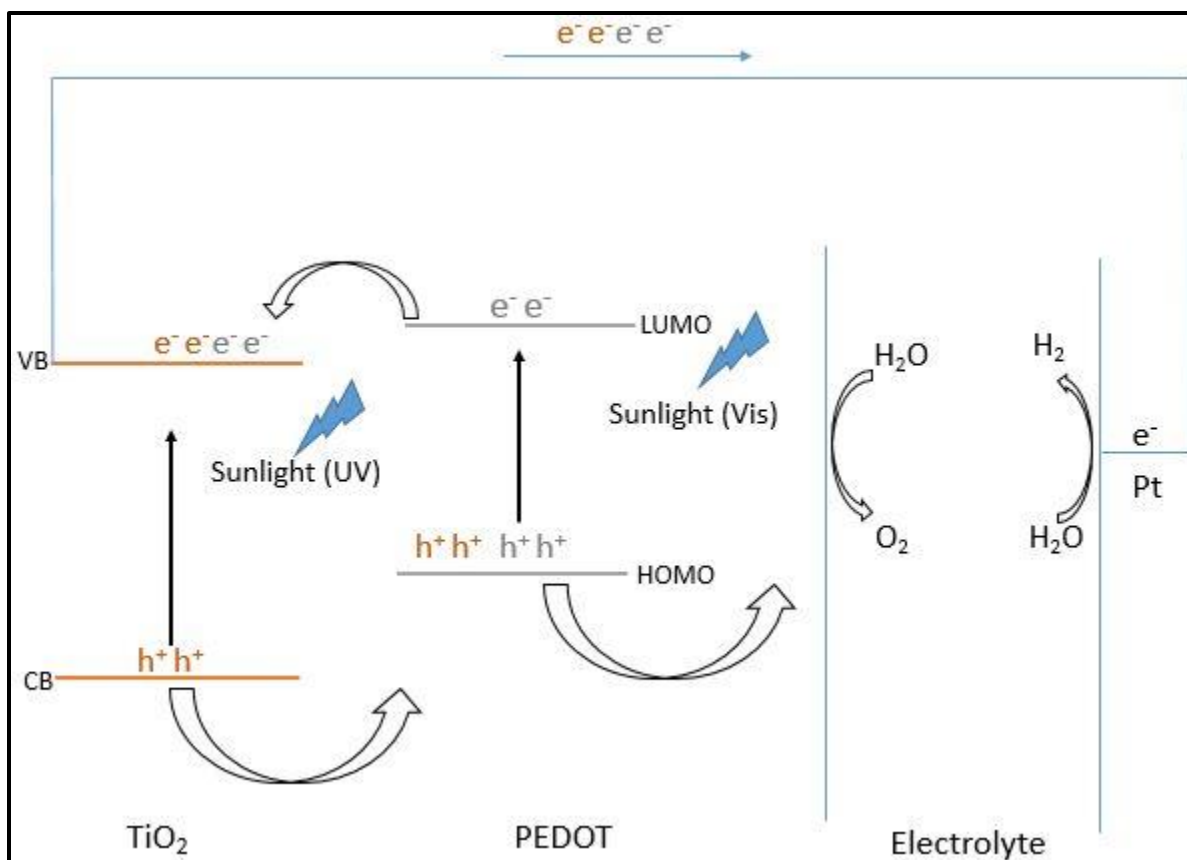
Figure 6.11: Schematic diagram demonstrating the water splitting mechanism utilizing PEDOT-TiO₂ hybrid photoelectrodes.

To sum up, this study exemplifies the realization and characterization of mixed organic-inorganic system for water splitting applications where the visible-light absorption properties of PEDOT are combined together with the enhanced charge transport capabilities of TiO_2 nanotubes building-up a novel hybrid photoelectrochemical system for hydrogen production. The morphological characterization shows the existence of PEDOT films over the surface of the anodically fabricated TiO_2 nanotubes and the structural analysis verified the accomplishment of the polymerization process for the sensitized PEDOT. Optical properties were investigated through UV-vis DRS which revealed the effect of PEDOT in expanding to the optical response and narrowing down the band gap of TiO_2. The PEC performance of the nanocomposite system was assessed by linear sweep voltammetry, which showed a tremendous increase in the photocurrent response reaching 2.89 mA cm^{-2}, a value 15 fold that of the pristine TiO_2. Additionally, electrochemical impedance was utilized to investigate the charge transfer kinetics admitting that the developed samples exhibit two time constants behavior where the sensitized electrodes maintain superior conductivity and better mobility of charges in comparison with the TiO_2 counterpart. We have also extended the analysis to estimate the band edge positions of the fabricated samples utilizing the data extracted from the Mott-Schottky plots which confirms not only band gap narrowing but also remarkable charge separation capabilities for this electroactive heterojunction rendering it highly efficient for water cleavage.

References

1. L. Groenendaal, F. Jonas, D. Freitag, H. Pielartzik and J. Reynolds, "Poly(3,4-ethylenedioxythiophene) and Its Derivatives: Past, Present, and Future", *Advanced Materials*, vol. 12, no. 7, pp. 481-494, 2000.

2. C. Carlucci, F. Conciauro, B. Scremin, A. Antico, M. Muscogiuri, T. Sibillano, C. Giannini, E. Filippo, C. Lorusso, P. Congedo and G. Ciccarella, "Properties of Aluminosilicate Refractories with Synthesized Boron-Modified TiO_2 Nanocrystals", *Nanomaterials and Nanotechnology*, vol. 5, p. 8, 2015.

3. N. Allam and C. Grimes, "Room Temperature One-Step Polyol Synthesis of Anatase TiO_2 Nanotube Arrays: Photoelectrochemical Properties", *Langmuir*, vol. 25, no. 13, pp. 7234-7240, 2009.

4. S. Spanninga, "The Characterization and Fabrication of Poly (3,4-Ethylenedioxythiophene) Enzyme Based Biosensors", Ph.D. dissertation, Macromolecular Science and Engineering., The University of Michigan., Michigan, USA, 2010.

5. S. Na, G. Wang, S. Kim, T. Kim, S. Oh, B. Yu, T. Lee and D. Kim, "Evolution of nanomorphology and anisotropic conductivity in solvent-modified PEDOT:PSS films for polymeric anodes of polymer solar cells", *Journal of Materials Chemistry*, vol. 19, no. 47, pp. 9045-9053, 2009.

6. G. Zotti, S. Zecchin, G. Schiavon, F. Louwet, L. Groenendaal, X. Crispin, W. Osikowicz, W. Salaneck and M. Fahlman, "Electrochemical and XPS Studies toward the Role of Monomeric and Polymeric Sulfonate Counterions in the Synthesis, Composition, and Properties of Poly(3,4-ethylenedioxythiophene)", *Macromolecules*, vol. 36, no. 9, pp. 3337-3344, 2003.

7. H. Allcock, F. Lampe and J. Mark, *Contemporary polymer chemistry*, 3rd ed. Upper Saddle River, NJ, USA: Wiley, 2003.

8. W. Feng, A. Wan and E. Garfunkel, "Interfacial Bonding and Morphological Control of Electropolymerized Polythiophene Films on ZnO", *The Journal of Physical Chemistry C*, vol. 117, no. 19, pp. 9852-9863, 2013.

9. D. Nguyen and H. Yoon, "Recent Advances in Nanostructured Conducting Polymers: from Synthesis to Practical Applications", *Polymers*, vol. 8, no. 4, p. 118, 2016.

10. S. Selvaganesh, J. Mathiyarasu, K. Phani and V. Yegnaraman, "Chemical Synthesis of PEDOT–Au Nanocomposite", *Nanoscale Research Letters*, vol. 2, no. 11, pp. 546-549, 2007.

11. J. Luo, Y. Ma, H. Wang and J. Chen, "Preparation of polypyrrole sensitized TiO_2 nanotube arrays hybrids for efficient photoelectrochemical water splitting", *Electrochimica Acta*, vol. 167, pp. 119-125, 2015.

12. K. Siuzdak, M. Szkoda, J. Karczewski, J. Ryl and A. Lisowska-Oleksiak, "Titania nanotubes infiltrated with the conducting polymer PEDOT modified by Prussian blue – a novel type of organic–inorganic heterojunction characterised with enhanced photoactivity", *RSC Adv.*, vol. 6, no. 80, pp. 76246-76250, 2016.

13. K. Siuzdak, M. Szkoda, A. Lisowska-Oleksiak, J. Karczewski and J. Ryl, "Highly stable organic–inorganic junction composed of hydrogenated titania nanotubes infiltrated by a conducting polymer", *RSC Adv.*, vol. 6, no. 39, pp. 33101-33110, 2016.

14. L. Bertoluzzi, L. Badia-Bou, F. Fabregat-Santiago, S. Gimenez and J. Bisquert, "Interpretation of Cyclic Voltammetry Measurements of Thin Semiconductor Films for Solar Fuel Applications", *The Journal of Physical Chemistry Letters*, vol. 4, no. 8, pp. 1334-1339, 2013.

15. R. Beranek, "(Photo)electrochemical Methods for the Determination of the Band Edge Positions of TiO_2-Based Nanomaterials", *Advances in Physical Chemistry*, vol. 2011, pp. 1-20, 2011.

16. S. Al-Hilli and M. Willander, "The pH Response and Sensing Mechanism of n-Type ZnO/Electrolyte Interfaces", *Sensors*, vol. 9, no. 9, pp. 7445-7480, 2009.

17. T. Lopes, L. Andrade, H. Ribeiro and A. Mendes, "Characterization of photoelectrochemical cells for water splitting by electrochemical impedance spectroscopy", *International Journal of Hydrogen Energy*, vol. 35, no. 20, pp. 11601-11608, 2010.

18. S. Wang, F. Liu ,J. Chen, E. Han, S. Xu, B. Hu, J. Lu, "Influence of Flaky Nickel Powder on Permeation Resistance of Fluorocarbon Coatings", *Chinese Journal of Materials Research*, vol. 29 no. 4, pp. 255-261, 2015.

19. A. Amer, M. El-Sayed and N. Allam, "Tuning The Photoactivity of Zirconia Nanotubes-Based Photoanodes via Ultrathin Layers of ZrN: An Effective Approach Toward Visible-

Light Water Splitting", *The Journal of Physical Chemistry C*, vol. 120, no. 13, pp. 7025-7032, 2016.

20. T. Kelly, K. Yano and M. Wolf, "Supercapacitive Properties of PEDOT and Carbon Colloidal Microspheres", *ACS Applied Materials & Interfaces*, vol. 1, no. 11, pp. 2536-2543, 2009.

21. B. Babakhani and D. Ivey, "Improved capacitive behavior of electrochemically synthesized Mn oxide/PEDOT electrodes utilized as electrochemical capacitors", *Electrochimica Acta*, vol. 55, no. 12, pp. 4014-4024, 2010.

22. H. Lu, F. Li, G. Liu, Z. Chen, D. Wang, H. Fang, G. Lu, Z. Jiang and H. Cheng, "Amorphous TiO_2 nanotube arrays for low-temperature oxygen sensors", *Nanotechnology*, vol. 19, no. 40, p. 405504, 2008.

23. W. Chun, A. Ishikawa, H. Fujisawa, T. Takata, J. Kondo, M. Hara, M. Kawai, Y. Matsumoto and K. Domen, "Conduction and Valence Band Positions of Ta_2O_5, TaON, and Ta_3N_5 by UPS and Electrochemical Methods", *The Journal of Physical Chemistry B*, vol. 107, no. 8, pp. 1798-1803, 2003.

24. Y. Matsumoto, "Photoelectrochemical Properties of the Zn-Ti-Fe Spinel Oxides", *Journal of The Electrochemical Society*, vol. 133, no. 4, pp. 711-716, 1986.

25. Y. Lin, D. Li, J. Hu, G. Xiao, J. Wang, W. Li and X. Fu, "Highly Efficient Photocatalytic Degradation of Organic Pollutants by PANI-Modified TiO_2 Composite", *The Journal of Physical Chemistry C*, vol. 116, no. 9, pp. 5764-5772, 2012.

Chapter 7

Conclusions and Future Recommendations

7.1 Conclusions

Nowadays, the exploration of a novel, back-up source of energy to replace fossil fuels is of crucial importance. Hydrogen is regarded as a promising energy carrier to store solar energy provided that it is produced via a renewable, carbon-free approach and that its large scale production is feasible. Hence, our research to enhance the efficiency of the photoelectrodes utilized in PEC cells to generate hydrogen is one of the efforts devoted to the advent of hydrogen economy via renewable hydrogen generation. In this thesis, we adopted alkali as well as PEDOT-modified TiO_2 photoelectrodes to favorably split water into oxygen and hydrogen.

In the first part of the thesis, a random and dis-continuous layer of Na^+ and OH^-/SO_4^{2-} was formed over the top surface of the anodiaclly fabricated TiO_2 nanotubes by a simple soaking treatment. The layer produced a disordered TiO_2 nanostructure with an enhanced photocurrent response. It was concluded that the inclusion of band tail states created regions within the band gap that can trap charge carriers; hence, suppress the undesired recombination process and increase the photocurrent. Further assessment revealed less band bending requirements for the Na^+-containing titania. It is believed that the decrease in the steepness of the band edges upon Na^+ adsorption is the main reason behind this behavior which was also asserted by the negative shift of the flat band potential obtained by the Mott-Schottky analysis. It was also realized in this study that the surface-modified electrodes possess superior conductivity as well as better separation of excitons in comparison with the unmodified counterpart as illustrated by electrochemical impedance spectroscopy. Decisively, DFT calculations proved via the estimated band structures as well as density of states that the adsorption of Na causes dispersion within the conduction band of TiO_2 leading to band gap narrowing and promoting the photocatalytic activity.

In the second part of the thesis, the distinctive polymer sensitizer of PEDOT was adopted to couple with TiO_2 nanotubes scaffolding via a spin coating technique. The morphological analysis confirmed that PEDOT is embedded within the PEDOT-TiO_2 hybrids and the DRS measurements verified that it can be exploited as a visible light photosensitizer. The developed heterostructures exhibited a distinguishable photocurrent response and an inferior charge transfer resistance in comparison with the unsensitized TiO_2. Moreover, due to the relative band positions between the two phases, less chances for carriers' recombination are likely to happen and this in return advances the migration of the electron-hole pairs to the interface as precisely described in the mechanism of the photocatalytic process.

7.2 Future Recommendations

On the basis of the obtained results, we were able to provide accurate reasoning regarding the mechanism of the water splitting process that could be valuable for the advancement of efficient photoelectrochemical systems. Although, the adequacy of water splitting using TiO_2 is a long away from values that could contribute to the industrial scale, it is believed that the

development of new ideas and procedures will help solve the key limitations of the photoactive performance of TiO_2. Since the solar-to-chemical energy conversion efficiency is highly influenced by the efficiencies of several consecutive photocatalytic processes, such as: light absorption, carriers' separation, flow and utilization, it is of great necessity to work on enhancing the efficiency of all these stages within the photoelectrochemical system. Based on the above mentioned concerns, the subsequent future research perceptions could be realized.

➤ Study the effect of using different counter ions on the Na-modified TiO_2 performance and morphology.

➤ Investigate the possibility of performing annealing in different atmospheres on the Na-modified TiO_2 performance and morphology.

➤ Examine the consequences of using different polymerization techniques for PEDOT synthesis on the PEDOT-TiO_2 performance and morphology.

➤ Explore different types of polymers to sensitize TiO_2 surface along with PEDOT, thus developing multi-component photocatalytic system.

➤ Further, the kinetics of the water splitting process on the developed electrodes should be more adequately verified by properly describing the impact of incident photons on modifying of the material properties via space-resolved (interaction of photons with atoms, defect sites and grain-boundaries) and time-resolved (modelling of electron interactions, relaxation processes and chemical reactions) analyses. Additionally, simulation studies will help acquire extensive insights on the behavior of the TiO_2-based photocatalytic systems.

➤ Finally, a method of assimilating the fabricated photoanodes in the exceptional-performance Z-scheme water splitting systems is one of the novel avenues to effectively utilize TiO_2 as an oxygen evolution photocatalyst. In such configuration, the developed photoanodes will be concurrently used in the PEC cell along with a p-type photocathode to carry out overall water splitting. Adopting such system will reduce the energy needed to proceed the photocatalytic reaction. This is mainly due to the self-bias originating from the mismatch in the fermi-levels within the two phases which can also provide efficient carriers' separation and transportation in comparison with the ordinary one-step water splitting system. Moreover, this system will allow separate evolution of both hydrogen and oxygen which is vastly favorable for practical purposes to overcome the possibilities of an explosion which couldn't be accomplished by the regular one-step water splitting set-up.

On the basis of the above mentioned items, it is believed that the outcomes of this study may provide relevant understanding to the field of photoelectrochemical water splitting and can be further used to promote the development of this field. As we aim to see this research field progress in the near future.